DEPARTMENT OF MATERIAL SCIENCE AND ENGINEERING

NAGOYA INSTITUTE OF TECHNOLOGY

Ion Storage Properties of Single-walled Carbon Nanotubes used as Electrode Material for Electrochemical Capacitors

電気化学キャパシタ電極としての単層カーボンナノチューブのイオン吸蔵特性

JANUARY 2014

AYAR AYAD HUSSEIN AL-ZUBAIDI

アルーズバイディ　アヤル　アヤド　フッサイン

ABSTRACT

Electric Double Layer Capacitors (EDLCs), or electrochemical capacitors, store electric charge in the ionic layer that forms at the interface between an electrolyte and an immersed electrode. Charge storage in EDLC can be maximized by classical ways through increasing surface area of the porous electrode material, an approach of limited efficiency and eventually leads to electrode failure. An alternative modern approach involves using new material with defined and controllable pore structure for optimum electrolyte uptake. Among such materials, Single-walled Carbon Nanotubes (SWCNTs) stand as promising candidate material due to their superior electric conductivity and mechanical strength, defined and controllable morphology, and high theoretical surface area. But, the capacitance performance of SWCNTs realized in practice did not seem to reflect the theoretically anticipated performance. However, SWCNT samples investigated had low quality and purity, and wide diameter distribution, all leading to electrochemical performance that would significantly deviated from theory. This study investigated a new class of SWCNTs of high crystallinity and narrow diameter distribution as electrode material for EDLC. The study revealed unprecedented electrochemical features influenced by SWCNT fundamental characteristics in addition to their surface morphology.

In Chapter 2, the electrochemical behavior of SWCNTs as EDLC electrode was investigated by cyclic voltammetry (CV). It was revealed for the first time that the cyclic voltammogram of SWCNTs does not resemble the classical rectangular shape obtained with other carbon materials, nor does it resemble the often reported “butterfly” shape. Instead, the voltammogram had a “dumbbell-like” shape with large steps on both sides of a region of minimum capacitance in the middle, referred to as the “dumbbell grip”. By using SWCNT

samples separated into metallic and semiconducting tubes, and employing different aqueous and organic electrolyte solutions, It was confirmed that the width of the dumbbell grip is an intrinsic feature that reflects the electronic density of states (DOS) of SWCNTs, and correlates with the tube chirality and diameter irrespective of the electrolyte medium used.

In Chapter 3, ion adsorption on the outer and inner surfaces of SWCNTs was addressed. CV measurements were performed on closed-end and open-end SWCNTs at different scan rates, and in different aqueous and organic electrolytes. It was shown that, within the parameters tested, the outer surface of the tubes demonstrated the behavior of a flat electrode with little dependence on the potential scan rate, compared to the inner surface that acts as a porous electrode showing ohmic drop and distorted voltammogram at high scan rates. Mathematical analysis was used to quantify the increase in electrode resistance due to ion adsorption inside the tubes, the magnitude of which was dependent on the type of electrolyte medium.

Chapter 4 combined electrochemical measurements with in situ Raman spectroscopy to follow changes in charge carrier in the potential region of the dumbbell voltammogram. Sharp spectroscopic changes were observed on the spectra of metallic SWCNTs, and coincided with the two steps of dumbbell voltammogram, and correlate with the electronic band gap of semiconducting SWCNTs. Also the results of closed-end are compared with those of open-end SWCNTs, and show that spectroscopic changes with applied potential depend on the joined influence of electronic and surface structure of SWCNTs.

Finally, in Chapter 5, the electronic properties of SWCNTs were manipulated by doping with nitrogen. It was demonstrated the changes in electrochemical behavior of SWCNTs as EDLC electrode material, and reveal an enhancement in the ion adsorption kinetics and capacitance at high scan rate due to the improvement in electrode conductivity. In addition, an unusual increase in the capacitance of nitrogen-doped SWCNTs with charge-discharge cycling is revealed.

DEDICATION

To my dear brother, Salam.

Ayar

ACKNOWLEDGEMENT

I wish to convey my gratitude to all the people who kindly provided me with help and guidance throughout the course of conducting this study, and facilitated the accomplishment of this work.

I start by conveying my utmost respect to my teacher, **Professor Shinji Kawasaki**, for accepting me to join his research group and providing me with guidance moral support, which not only ensured successful completion of my research, but also made studying and living in Japan for me a positive and fruitful experience.

I would like to present my gratitude for the **Ministry of Education, Culture, Sports, Science and Technology (MEXT)**, for accepting me in the JAPANESE GOVERNMENT （MONBUKAGAKUSHO:MEXT） SCHOLARSHIP program, and offering me this life-changing opportunity to gain scientific knowledge, and also experience life and culture in Japan.

I wish to present my appreciation to my Senpai, **Dr. Yosuke Ishii**, for his continuing scientific guidance and advice. I am also grateful to him for introducing me to various aspects of Japanese culture, history, cuisine, and society, which enriched my knowledge and understanding of Japan, and deepened my appreciation of Japanese culture.

I wish to thank for the operators at the **Instrument and Research Technology Center** (大型設備基盤センター) for their valuable assistance in the characterization of the samples used this study.

I also wish to thank the working staff at the **beamline BL-18C at the Photon Factory (PF)**, at the High Energy Accelerator Research Organization (KEK) in Tsukuba, Japan, for providing the facility and equipment necessary for performing high –brightness synchrotron X-ray diffraction (XRD) measurements.

I also wish to acknowledge the kind advice and helpful discussions I received from **Dr. Khaled Parvez** from Max Planck Institute for Polymer Research, Germany, regarding the accomplishment

of the experimental part of chapter 5.

I greatly value the help and guidance I received as a foreign student from the **International Students Affair Office** at Nagoya Institute of technology, for the support they offered us and the cultural exchange events that helped us meet with other students from Japan and the rest of the world, and lead to the creation of friendly human relations that transcended the boundaries of nationality, culture, race, and ideology.

I take this chance to extend my deep gratitude to **Ms. Atsuko Arai** from the International Students Affair Office, and **Mr. Fumio Iwatsu** from the Education Center for International Students, for the great support they offered me during a period of injury that I suffered from on 2011.

With great regard, I wish to thank **Ms. Zinan Jiang**, foreign exchange student from Beijing University of Chemical Technology, China, thanks to whom I had a hard-working research partner to accomplish the work related to chapter 5, and gained a dear friend for life.

Finally, to the most important person in my life, my brother *Salam al-zubaidi*, I owe endless gratitude, for being the most generous, loving, and supporting brother a sister can hope to have, and for believing in me and being by my side at every step along the way.

TABLE OF CONTENTS

LIST OF FIGURES

of applied potential in (V) are indicated on the right.

Figure A3: Raman spectra for open-end SWCNTs in NaI using red laser (λ=632.8 nm). Values of applied potential in (V) are indicated on the right.

Figure A4: Raman spectra for open-end SWCNTs in KCl using red laser (λ=632.8 nm). Values of applied potential in (V) are indicated on the right.

Figure A5: Raman spectra for open-end SWCNTs in $TEMABF_4$ using green laser (λ=532 nm). Values of applied potential in (V) are indicated on the right.

Figure A6: Raman spectra for open-end SWCNTs in NaBr using green laser (λ=532 nm). Values of applied potential in (V) are indicated on the right.

Figure A7: Raman spectra for open-end SWCNTs in NaI using green laser (λ=532 nm). Values of applied potential in (V) are indicated on the right.

Figure A8: Raman spectra for open-end SWCNTs in KCl using green laser (λ=532 nm). Values of applied potential in (V) are indicated on the right.

Figure A9: Raman spectra for closed-end SWCNTs in NaCl using red laser (λ=632.8 nm). Values of applied potential in (V) are indicated on the right.

Figure A10: Raman spectra for closed-end SWCNTs in NaBr using red laser (λ=632.8 nm). Values of applied potential in (V) are indicated on the right.

Figure A11: Raman spectra for closed-end SWCNTs in NaI using red laser (λ=632.8 nm). Values of applied potential in (V) are indicated on the right.

Figure A12: Raman spectra for closed-end SWCNTs in KCl using red laser (λ=632.8 nm). Values of applied potential in (V) are indicated on the right.

Figure A13: Raman spectra for closed-end SWCNTs in NaCl using green laser (λ=532 nm).

Values of applied potential in (V) are indicated on the right.

Figure A14: Raman spectra for closed-end SWCNTs in NaBr using green laser (λ=532 nm). Values of applied potential in (V) are indicated on the right.

Figure A15: Raman spectra for closed-end SWCNTs in NaI using green laser (λ=532 nm). Values of applied potential in (V) are indicated on the right.

Figure A16: Raman spectra for closed-end SWCNTs in KCl using green laser (λ=532 nm). Values of applied potential in (V) are indicated on the right.

CHAPTER 1

CHAPTER 1

Introduction

1.1. Electric double layer capacitor: background

Electric double-layer capacitors (EDLCs) are electrochemical systems that are used as energy storage devices. Scientifically, the expression EDLC is used to describe the accumulation of charge on the interface of a charged electrode and a surrounding electrolyte. While a classical dielectric capacitor consists of two parallel surfaces where accumulation of two opposite charges occurs as the results of applied electric potential, an EDLC consists of one "real" surface of electronically conducting material (metal, semiconductor, carbon material) and a second "virtual" surface that is the inner interfacial limit of the conducting electrolyte solution phase. The double layer distribution of charges is established across this interfacial region.[1] Classically, this region was considered to be composed of a compact layer having the dimensions of about 0.5 to 0.6 nm, corresponding to the diameters of the solvent molecules and ions that occupy it, and a wider region of thermally distributed ions over 1 to 100 nm, depending on the ionic concentration. Recent observations of electrochemical behavior of nanoporous EDLC electrodes[2] lead to a modified perception of the composition of the double layer on the electrode surface, which incorporated the length scale of the space available for ion adsorption, as will be explained later in more detail.

EDLC in its simplest configuration consists of two electrodes immersed into electrolyte and separated by an ion-conducting but electron-insulating membrane. Upon the application of a potential to one of the electrodes the ions of the opposite sign travel from the bulk of the electrolyte and accumulate on its surface in a quantity proportional to the applied voltage, forming a so-called electrical double layer. This double layer consists of an electrical space charge from the electrode side and an ion space charge from the electrolyte side.[1]

The magnitude of electric potential applied to the EDLC electrode lies within a range called the stability window, inside which the applied potential causes the ionic species of the electrolytes to adsorb on the surface of the electrode, but not react with the electrode material.

Therefore, the charge storage mechanism in pure EDLC is physical and non- Faradaic, which means that during charging and discharging of this device no charge transfer takes place across the electrode/electrolyte interface and the energy storage is electrostatic in nature.

Apart from electrostatic ion adsorption, electrode materials with chemical groups on their surfaces may additionally exhibit chemical interactions with selected electrolytes, which involve fast and often reversible charge-transfer reactions between the carbon surface and the electrolyte ions, hence storing energy charge by the Faradaic charge transfer mechanism giving rise to the so called pseudo-capacitance. A capacitor combining both the double layer and pseudo-capacitance is given the general term "supercapacitor".

Since physical charge storage remains the dominant mechanism in EDLCs, they are capable of fast delivery of stored charge without any limitation caused by the electrochemical kinetics found in batteries. They are therefore characterized by very high power density and long cycle life, which makes them particularly useful for high power applications. In applications that require high energy and high power delivery, EDLCs can be used to complement the lithium ion rechargeable batteries, which provide high energy density but low power density. On the other hand, the major drawback of EDLCs is their lower energy density, which is bound by the available surface area for ion adsorption, resulting in less energy stored per unit mass compared to that of rechargeable batteries.

The energy density of an EDLC is determined by the capacitance of positive and negative electrodes and the maximum voltage, at which the device can be operated:

$$E^{EDLC} = \left(\frac{C_- C_+}{C_- + C_+}\right)(V_{max}^{EDLC}) \tag{1.1}$$

To maximize the energy of an EDLC the capacitance of both electrodes should be the same. In this case:

$$E^{\mathrm{EDLC}} = \frac{1}{2} C \left(V_{max}^{\mathrm{EDLC}}\right)^2 \tag{1.2}$$

The maximum voltage is generally determined by the stability window (from the lowest stable potential V_{low} to the highest stable potential V_{high}) of the selected electrolyte. Impurities and functional groups on the electrode may catalyze electrolyte decomposition and increase stable V_{low} or decrease V_{high}, thus lowering EDLC maximum voltage and energy density.

Increasing the low energy density of EDLC has been the focus of many research efforts over the past few decades, because higher energy density is a crucial requirement for expanding the application possibilities of EDLC to a wider range, and employing them in more advanced applications like electrical vehicles as high power, next generation replacements for rechargeable batteries. Achieving high energy storage in EDLCs necessitates the development of an electrode material that exhibits high electrochemical and temperature stability, as well as high accessibility for the electrolyte ions. Porous carbon materials are the most common EDLC electrode materials, with high conductivity, and a porous structure that offers the surface required for the formation of the double layer of adsorbed ions. The highest possible ion accessibility into the porous structure of the electrode can be realized in two different ways. The first is to maximize ion accessibility by increasing the specific surface area of electrode materials in EDLCs. However, the effectiveness of this approach is limited. A typical example of such limitation is seen with activated carbon that has a high surface area compared to other materials, and is being the most commonly used electrode material in commercial EDLCs. With the increase in its surface area, activated carbon was shown to exhibit a reduction in both stability and conductivity, which in turn resulted in deterioration in the electrode capacitance.[3]

The second approach is to design the pore structure of the electrode material for optimum electrolyte uptake, which requires precise knowledge of the specific ion–pore size relationship. For this purpose, materials with well-defined and controllable pore structure have proved to be promising for energy storage purposes, and also in terms of utilizing their predefined structure to identify the precise ion adsorption behavior in relation to the pore structure.[2, 4-11]

Below a summary is given about the models proposed in literature to describe the structure of the double layer on the electrode surface, and the evolution of those models with new insight on EDLC behavior in constraint porous space.

1.2. Formation of the double layer: electrolyte–electrode interactions

1.2.1. Helmholtz model

The Helmholtz model was the first type of model proposed used to understand the energy-storage mechanism in terms of the structure of the double layer at an

electrode/electrolyte interface. The model is analogous to that in a solid-state capacitor—i.e., two layers of charge of opposite sign are separated by a fixed distance. In this case, one may assume electrons in the electrode and positive ions in solution. Such structure is equivalent to a parallel-plate capacitor (Figure 1.1a), and has the following relation between the stored charge density (Q) and the voltage drop (V) between the plates:

$$Q = \frac{\varepsilon\varepsilon_o}{d}V \tag{1.3}$$

where ε is the dielectric constant of the medium, ε_o is the permittivity of free space, and d is the interplate spacing. The differential capacitance is therefore:

$$\frac{\partial Q}{\partial V} = C = \frac{\varepsilon\varepsilon_o}{d} \tag{1.4}$$

leading to

$$C/A = \frac{\varepsilon\varepsilon_o}{d} \tag{1.5}$$

The model assumes constant differential capacitance, hence does not account for the dependence of the measured capacity on potential or electrolyte concentration. Variations in C with potential and concentration suggest that either ε or d depends on these variables necessitating more sophisticated treatment in describing the adsorption of ions on charged surfaces. Such variation of differential capacitance with applied potential and ionic concentration was later observed and accounted for by the Gouy-Chapman model.

1.2.2. The Gouy-Chapman theory

In this model Gouy and Chapman considered observations that capacitance was not a constant and depended on the applied potential and the ionic concentration. To account for that observation Gouy, and independently, Chapman pictured a diffuse double layer composed of ions of opposite charge (counterions) attracted to the surface, and ions of the same charge (coions) repelled from it. Ions are embedded in a dielectric continuum while the electric potential is subject to the Poisson-Boltzmann (PB) differential equation. The greatest concentration of excess charge would be adjacent to the electrode, while progressively lesser

concentrations would be found at greater distances as those forces become weaker. Thus, an average distance of charge separation replaces *d* in the capacitance expression.[12] Also; we can expect that average distance to show dependences on potential and electrolyte concentration. As the electrode becomes more highly charged, the diffuse layer should become more compact and Q should rise. As the electrolyte concentration rises, there should be a similar compression of the diffuse layer and a consequent rise in capacitance.

To formulate this model the Poisson equation was used to relate potential to charge density:

$$Q(x) = -\varepsilon\varepsilon_o \frac{d^2V}{dx^2} \tag{1.6}$$

The Boltzmann equation was used to determine the distribution of ions:

$$n_i = n_i^o exp\left(\frac{-z_i eV}{\acute{k}T}\right) \tag{1.7}$$

Here n_i^o is the concentration of ion *i* in the bulk, *e* is the unit charge, z_i charge on the ion i, ќ Boltzmann constant, and *T* absolute temperature. The total charge density per unit volume for all ionic species is the sum over all ions:

$$Q(x) = \sum n_i\, z_i e = \sum n_i^o z_i\, e\, exp\left(\frac{-z_i eV}{\acute{k}T}\right)$$

The combination of the two equations above would eventually lead to the differential capacitance expressed in terms of the electric potential *V* and temperature *T* as follows:

$$C = \frac{dQ}{dV}$$

Or

$$C = \left(\frac{2z_i^2 e^2 n_i^o \varepsilon\varepsilon_o}{\acute{k}T}\right)^{1/2} \cosh\left(\frac{z_i eV}{2\acute{k}T}\right) \tag{1.8}$$

The adsorption process described by the Gouy-Chapman model is called non-specific adsorption, as it arises due to electrostatic interaction between point charge ions and the charge on the electrode. The size of the ions is introduced only as a distance of closest approach to the electrode (x_2) that is similar for each ion. An ionic atmosphere or diffuse layer extends from x_2

and decays out into the bulk of the solution, the net charge on this diffuse layer being equal and opposite to that on the metal surface. In practice, different types of electrical interactions such as electric field forces, image forces, dispersion forces, and electronic or repulsive forces, can occur between the electrodes and ions, causing ions to approach the electrode closer than x_2, giving rise to what is called "specific adsorption" between ions and the electrode. Specific adsorption can occur when bond could be formed by partial electron transfer between the ion and the electrode (chemisorption). Other effects, like the 'squeezing out' of a structure- breaking ion from the bulk of the solution may also contribute to the specific interaction. Because such specific forces are short-range, specifically adsorbed ions are usually located in a monolayer with their centers in a plane at x_1, from the electrode ($x_1 < x_2$), which cannot be accounted for by the Gouy-Chapman model. Therefore, while for or low concentration electrolytes, the Gouy-Chapman theory has been successful in predicting ionic profiles close to planar and weakly curved surfaces, it is known to overestimate strongly ionic concentrations close to charged surfaces.[13]

1.2.3. The Stern model

This model is a hybrid of the two models above. First, ions are considered to have a finite size and are located at a finite distance from the electrode. Second, the charge distribution in the electrolyte is divided into two parts: (i) an immobilized, Helmholtz-like part close to the electrode, and (ii) a Gouy-Chapman part, diffusely spread out in solution. There is a linear variation of potential with distance across the Helmholtz component and a semi-exponential variation in the Gouy-Chapman component of the double layer (Figure 1.1c). [13]

In concentrated electrolytes the structure of the double layer resembles that described by Helmholtz model (i.e., most of the charge is concentrated in the Helmholtz layer). On other hand, in extremely dilute solution the double-layer structure approaches that of the Gouy-Chapman model. However, this model does not take into account the role of the solvent as related to the hydration of the ions and its influence on the structure of the double layer.

1.2.4. Triple-layer model: Esin and Markov, Grahame, and Devanathan model.

The subtle feature of this model proposed by the three groups was to take into consideration that ions could be dehydrated in the direction of the electrode and specifically adsorbed on its

surface (Figure 1.1d). Thus, an inner layer between the electrode surface and the Helmholtz layer further modifies the structure of the double layer.[13] This inner layer is the locus of centers of unhydrated ions strongly attached to the electrode.

For this case, Devanathan proposed that the capacitance is obtained by as the outcome of the capacitance contributions of several individual components as seen in the equation below:

$$\frac{1}{C} = \frac{1}{C_{\mathrm{M-1}}} + \left(\frac{1}{C_{\mathrm{M-2}}} + \frac{1}{C_{\mathrm{2-b}}}\right)\left(1 - \frac{dq_l}{dq}\right) \tag{1.9}$$

where $C_{\mathrm{M\text{-}1}}$, $C_{\mathrm{M\text{-}2}}$, $C_{\mathrm{2\text{-}b}}$, are the capacitance components from the space between the electrode and the inner Helmholtz plane (IHP), the space between the inner and outer Helmholtz planes (OHP), and the diffuse double layer, respectively, while dq_l/dq is the rate of change of the specifically adsorbed charge with charge on the electrode. Hence, this model is referred to as the triple-layer model, and suggests the following characteristics:

- If (dq_l/dq) is zero, the expression for the capacity C is equivalent to that for 3 capacitors in series, that is, inner Helmholtz, outer Helmholtz, and Gouy. Hence, this model is referred to as the triple-layer model.
- The capacity is a minimum when (dq_l/dq) is zero, because the latter can have only positive values.
- If (dq_l/dq) exceeds unity, the differential capacity attains large values. When C tends to infinity, the electrode becomes non-polarizable.
- The minimum in the capacity is in the vicinity of the potential of zero charge.

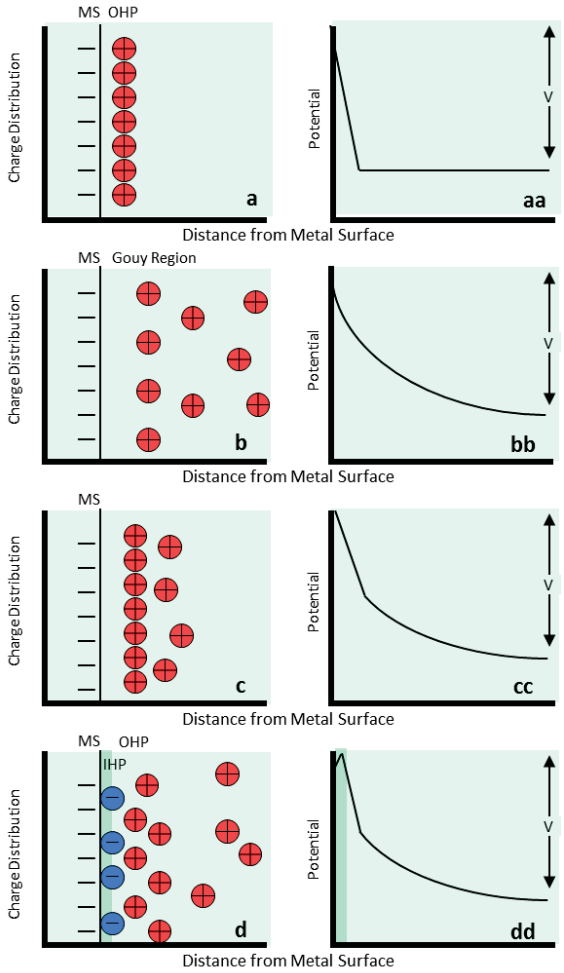

Figure 1.1: Charge distribution vs. distance and potential variation vs. distance: (a) and (aa) Helmholtz model; (b) and (bb) Gouy-Chapman model; (c) and (cc) Stern model, and (d) and (dd) Esin and Markov, Grahame, and Devanathan model.

1.2.5. Beyond the parallel-plates model: pore curvature and ion desolvation effects.

In all the previous models the capacitance of EDLCs was depicted in a parallel-plate capacitor configuration (Figure 1.2a), mathematically described by equation 1.5.

For cylindrical mesopores, it was hypothesized that solvated counterions would enter pores and approach the pore walls to form what was called an electric double-cylinder capacitor (EDCC; Figure 1.2b). The double-cylinder capacitance was given as: [14]

$$C = \frac{2\pi\varepsilon_r\varepsilon_0 L_p}{ln(b_c/a_c)}$$

Or

$$C/A = \frac{2\pi\varepsilon_r\varepsilon_0 Lp}{b_c\, ln(b_c/(b_c - a_c))} \tag{1.10}$$

where L_p is the pore length and b_c and a_c are the radii of the outer and inner cylinder, respectively. The EDCC model can be reduced naturally to the EDLC model when the pores are large enough so that the pore curvature is no longer significant and can be approximated by a planar surface.[15]

All the previous models were based on the concept of an ionic layer that consists of ions surrounded by a shell of the solvent molecules, known as the solvation shell. According to this perception, the definition of the optimum pore size required to achieve maximum capacitance was that large enough to accommodate the ion plus the surrounding solvation shell. These assumptions were consistent with previous work showing that ions carry a dynamic sheath of solvent molecules, the solvation shell, and that some hundreds of kilojoules per mole are required to remove it in the case of water molecules.

As a result, a pore size distribution in the range 2–5 nm, which is larger than the size of two solvated ions, was then identified as a way to improve the energy density and the power capability. The double layer charging was deemed unfavorable in the confined space of micropores, where there is no enough space for the formation of the Helmholtz layer and diffuse layer at a solid–electrolyte interface. Accordingly, it was assumed that pores smaller than 0.5 nm were not accessible to hydrated ions, [16, 17] and even pores under 1 nm were considered too small, especially in the case of organic electrolytes, where the size of solvated ions is larger than 1 nm.[18]

However, several experiments using different carbon materials with significant contribution of micropores, [19-25] reported unexpectedly high capacitance, contradicting the solvated ion adsorption theory, particularly when organic electrolytes were employed where the large size of the solvated ion prevents adsorption in micropores. These findings suggested that a partial desolvation of ions could occur, allowing access to small pores, leading to improved capacitance. The most convincing evidence of capacitance increase in pores smaller than the solvated ion

size was provided by experiments using carbide derived carbons (CDCs) [26-28] as active material. The change of capacitance with pore size was reported by Chmiola *et al.*,[2] and later confirmed by other studies,[29, 30] to be a linear function of $1/b_c$ (where b_c is the pore radius), confirming that the distance between the ion and the carbon surface, d, was shorter for the smaller pores.

These results challenged the long-held assumption that pores smaller than the size of solvated electrolyte ions do not contribute to energy storage, and the anomalous increase in capacitance in subnanometer pores was ascribed to the desolvation of the electrolyte ions entering subnanometer pores, [2, 9] which was verified by experiments utilizing an ionic liquid electrolyte with no solvation shell around the electrolyte ions.[31]

In lights of these findings, it was assumed that for micropores where the small-size pores do not allow the formation of a double cylinder, counter-ions (solvated or desolvated) would enter the pores and line up to form electric wire-in-cylinder capacitor (EWCC; Figure 1.2c). [29, 30] In a way, EWCCs can be also viewed as EDCCs, but the key quantity for EWCCs is the radius of the inner cylinder a_0, which is the effective size of the counterions (that is, the extent of electron density around the ions). By using a_0, equation 1.10 (EDCC) becomes:

$$C/A = \frac{\varepsilon_r \varepsilon_0}{b_c \, ln(b_c/a_0)} \tag{1.11}$$

From detailed analysis of experimental data previously obtained data by many researchers, Huang *et al.* [30] concluded that the EDLC/EDCC/EWCC model was valid regardless of the type of carbon materials used for electrode-active materials, and was universal to carbon electrochemical capacitors with diverse electrolytes of various concentrations.

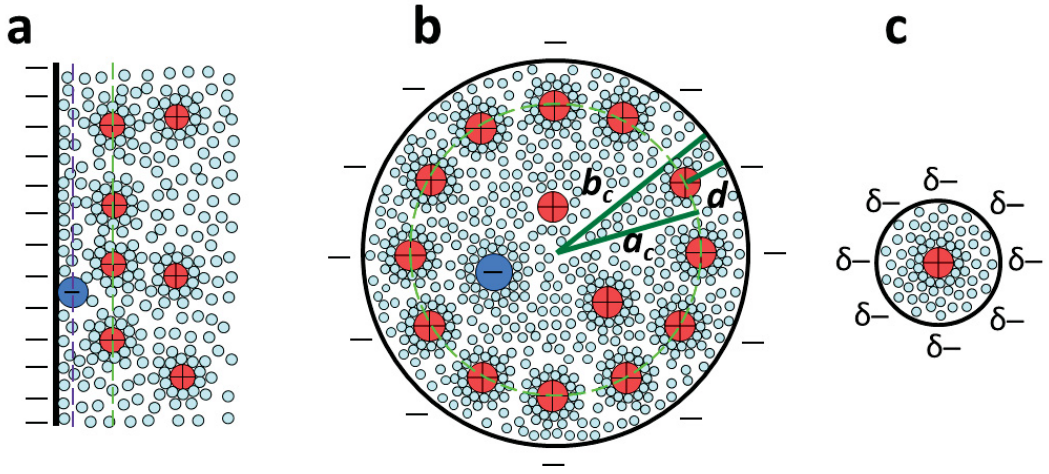

Figure 1.2: (a) An electric double-layer capacitor (EDLC) formed with solvated cations at the carbon/electrolyte interface in which the inner and outer Helmholtz planes (IHP, OHP) are marked by purple and green dashed lines, respectively. (b) top views of a negatively charged mesopore with solvated cations approaching the pore wall to form an electric double-cylinder capacitor (EDCC) with radii b_c and a_c for outer and inner cylinders, respectively, separated by distance d, and (c) a negatively charged micropore of radius b_c with solvated/ desolvated cations of radius a_0 lining up to form an electric wire-in-cylinder capacitor (EWCC).

1.3. Electrode materials for EDLC

The basic definition of electrode capacitance, based on the concept of formation of ionic layer on the electrolyte/electrode interface, implies that the key to reaching high capacitance by charging the double layer lies in using high specific surface area (SSA) blocking and electronically conducting electrodes.

One of the most commonly used EDLC electrode materials is activated carbon, due to its high SSA and moderate cost. Activated carbon contains a porous network of broad distribution of pore size in the bulk of the carbon particles, and consists of micropores (<2 nm in size), mesopores (2–50 nm) and macropores (>50 nm). A typical cyclic voltammogram of a two-electrode EDLC laboratory cell is presented in Figure 1.3 below. Its rectangular shape is characteristic of a pure double layer capacitance mechanism for charge storage according to:

$$I = C \times \frac{dV}{dt}$$

where I is the current, (dV/dt) is the potential scan rate, and C is the double layer capacitance. Assuming a constant value for C, and for a given scan rate the current I is constant, and a rectangular cyclic voltammogram is obtained.

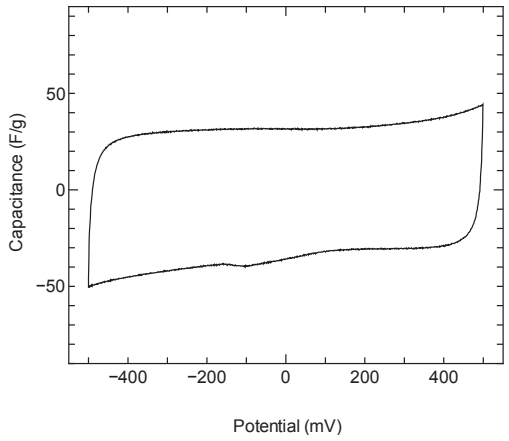

Figure 1.3: Cyclic voltammetry of activated carbon powder in 1.0 M NaCl.

The promising power performance and reliability of EDLCs compared to other energy storage devices caused progressive expansion in their use from small-scale application like consumer and microelectronics, to wider and heavier duty applications such as electric or hybrid vehicles, and grid-scale energy storage, which inevitably led to an increase in their energy density requirements, and activated carbon could no longer fulfill the new power and energy requirements. Initial research on activated carbon was directed towards increasing the pore volume by developing high SSA and refining the activation process. However, the SSA of a porous material cannot be increased indefinitely, because the electrical conductivity, which is an essential requirement to minimize the equivalent series resistance (ESR), generally decreases as the surface area increases, due to a disruption of the electronic conduction bands and physically less carbon in the pore walls. More importantly, and as explained above, the advances made in the basic understanding of the nature of the double layer led to recasting the theory of double layer in electrochemistry to take into account pore size and shape, and ion solvation and desolvation effects, which in turn revolutionized both the process of material selection as well

as the fundamental understanding of the behavior of ions confined in nanopores, and necessitated the reinvestigation of EDLC electrode material selection, with special attention to the aforementioned considerations. To this end, later studies focused on controlling the effectiveness of ion storage by elimination of the macro- and mesopores of existing materials, and matching the pore size with the ion size, while others aimed at developing and testing new carbons that can accommodate energy requirement and still maintain the necessary low resistivity for high power performance. Graphitic carbon seemed to satisfy the requirements for this purpose, with high conductivity, electrochemical stability and open porosity.[32] Several carbon materials were investigated as EDLC electrodes, including templated and carbide-derived carbons (CDC),[33] carbon fabrics, fibers,[34] onions[35] and nanohorns.[36] Several reviews concerning the choice and investigation of EDLC electrode materials can be found in literature for further reference.[7, 37, 38] The next section will focus on single-walled carbon nanotubes (SWCNTs) as the main topic of the current study.

1.4. Single-walled Carbon Nanotubes: One-dimensional macro molecule.

Since their discovery, single-walled carbon nanotubes (SWCNTs) were considered promising candidate materials for high energy density EDLC electrodes, because they exhibit exceptional properties such as high electrical conductivity, high specific surface area, high charge transport capability, and also tunable porosity. In order to achieve high performance from such potentially promising material, it becomes essential to accurately understand the charge storage performance of SWCNTs, which in turn necessitates understanding the fundamental properties of SWCNTs in order to have insight into the elements of significant relevance to their electrochemical behavior, which are their surface structure, and also electronic structure.

1.4.1. Surface structure of SWCNTs

A single-walled carbon nanotube (Figure 1.4) can be described as a graphene sheet (a single layer from the graphite crystal) that is rolled up into a continuous cylinder whose tip ideally terminates with a fullerene-like cap or hemisphere. Being one atom in thickness and about few microns in length,[39] a SWCNT has a high aspect ratio (10^4 – 10^5) due to which it can be classified as a one-dimensional nanostructured material. Carbon atoms in SWCNTs are bonded

by sp^2 hybrid orbitals that allow them to form hexagons and occasionally pentagons and heptagon units by in-plane σ bonding and out-of-plane π bonding. Tube curvature results in σ-π rehybridization or mixing, in which three σ bonds are slightly out of plane; for compensation, the π orbital is more delocalized outside the tube. This makes nanotubes mechanically stronger, and electrically and thermally more conductive than graphite.[40]

Depending on the conditions of the growth process, SWCNTs can be open-ended or closed ended with caps of fullerene hemispheres.[41] Each cap contains six pentagons and an appropriate number and placement of hexagons that are selected to fit perfectly to the long cylindrical section.[39] SWCNTs do not exist individually; rather, they tend to group into bundle-like structures because they are held together by the non-covalent van der Waals bonds to form a two-dimensional triangular lattice with a lattice constant of 1.7 nm, and an inter-tube separation of 0.315 nm at closest approach within a rope.

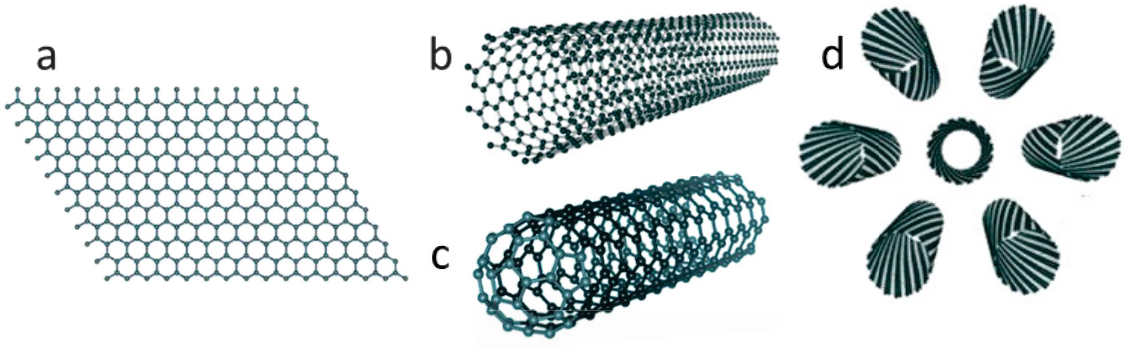

Figure 1.4: (a) Graphene sheet, (b) Open-end and (c) closed-end Single-walled carbon nanotube (d) Bundle of aggregated tubes.

The process of rolling a graphene to form a single-wall carbon nanotube results into a cylinder with axial symmetry and a spiral conformation, called *chirality*. The tube chirality is the outcome of the different possible orientations of the six-membered carbon ring (hexagon) in the honeycomb lattice relative to the axis of the nanotube. It is the most important characteristic feature that defines SWCNTs, and separates them from other graphitic allotropes, because it reflects directly on their electronic structure and – as will be revealed for the first time in the next chapter – their electrochemical behavior as well. The manner of rolling the graphene sheet determines its chirality as will be explained in more detail below.

The unit cell of the carbon nanotube is shown in Figure 1.5 as the rectangle bounded by two

vectors, the *chiral vector* C_h and the *translation vector T*.[42]

The chiral vector C_h is described as the vector that joins two equivalent points on the original graphene lattice. This means that the SWCNT cylinder is produced by rolling up the sheet such that the two end-points of this vector are superimposed. The chiral vector is defined on the honeycomb lattice as follows:

$$C_h = n\mathrm{a}_1 + m\mathrm{a}_2 \tag{1.12}$$

where (n, m) are two integer indices ($n \geq m$) that denote the number of unit vectors $n\mathrm{a}_1$ and $m\mathrm{a}_2$ in the hexagonal honeycomb lattice contained in the vector, and taken respectively in the direction of a_1 and a_2, which are the unit cell base vectors of the graphene sheet. The vector a_1 lies along the "zigzag" line, while vector a_2 direction is a reflection of a_1 over the "armchair" line in Figure 1.5. The two vectors can be mathematically determined as follows:

$$\mathrm{a}_1 = \left(\frac{\sqrt{3}}{2}a, \frac{a}{2}\right), \mathrm{a}_2 = \left(\frac{\sqrt{3}}{2}a, -\frac{a}{2}\right)$$

where a is the here $a = a_{\mathrm{C-C}} \times\sqrt{3}$ = 2.49 Å is the lattice constant of the honeycomb lattice in the rolled graphene layer, where $a_{\mathrm{C-C}}$ is the nearest-neighbor C–C distance (1.44 Å in SWCNT).

The length L of the chiral vector C_h becomes the circumference of the tube, and is directly related to the tube diameter, which is also expressed in terms of chiral indices as seen below:

$$L = \pi d_t$$

$$d_t = \frac{\sqrt{n^2 + m^2 + nm}}{\pi}a \tag{1.13}$$

$$L = |C_h| = a\sqrt{n^2 + m^2 + nm} \tag{1.14}$$

The chiral angle θ between the C_h direction and the zigzag direction of the honeycomb lattice of the tube can also be determined from chiral indices as follows:

$$tan\,\theta = \frac{\sqrt{3}m}{2n + m} \tag{1.15}$$

The second vector is *T*, the 1D translation vector of the nanotube. The vector T is normal to

C_h and extends from the origin to the first lattice point B in the honeycomb lattice. T is expressed in terms of the integers (t_1, t_2) that can also be given in terms of the chiral indices n and m as follows:

$$T = t_1 \mathrm{a}_1 + t_2 \mathrm{a}_2 \tag{1.16}$$

$$t_1 = \frac{2m + n}{d_R}, t_2 = -\frac{2n + m}{d_R}$$

The length T of (T) is given as:

$$\mathrm{T} = \frac{\sqrt{3}L}{d_R} \tag{1.17}$$

In which d_R is either equal to d (the highest common divisor of (n, m)), or to 3d, which depends on whether n - m = 3dr, r being an integer, or not. Finally, the number of carbon atoms per unit cell, of the 1D tube is 2N, given as:

$$N = \frac{2(n^2 + m^2 + nm)}{d_R} \tag{1.18}$$

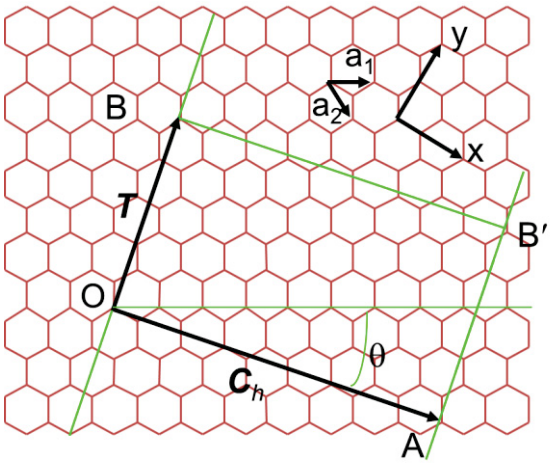

Figure 1.5: 2D graphene sheet shown along with the chiral vector that specifies the chiral nanotube and translation vector.

From the explanations above, it becomes clear that the chirality of SWCNT can be

conveniently expressed it terms of solely the chiral indices (n, m) that provide information about the tubes geometry and, as will be shown later, the electronic structure of SWCNT as well.

By rolling a graphite sheet in different directions, three typical nanotubes can be obtained: zigzag tube $(n, 0)$ obtained graphene sheet is rolled along the zigzag direction, armchair tube (n,n) rolled along the armchair direction, and chiral tube (n, m) with chiral vector along neither directions. The tube chiral indices are defined in within the relation $n > m > 0$. Figure 1.6 shows the three rolling patterns, and Figure 1.7 shows the appearance of the three types of SWCNTs chiralities.

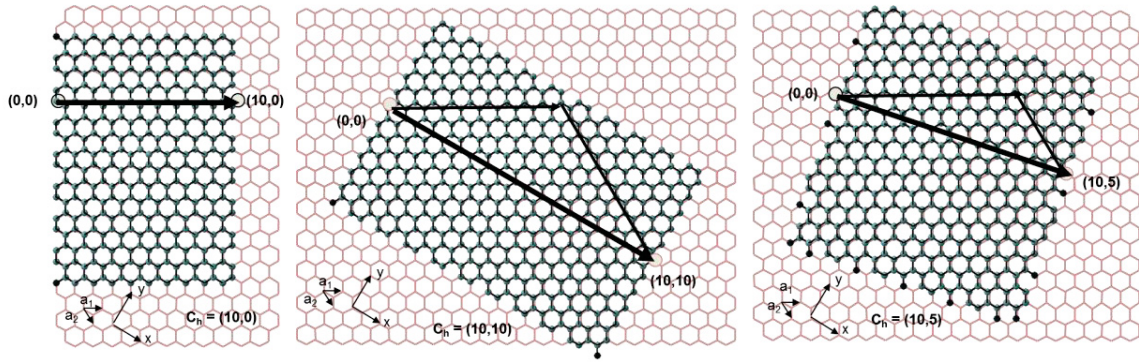

Figure 1.6: Examples of the three rolling patterns of SWCNTs with (a) $m = 0$ (b) $n = m$ and (c) $n \neq m$.

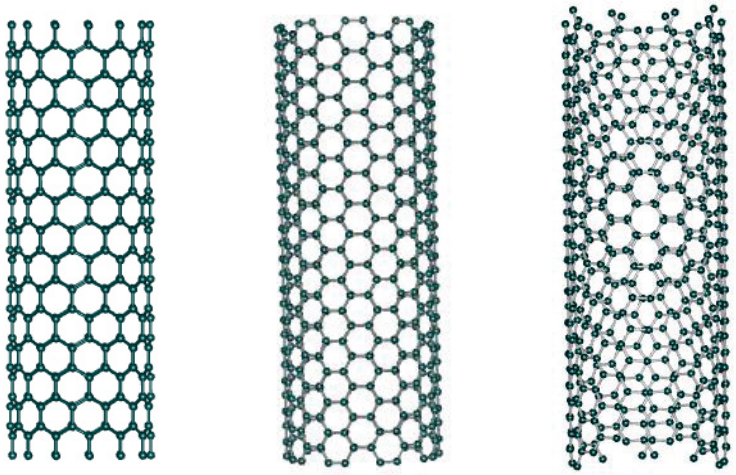

Figure 1.7: The three chiralities of SWCNTs (a) Zigzag ($m = 0$) (b) Armchair ($n = m$) and (c) Chiral ($n \neq m$).

1.4.2. Electronic structure of SWCNTs

Since a nanotube is a one-dimensional crystal obtained from a graphene sheet rolled into a tube, the electronic structure of graphene becomes the starting point for understating that of nanotubes.

Graphene has a hexagonal lattice with two atoms per unit cell, termed A and B atoms (Figure 1.8). Each atom has one s and three p orbitals. The s orbital and the two in-plane p orbitals (2s, 2px and 2py) are tied up in graphene's strong covalent bonding and do not contribute to its conductivity, while the remaining 2pz orbital, oriented perpendicular to the molecular plane, and through interaction with neighboring 2pz orbitals forms non-localized bonding π and anti-bonding $\pi*$ orbitals. The π bonds pointing out of the plane are responsible for the weak interactions between different graphene layers in graphite—or between bundled SWNTs—and play the key role in the determination of the electronic properties.

The graphene primitive cell in the reciprocal space, known as the Brillouin zone, is also a honeycomb lattice, with six corner points located at its boundary, called the K –points. The energy structure (ranges of energy that an electron may have, and gaps or forbidden ranges of energy that it may not have) in the valence and conducting bands of graphene is linear, and the two bands join like *cones* at these K –points through which Fermi energy passes (Figure 2.4 in Ref 39). As a result, graphene has a zero-band gap at the K –points.[39]

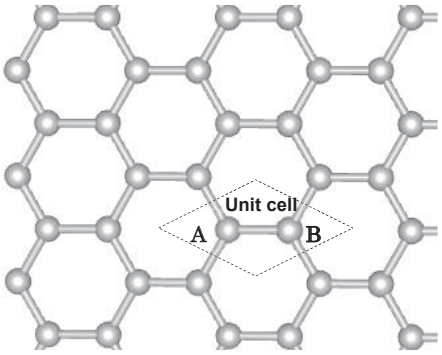

Figure 1.8: The lattice structure of graphene. The two atoms per unit cell are labeled A, and B.

As the 2D graphene plane is rolled into 1D nanotube, the electronic structure of graphene is modified to that of a tube by using periodic boundary conditions in the circumferential direction. As a result, the wave vector associated with the *Ch* direction becomes quantized, while the wave

vector associated with the direction of the translational vector T (or along the nanotube axis) remains continuous for a nanotube of infinite length. By this quantization Ch and T is transformed into K_1 (discrete unit vector along the circumferential direction) and K_2 (reciprocal lattice vector along the nanotube axis), given by the following equations:

$$K_1 = [(2m + n)b_1 + (2n + m)b_2]/Nd_R \tag{1.19}$$

$$K_2 = (mb_1 - nb_2)/N \tag{1.20}$$

where b_1 and b_2 are the reciprocal lattice vectors of two-dimensional graphite in the x, y coordinate, given by:

$$b_1 = \left(\frac{1}{\sqrt{3}}, 1\right)\frac{2\pi}{a}, b_2 = \left(\frac{1}{\sqrt{3}}, -1\right)\frac{2\pi}{a}$$

The periodic boundary condition for a carbon nanotube (n, m) gives N discrete k values in the circumferential direction. The direction of the discrete k vectors and the separation between two adjacent k vectors are both given by the K_1 vector shown in Figure 1.9.[43]

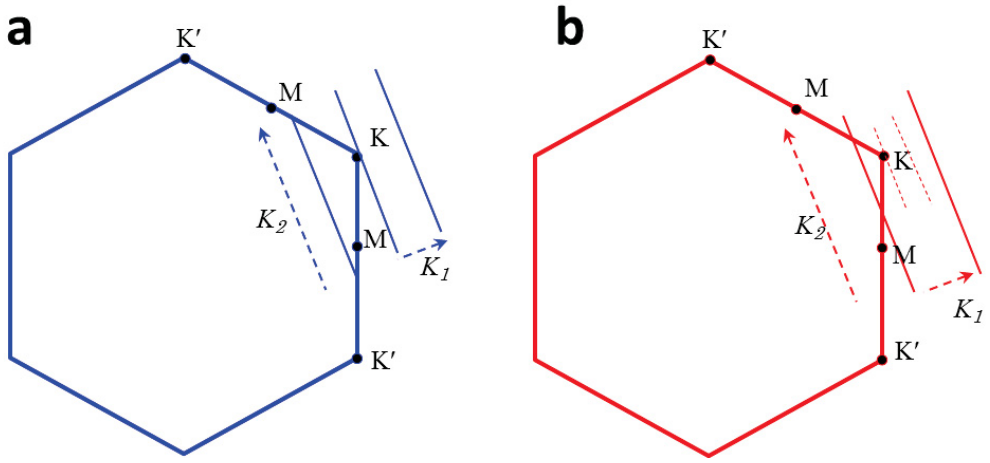

Figure 1.9: The wave vector k for one-dimensional carbon nanotubes is shown in the two-dimensional Brillouin zone of graphite (hexagon) as bold lines for (a) metallic and (b) semiconducting carbon nanotubes.

If for a particular (n, m) nanotube, the cutting line passes through a K – point of the 2D Brillouin zone (Figure 1.9), where the π and π* energy bands of graphene are degenerate by symmetry, the resulting one-dimensional energy bands will have a zero energy gap. Further, the

density of states (DOS) at the Fermi level has a finite value for these carbon nanotubes, and they therefore are metallic. If the cutting line does not pass through a K –point, then the carbon nanotube is expected to show semiconducting behavior, with a finite energy gap between the valence and conduction bands.[39] The geometrical condition for the cutting lines to pass through the K –points requires that ($n - m$) is a multiple of 3. In particular, the armchair nanotubes denoted by (n, n) are always metallic, and the zigzag nanotubes (n, 0) are only metallic when n is a multiple of 3. It follows that approximately one third of the carbon nanotubes are metallic and the other two thirds are semiconducting.[39]

Therefore, the chirality-related electronic density of states (DOS) of SWCNTs is unique for each tube, and of significant relevance to the optical and charge storage properties of that tube. The discontinuity known as a van Hove singularity (VHS) on the DOS of SWCNTs is the result of the one-dimensional confinement of electrons due to the quantization discussed above. This means that energy required to excite an electron from one VHS in the valence band to a symmetrical one in the conduction band becomes a signature that correlates to the tube chirality and provides identification information about the tube. As a result, van Hove singularities are important for determining many solid state properties of carbon nanotubes, such as optical absorption and resonant Raman spectroscopy,[43] as well as charge transfer properties as will be shown in detail in the following chapters.

1.4.3. Calculation of SWCNT density of states

Two main methods are used to calculate the density of states of SWCNTs: density functional theory (DFT), and tight binding model. The employment of the two methods is reported frequently in literature, where methodology of each approach is discussed in detail. Here a brief discussion of each method presented to provide some insight on the merits and demerits of each.

Density functional theory is a first principle calculation method based on fundamental concepts, and incorporates two core elements, the Hohenberg-Kohn theorem and Kohn-Sham equations. The method obtains all information about a given system from the system electron density instead of the wave function. The nuclear degrees of freedom (e.g. the crystal lattice in a solid) appear only in the form of potential acting on the electrons, so that the wave function depends only on the electronic coordinates. A term called “electron-electron interaction” is incorporated to differentiate the quantum mechanics of single-body from those with many-body

problem. These properties are built into DFT in a very fundamental way. DFT is a general, parameter-free flexible theory with a proven record of calculating the electronic states of both semiconductors and molecules. The well-known weakness of DFT is its underestimation of the band gap of semiconductors, which is not a trivial issue for electronic device modeling. Also, while the use of hybrid density functionals was shown to improve the accuracy in describing the electronic structure of semiconducting bulk materials and also SWCNTs, the biggest weakness of this approach is the limited size of the systems that can be treated, which makes it time demanding and impractical for SWCNTs, where the number of carbon atoms in the unit may contain from hundreds to thousands of carbon atoms.[44, 45]

This latter problem is absent in the tight binding method, which uses the concept known as zone folding, whereby cutting lines are defined as zone-folded one-dimensional (1D) Brillouin zone (BZ) line segments, expressed in relation to their two-dimensional (2D) BZ counterparts.[39]

This approach in general, and gives reliable electronic energies for states no too far away from the Fermi level and for large enough nanotubes (d_t~1.5 nm). However, since it is based solely on the confinement of the electronic states along the circumferential direction, it completely neglects the curvature of the nanotube wall that becomes important for smaller-diameter. As a result, while zone folding correctly predicts the metallic and semiconducting character of tubes with diameter between 0.5 and 1 nm, it overestimates the energies of the conduction bands, and completely fails for very small nanotubes (d_t < 0.5nm).

Nevertheless, should the effect of tube curvature be correctly addressed, the zone folding approximation becomes a feasible technique that not only predicts correct energies, but also offers an important advantages over most other methods in the sense that it is extremely fast and can calculate the properties of any desired nanotubes within seconds, which makes it more useful for calculation of electronic structure of tubes that have so many carbon atoms in their unit cell that they are far beyond first-principle calculations.

Upon the application of tight binding method, three possible effects are considered in connection with first principles calculations of the electronic structure of carbon nanotubes:(1) the effect of curvature on carbon-carbon interaction energy γ_0, (2) the inclusion of the so-called tight binding overlap integral s, associated with the asymmetry between the valence and conduction bands in 2D graphite,[39] and (3) the trigonal warping effect in which the equi-energy contours change from a circle to a triangular shape with increasing energy as shown in FIG.1

from Ref. 43.

To tackle the influence of surface curvature, one must consider the fact that the carbon-carbon distance for atoms in SWCNTs is different from that in graphene. Also, rolling up of the graphene sheets the angle of the hexagon is also changed. When the tight-binding is used to derive the electronic band structure of graphene, the explicit use of the equivalence of neighbors of a given order will no longer be valid if we want to use curvature.

In addition, there are also arguments from a quantum-mechanical and a symmetry point of view. In graphene the π orbitals cannot mix with the σ states because the former are strictly perpendicular to the sheet, whereas the latter are parallel.

However, calculations have shown that the curvature effect can be neglected except for very small diameter nanotubes, since the smallest nanotubes with a C_{60} fullerene diameter such as a (5, 5) nanotube would have only about a 2% decrease in the value for γ_0 due to nanotube curvature.[43]

A nonzero value for the overlap integral *s* modifies the electronic energy at the M point (edge center of the hexagonal Brillouin zone in FIG.1 from Ref. 43) from $\pm\gamma_0$ to $\pm\gamma_0 / (1 \pm s)$ for the $\gamma_0 > 0$. This was shown to result in asymmetry in the energy values for the π^* and π bands at the M point. However, while that is important for considering intraband optical transitions within either the conduction or valence bands for doped carbon nanotubes, when we consider the energy difference between the conduction and valence bands, the overlap effect or nonzero value for *s* is not so significant for energies less than 3 eV, since the energy difference at the M point is modified only by a factor $2\gamma_0/ (1 - s^2)$. Accordingly, the effect of a nonzero s value on the interband energy difference between VHS in the valence and conduction bands is only on the order of 10^{-2}.

On the other hand, and for SWNT's with diameters of around 1 – 2 nm and for excitation energies below 3 eV, which is the usual situation for observation of the resonant Raman scattering in SWNT's, the trigonal warping effect, addressed in greater detail in Ref. 43, becomes the most important of the three effects above. In that regard, it is sufficient to use experimentally measured transition energies to provide proper correction for the trigonal warping effect, and consequently for the calculated electronic structure. The electronic structure data used in our present study were calculated using tight binding method whereby calculations were performed after the implementation of such correction procedure.

1.4.4. Performance of SWCNTs as EDLC electrodes

Although the superior physical properties of SWCNTs rendered them promising candidate materials for EDLC electrode, the numerous investigations conducted on SWCNT EDLC electrodes.[34, 46−52] did not report high EDLC capacity values of SWCNT electrodes. This unexpected low capacity can be explained by the considerably low specific surface area of bulk SWCNTs, although the ideal specific surface area of an isolated open-end SWCNT is calculated to be 2630 m^2/g, identical to that of a graphene sheet. In the bulk SWCNT sample, SWCNTs form several aggregations bound by weak van der Waals interaction; therefore, the specific surface area of the bulk SWCNT sample becomes significantly lower than that of the isolated tube. In addition, the tube ends of some SWCNTs are closed by half fullerene caps, preventing ion adsorption inside the tube. Even if the tube end is open, it was not clarified whether electric double layers can form on the inner surfaces of SWCNTs with small diameters of 1−2 nm.

Furthermore, the electronic features of SWCNTs discussed above that suggest a unique, diameter-related electronic behavior were not reported. Although the cyclic voltammogram of SWCNTs did not resemble the classical rectangular shape observed for other carbon materials, it did not reflect any subtle electronic changes during electrochemical polarization, and rather showed a linear increase in capacitance with applied potential, which gave the voltammogram the often reported “butterfly” shape discussed in more detail in Chapter 2.

It is important to emphasize that the majority of SWCNT samples investigated in the past had low quality and purity, and wide diameter distribution, resulting in poor electrochemical performance that significantly deviated from theory. On the other hand, and with the recent advances in the understanding of SWCNTs, it is possible now to synthesize or isolate high quality and limited/specific diameter and chirality SWCNTs that will approach hypothetically anticipated properties. As a result, it becomes equally necessary to evaluate this new class of SWCNTs which includes among other fields, their performance as EDLC electrodes.

1.5. Purpose of the present study

In the present study, the mechanism of charge transfer is investigated in SWCNTs with controlled properties, used as EDLC electrodes. SWCNTs with high level crystallinity, low impurities, and narrow diameter distribution are used, and their electrochemical behavior is

addressed in connection to the two major elements influencing SWCNT electrode capacitance, which are the electronic density of states, and the surface structure of SWCNTs. The study was conducted in the following manner:

In **Chapter 2**, Using cyclic voltammetry (CV), the electrochemical behavior of highly crystallized small diameter distribution is investigated in different organic and aqueous electrolyte solutions. The study revealed for the first time a characteristic CV profile that is referred to later as the "dumbbell-voltammogram", which reflects the electronic structure of SWCNTs in the sample, and the origin of dumbbell voltammogram is verified by performing electrochemical measurements on SWCNTs separated into metallic and semiconducting SWCNTs, and also SWCNTs with different average diameters.

In **Chapter 3**, the possibility of ion adsorption inside SWCNTs is addressed and verified, and the difference between the nature of adsorption on the inner and outer surface of the tube is investigated. These elements are addressed by preforming CV electrochemical measurements at different scan rates, on closed-end and open-end SWCNTs, and in different aqueous and organic electrolytes. The electrode capacitance of inner and outer surface of SWCNTs was then simulated, and the difference in their ohmic resistance is quantified.

In **Chapter 4**, electrochemical measurements are combined with Raman spectroscopy to investigate the changes in charge carrier density leading to the dumbbell-like cyclic voltammogram of SWCNTs used as EDLC electrodes. The joined influence of both electronic and surface structure on the changes in charge carrier is investigated by *in situ* monitoring spectroscopic changes with applied potential for closed-end and open-end SWCNT samples using two laser excitation sources that probe either metallic or semiconducting SWCNTs in the sample. Unexpected spectroscopic changes are observed for metallic tubes, coinciding with the the potential of the two step-like jumps in the dumbbell voltammogram. The influence of surface structure on these spectroscopic changes is also clarified.

Finally, **Chapter 5** addressed the manipulation of electronic properties of SWCNTs through chemical and doping. Liquid phase chemical approach is used to dope SWCNTs with nitrogen, and the efficiency of doping of different SWCNT sample is discussed. In addition electrochemical measurements demonstrated the changes in EDLC electrochemical behavior of doped SWCNTs and the enhancement in the ion adsorption kinetics and total capacitance at high scan rate due to the improvement in electrode conductivity.

CHAPTER 2

CHAPTER 2

The Cyclic Voltammogram Profile of Single-Walled Carbon Nanotube Electric Double-Layer Capacitor Electrode

2.1. Overview

As discussed in chapter 1, the charge Q on a capacitor is proportional to the potential difference V, according to the relation $Q = CV$, where C is the capacitance. In ideal EDLCs, because the capacitance C is a constant, the cyclic voltammogram (CV) shape should be a rectangle. However, with SWCNTs that may not be the case. The electronic properties of single-walled carbon nanotubes (SWCNTs) play an important role in their electrochemical performance. When used as electrical double layer capacitor electrode materials under sufficiently high voltage window, SWCNTs go through the process of charge carrier injection into their electronic band structure. This increase in the charge carriers will increase the electronic conductivity of the electrode. Also, as the additional charge carriers are neutralized by the increase in the ion adsorption within the electrical double layer at the electrode-electrolyte interface, a significant increase in the electrode capacitance will be obtained. With this great potential for superior electrode performance of SWCNTs, their successful incorporation in energy storage devices will require correct understanding and evaluation of the charge carrier doping behavior of SWCNTs.

Nevertheless, the observed CV shapes of SWCNT electrodes reported in previous papers had a symmetrical and steady increase of the current density, proportional to the potential in both sides of the open-circuit voltage (OCV). This CV shape resembles a butterfly. The origin of this butterfly shape was extensively discussed in many papers,[46–52] the majority of which reported that carrier doping into the semiconducting SWCNTs was responsible for this shape. However, it remains unclear whether SWCNT carrier density increases proportionally to potential with increasing/ decreasing potential.

It is widely accepted that the electronic density of states (DOS) of SWCNT is quite characteristic. The presence of van Hove singularities results in numerous peaks (kinks) in the

DOS. Therefore, the increase of carriers proportional to potential is unlikely. The position of van Hove singularity depends on the chirality of the SWCNT, and many SWCNTs with various chiralities should be included in a sample. Therefore, we should consider the overlap of SWCNTs and DOS. As previously mentioned, the ion adsorption mechanism of SWCNT EDLC electrodes is not clearly understood, although extensive research has been conducted on SWCNT EDLC electrodes.

Unfortunately, most of the previous studies involved SWCNTs with relatively low crystallinity produced by chemical vapor disposition (CVD) method, probably because this method was the only way to produce sufficient amounts of SWCNTs for electrochemical measurements. However, to elucidate the ion adsorption mechanism of SWCNT EDLC electrodes, several precise electrochemical measurements using well-defined SWCNTs having high crystallinity are required. This chapter presents the electrochemical measurements for SWCNTs produced by arc-discharge method with high crystallinity and narrow diameter distribution. The results show a characteristic size-dependent cyclic voltammogram of SWCNTs of different diameters.

2.2. Experimental

2.2.1. Preparation of samples

The sample of SWCNTs used in the present study was produced by arc discharge (Meijo Nano Carbon Co. Ltd., SO type), and had high crystallinity and narrow diameter distribution. First, as-grown sample was purified to remove any metallic catalyst and amorphous carbon impurities, resulting in low level of non-carbon impurities (3%). Then the purified sample was annealed under vacuum at 1200 °C for 14 hours to close the defects on the walls of the tubes and further improve their crystallinity.[53] The annealed SWCNT sample was then decapped by heating the closed-end SWCNTs at 450 °C in air for 20 min to remove their head caps resulting in open-end SWCNTs. The temperature required to open the tube end was determined by thermogravimetric analysis (TGA) data (Figure 2.1).

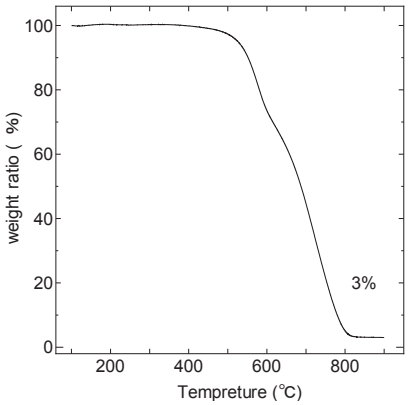

Figure 2.1: TGA analyses for the SWCNT sample, the purified sample contained 3% non-carbon impurities.

2.2.2. Characterization of samples

The surface properties of the sample were thoroughly characterized using several techniques. Scanning electron microscopy (SEM) images of the sample were probed using Field Emission Scanning Electron Microscope (FESEM), and by elemental analysis using Energy Dispersive X-ray Detector (EDX) with JSM-7001FF (JEOL) microscope.

Raman spectroscopy measurements were performed using three different nitrogen-cooled excitation sources: argon (λ =514.5, E_L = 2.4 eV), green Nd:YAG laser (λ = 532, E_L = 2.33 eV), and red helium-neon laser (λ = 632.8, E_L = 1.96 eV). Multiple excitation sources were used because Raman spectra are strongly affected by the resonance effect. The spectra excited by 514.5 nm argon lasers were collected using a Raman microscope system equipped with the Acton SP 2300 charge-coupled device (CCD) detector (Princeton Instrument). The spectra excited by 532.1 nm Nd:YAG laser and 632.8 nm helium− neon lasers were collected using NRS 3300 (JASCO) spectrometer.

Although multiple excitation sources were used, Raman spectroscopy is not a proper method to determine the mean tube diameter of all the tubes existing in the sample. Raman scattering from SWCNTs is dominantly in resonance process and only a very small set of tubes participate in this process. Therefore, powder X-ray diffraction (XRD) measurement of the SWCNT sample was performed, and the mean tube diameter was determined by simulating the observed XRD pattern. Because of the low scattering factor of SWCNTs, high brightness synchrotron

XRD measurements were performed using beamline BL-18C at the Photon Factory (PF), High Energy Accelerator Research Organization (KEK) in Tsukuba, Japan. The experiments were conducted using X-ray (wavelength: 0.614 Å) monochromatized by Si (111) double-crystal monochromator. Diffraction patterns were collected using a two-dimensional imaging plate (IP) detector located 160 mm behind the sample position. The X-ray wavelength and the distance from the sample to the IP were calibrated on the basis of the X-ray diffraction peaks of CeO_2 powder using the double cassette technique, through IPAnalyzer software.[54] To eliminate the preferred orientation effect, the quartz capillary tube that contained the sample was oscillated during the measurement process. The obtained XRD pattern was corrected for the influence of Lorentz-polarization factor prior to further analysis.

The obtained XRD patterns were assigned as the diffraction of a two-dimensional hexagonal structure. To estimate the lattice parameter *a*, and the tube radius R of the SWCNTs, pattern simulation were performed in which the SWCNT form factor was assumed using the 0th order cylindrical Bessel function.[55]

UV−Vis−NIR absorption spectra were collected using a UV- 1600 spectrophotometer (JASCO). For the measurements, 0.001 g of SWCNTs was mixed with an equal weight of sodium cholate surfactant and 0.1 g of distilled water. The mixture was sonicated for 20 min using a tip-type ultrasonic disruptor UD- 201 (TOMY).

2.2.3. Electrochemical measurement

Electrochemical (cyclic voltammetry and charge−discharge) measurements were conducted using a potentiostat/galvanostat (Hokuto Denko) controlled by a computerized system (Figure 2.2). A specially designed cell with a conventional three-electrode configuration was used. In the cell, the SWCNT sheet sample and activated carbon sample on platinum mesh current collector were used as working and counter electrodes, respectively. The electrolytes used included NaI, NaCl, and NaBr aqueous solutions and 1.0 M triethylmethylammonium tetrafluoroborate ($TEMABF_4$) in propylene carbonate (PC) organic electrolyte. Ag/AgCl electrode was used as reference electrode for the aqueous electrolytes, and Ag/Ag^+ reference electrode was used $TEMABF_4$. Cyclic voltammetry measurements were conducted at scan rate 5 mV/s. An argon-filled dry-box was used as the measurement environment using $TEMABF_4$. Cyclability was checked by performing galvanostatic charge−discharge measurements with

current densities between 50 and 1000 mA/g.

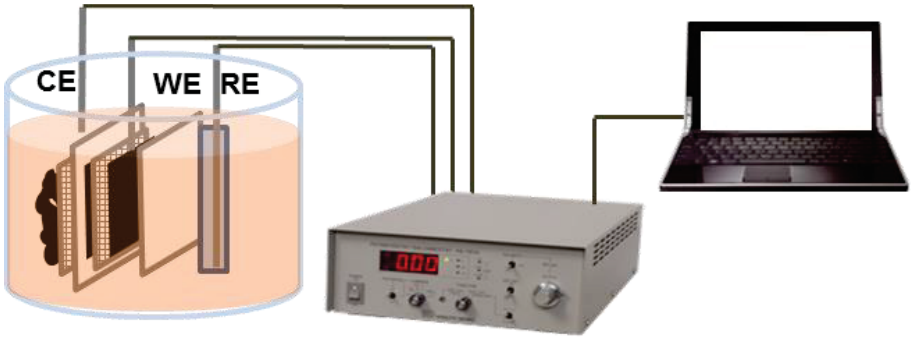

Figure 2.2: Electrochemical measurement cell. WE: working electrode, CE: counter electrode, and RE: reference electrode.

2.3. Results and discussion

Scanning electron microscopy (SEM) image of the sample are seen in Figure 2.3, showing the well-defined rope structure and bundle entanglement of the sample utilized.

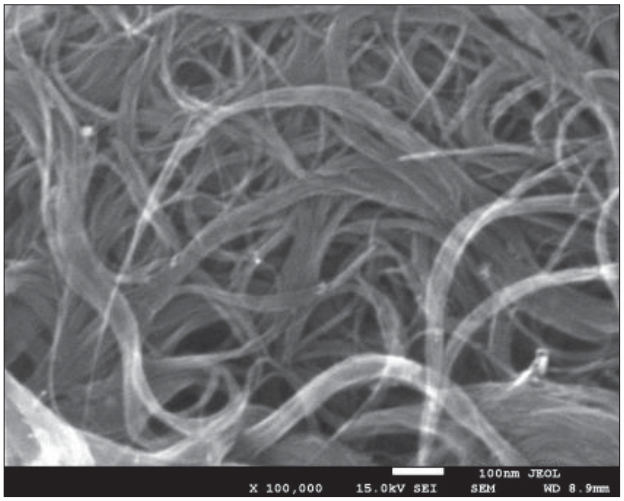

Figure 2.3: SEM images of the SWCNT sample.

Raman spectrum of the SWCNT sample is seen in Figure 2.4. The level of crystallinity of the sample can be judged from the disorder-induced D-band appearing around 1330 cm^{-1}, whose

intensity increases with the level of defects on the tube surface. The sample probed in Figure 2.4 shows a high level of crystallinity as seen from the very low intensity of the D-band.

The shape of the G-band peak observed at approximately 1590 cm^{-1} for the 632.8 nm laser was asymmetric and significantly broader than that observed in other excitation sources. The asymmetric peak profile of the G-band shown in Figure 2.4(C) exhibited a Breit−Wigner−Fano feature because of the existence of metallic SWCNTs in the sample.

The peaks seen on the low frequency region between 100 and 200 cm^{-1} are known as the radial breathing mode (RBM), and their peak position correlates inversely with the tube diameter. The RBM peaks from various laser types show small diameter distribution despite the change in laser source intensity. The values of SWCNT diameters calculated from these RBM positions[56] were in the range 1.46–1.67 nm.

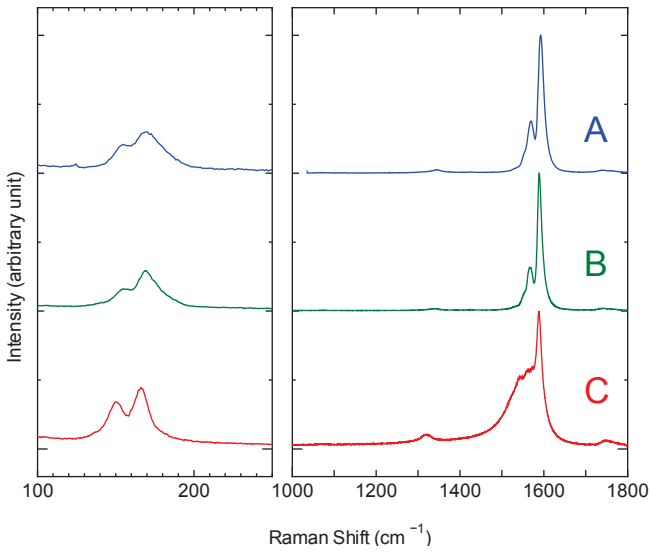

Figure 2.4: Raman spectra of open-end SWCNT sample probed using (A) 514.5 nm (B) 532 nm, and (C) 632.8 nm laser.

Cyclic voltammetry curve of the open-end SWCNTs sample in $TEMABF_4$/PC organic electrolyte taken at a sufficiently low scan rate (5 mV/s) is shown in Figure 2.5.

Contrary to any results reported so far on the cyclic voltammogram of SWCNTs, the cyclic voltammogram shape obtained here did not resemble the typically obtained “butterfly” shape previously observed by other researchers. Rather, first the voltammogram had a region in the middle (at a potential close to the OCP around –0.31 V) where the capacitance maintained a

constant value. Then, the capacitance showed an abrupt and significant increase at potential values (-0.05 V) and (-0.65 V). That sudden jump in capacitance led to the formation of two distinct steps on both the cathodic and anodic scans of the voltammogram, creating the final shape of a "dumbbell". The region of low capacitance in the middle will be referred to as the "dumbbell grip", and the two potential values where the steps appear will be called the "step potentials"

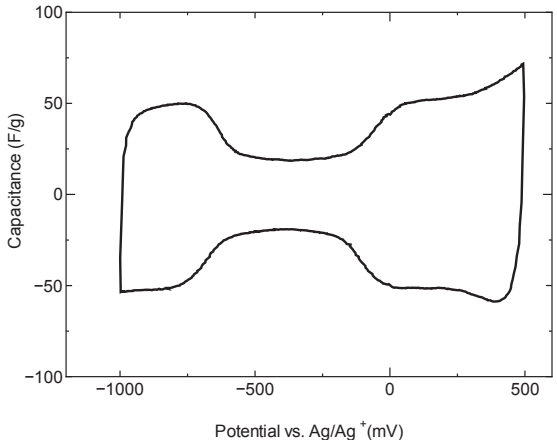

Figure 2.5:The cyclic voltammogram for decapped (open-end) SWCNT sample in TEMABF4/PC obtained at scan rate 5 mV/s.

Taking the electronic structure of SWCNTs into consideration, it is assumed that the origin of the step-increase in capacitance and the dumbbell shaped-voltammogram can be explained by electrochemical response following up the doping process of SWCNTs. However, one must also consider the possibility that the steps are the results of redox reactions. In that regard, two facts must be noted: the first is that from previous studies involving covalent[57] and non-covalent modification of SWCNT, [58] it was shown that the redox reactions of functional groups are not likely to invoke a significant modification to the electronic density of states of SWCNTs. The second fact is that reduction–oxidation reactions manifest on the cyclic voltammogram in the form of two peaks located symmetrically at around the open circuit voltage. The shape of the humps obtained in Figure 2.5 suggests that the peaks are located at the same values of the applied potential, and thus, peak separation and symmetry are absent around the open circuit voltage. It is also evident that instead of being sharp, the peaks are ''stepped''.

The other possibility is that these steps could have been produced accidentally by the

measurement system including the potentiostat, test cell, and electrolyte. To address that possibility, a different SWCNT sample (Meijo nano Carbon, FHP type) that had a relatively wide diameter distribution of 1−2.5 nm (Figure 2.6) is used. Upon performing CV measurement for that sample (Figure 2.7), a butterfly CV shape was obtained, hence dismissing the possibility of experimental error. This indicates that the steps were not caused by experimental errors and should have been caused by the essential nature of SWCNTs, and further enhances the density of states of SWCNTs as the origin of the dumbbell-shaped voltammogram.

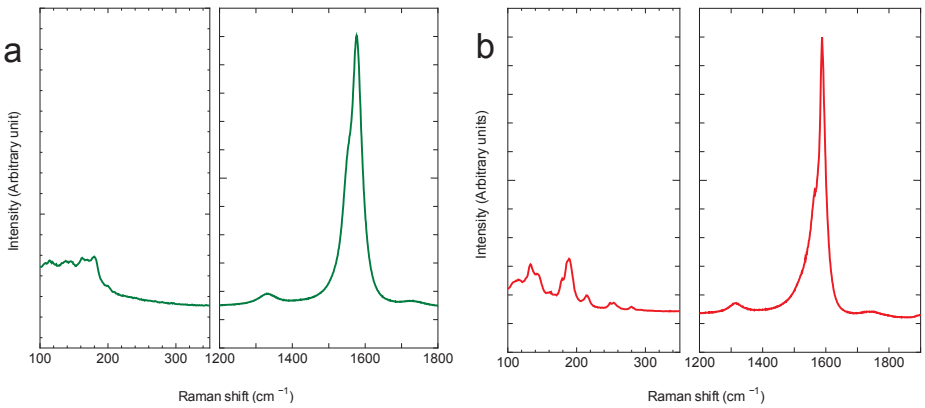

Figure 2.6: Raman spectra for FH-P type SWCNTs, probed using (a) 532 nm and (b) 632.8 nm laser.

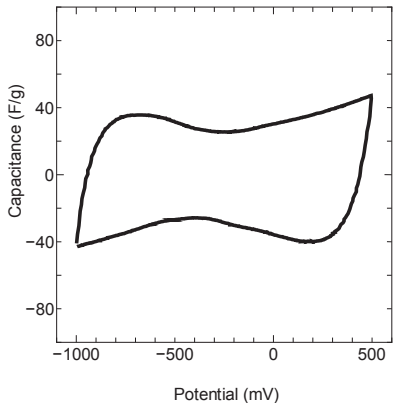

Figure 2.7: Cyclic Voltammetry for FH-P type SWCNT in TEMABF4/PC at 5mV/s. The sample has wide diameter distribution (1–2.5 nm) and displays a butterfly CV profile.

The relationship between the dumbbell CV shape and the electronic structure of the SWCNTs used in the present study is considered. As stated in the Introduction regarding the

origin of the butterfly CV shape, it was discussed that the current increase proportional to potential was caused by carrier doping into the semiconducting SWCNTs. To examine whether a similar explanation is possible for the present experimental result of the dumbbell shape, the electronic structure of the SWCNTs used in the present study, including the chiralities, should be determined. Infrared photoluminescence (PL) is a widely accepted method used to determine the chirality indices of SWCNTs. However, because this method is valid for only semiconducting tubes, it is not appropriate for the present study. For our sample, as seen for Raman spectra, the diameter distribution of the SO type SWCNTs used is considered to be quite small. Therefore, the chiralities should be limited. If the mean tube diameter can be determined and the estimated error of the determined diameter is evaluated, the chiralities should be restricted in a limited range.

For that purpose, XRD is a powerful tool that enables the determination of a mean diameter of SWCNTs in each sample. Figure 2.8 shows the observed XRD pattern for samples A and B. The intense diffraction peaks indicate that the SWCNT sample used in the present study was well crystallized with a rather small diameter distribution. The observed peak positions could be indexed as a two-dimensional hexagonal space group, which can be explained by the SWCNTs' bundle structure. Accordingly, pattern simulations were performed through XRD to determine the lattice parameter *a* (1.79 nm), and the tube radius R (0.74 nm). These values are in agreement with the values obtained using Raman measurements.

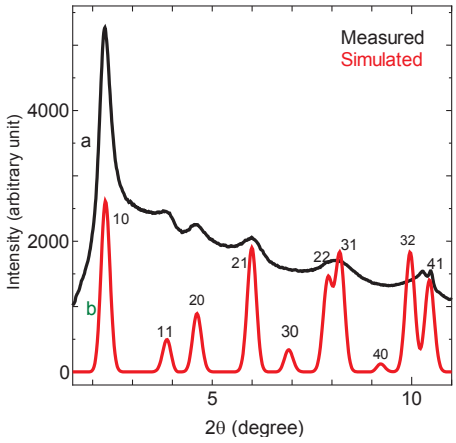

Figure 2.8: XRD measurements and pattern simulations for SWCNT sample.

Despite the fact that these two parameters (*a*, R) correlate empirically and are difficult to

obtain simultaneously, the simulated pattern well reproduces the observed pattern. With use of the determined *a* and R values, the tube-to-tube distance was calculated to be 0.31 nm, which is slightly less than the layer distance of graphite (0.335 nm). This distance is quite reasonable because the graphene sheet bends in the case of SWCNTs, thereby weakening the van der Waals interactions. Unfortunately, statistical determination of estimated errors for the determined parameters *a* and R is impossible. But if the value of parameter R was changed by 0.05 nm from the determined value (0.74 nm), it would be difficult to obtain good accordance between the simulated and observed patterns. Therefore, using this simulation, mean tube diameter was determined as 1.48 nm at a minimum resolution within 0.1 nm.

In this condition, the chirality candidates can be restricted in a limited range. In this range, (17, 3) and (15, 6) chiralities were obtained for the representative semiconducting and metallic tubes in the present SWCNT sample, respectively.[59] The diameters of (17, 3) and (15, 6) tubes were 1.483 and 1.487 nm, respectively. The electronic structures of these two tubes are considered (Figure 2.9). Although the other chirality tubes were included in the sample, the changes in DOS of the other metallic and semiconducting tubes from the DOS of (17, 3) and (15, 6) tubes were negligible for the following discussion if the tube diameter was 1.48 ± 0.1 nm. Comparing the DOS of (17, 3) and (15, 6) tubes, the energy gap of van Hove singularities of the semiconducting (17, 3) tube was much smaller than that of the metallic (15, 6) tube. In the semiconducting SWCNT case the gap from Fermi energy to the first singularity was about 0.3 eV (E_{11}^{S} ~ 0.56 eV). Therefore, if the (17, 3) tube is used as an electrode, the carrier density of the electrode dramatically changes when the electrode potential is altered by about 0.3 V from the open-circuit potential. This change may have caused the increase in ion adsorption on the electrode surface, which led to the increase of EDLC capacitance. The steps in the observed dumbbell CV shape should correspond to this carrier density change. The previously observed "step potentials" are located at distance of about 0.26 V in the positive side and at 0.34 V in the negative side from the open-circuit potential, hence are in good agreement with the energy gap from Fermi energy to the first van Hove singularity points of the semiconducting tubes.

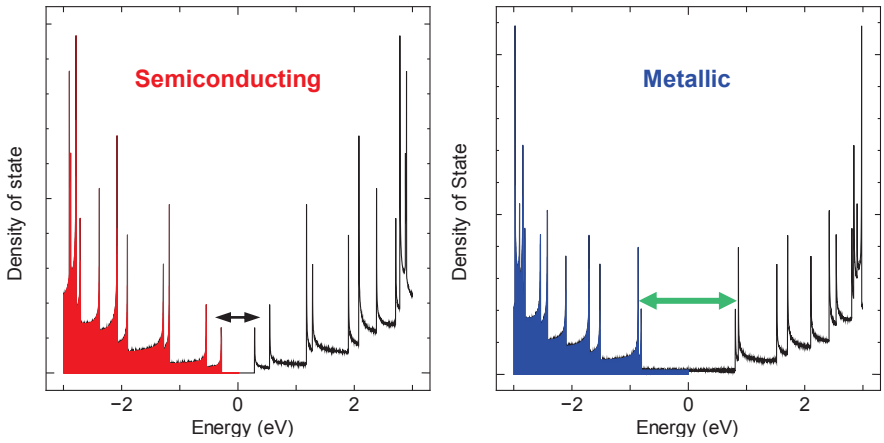

Figure 2.9: Electronic density of states (DOS) of (17, 3) semiconducting and (15, 6) metallic SWCNTS.

From the above discussion, it is plausible that the origin of the dumbbell CV shape can be explained by the characteristic DOS of the semiconducting SWCNTs used in the present study.

According to our hypothesis, if the CV shape of the pure metallic SWCNTs is measured, the two steps would not be observed in the same potential range as in Figure 2.5 because the energy gap of the metallic (15, 6) tube from Fermi energy to the first van Hove singularity points was approximately 0.8 eV.

Therefore, the separation of SWCNTs into metallic and semiconducting tubes was performed by the density gradient ultracentrifugation method. The observed UV−Vis spectra of the two separated samples in Figure 2.10 indicate that the separation was fairly efficient. Figure 2.11 shows the observed CVs of the separated metallic and semiconducting tubes. The observed CV curves were noisy because the amounts of the finally obtained metallic and semiconducting tubes were very small. However, it is evident that the CV curves of these two samples differ significantly. As expected, no bulges were observed in the CV curves of the metallic SWCNT sample in contrast to that of the semiconducting tube. If the potential range is expanded, bulges in the CV of metallic SWCNTs are expected, and secondary bulges corresponding to the second van Hove singularity points should be observed in the case of the semiconducting SWCNTs. However, no bulges were observed except for the first bulges of the semiconducting tubes in the CV curves in wider potential range, probably because the electric conductivity changes dramatically only at the first singularity points of the semiconducting tubes.

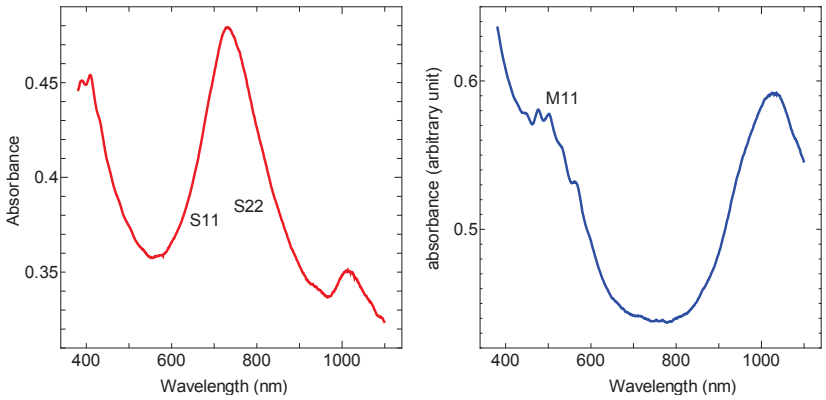

Figure 2.10: UV−Vis spectra of the separated semiconducting and metallic samples.

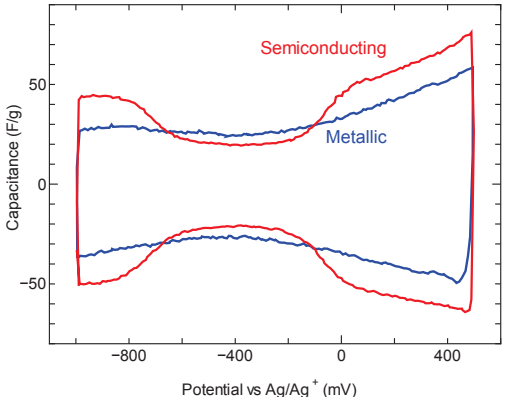

Figure 2.11: Cyclic voltammograms of the separated metallic and semiconducting SWCNTs in TEMABF$_4$/PC.

In addition to the evidence obtained from Figure 2.11, it remains important to reproduce the dumbbell voltammogram irrespective of the electrolyte medium, which will not only as final confirm the intrinsic nature of the dumbbell voltammogram, but also provide insight on any possible contributions from redox-like charge transfer as alternative or additional probable cause behind the step increase in capacitance. As discussed above, were reduction–oxidation to appear on the cyclic voltammogram, they would have the form of two peaks symmetrical around the open circuit voltage. The peak separation distance and height of these peaks are functions of the characteristics of the electrolyte. They may vary in height or disappear depending on the type of the electrolyte used. To gain insight into this latter issue the same samples must be tested in different electrolytes under potential window that gave rise to the

dumbbell shape.

To produce the dumbbell voltammogram, it is required to apply potential whose value is high enough to achieve an energy transition between two symmetric VHSs separated by a band gap of about 0.56 eV (E_{11}^{S} for semiconducting SWCNT with diameter 1.48). In other words, the potential window must extend to about 350 mV to each side of the center of the dumbbell grip (a total potential window of 700 mV). However, the potential window should not be extended to the extent that may cause the electrolyte decomposition. For this reason, an electrolyte such as aqueous H_2SO_4 should be avoided since it will give rise to redox peaks on the cyclic voltammogram, and obstruct any analyses of the changes occurring on the voltammogram in terms of the electronic density of states.

Therefore, CV measurement was repeated for the same sample using 1.0 M NaCl, NaBr, and NaI aqueous solutions as electrolyte mediums (Figure 2.12), and the results clearly show that the dumbbell shape was obtained once again with similar "grip width" to that shown in Figure 2.5, followed by an abrupt increase in the electrode capacitance. The value of the total capacitance will naturally depend on the electrolyte type, but the shape of the voltammogram and the grip distance remain a function of only the tube characteristics.

It is therefore concluded that the dumbbell-shaped cyclic voltammogram reflected the characteristic electronic structure of SWCNTs, and correlate to the energy band gap on the DOS of SWCNTs in the sample. Subsequently, step-like increase in capacitance values occurs as the results of the increase in the number of charge carriers supposedly providing additional energy to adsorb more ions on the surface of the tubes, increasing the electrode capacitance.

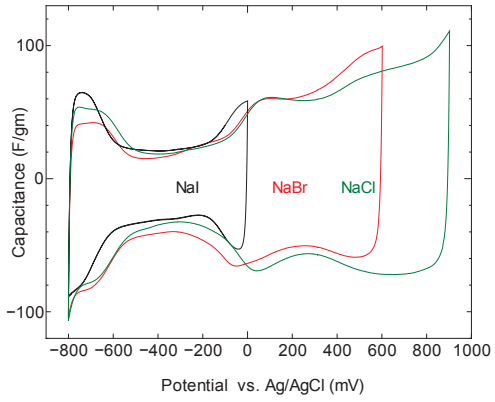

Figure 2.12: Cyclic voltammograms of SWCNTs sample in NaCl, NaBr, and NaI, showing dumbbell shapes.

Finally, the legitimacy of our hypothesis can be further confirmed if it proved valid for other SWCNTs with different mean diameters. In that case the width of the dumbbell grip must correlate with the mean diameter of the SWCNTs in that sample. For this purpose, two other samples were investigated, and had narrow diameter distribution but different mean diameters as seen from their Raman spectra in Figure 2.13.

The first sample is synthesized by laser ablation method (obtained from the Faculty of Science, Chiba University, Hattori type). It had high crystallinity, as seen from the D-band on the spectra in Figure 2.13. From XRD measurement and pattern simulation (Figure 2.14), a mean tube diameter of 1.36 nm was determined for the sample. This diameter corresponds to (16, 2) and (14, 5) SWCNTs semiconducting and metallic tubes that were used as the representative chiralities.

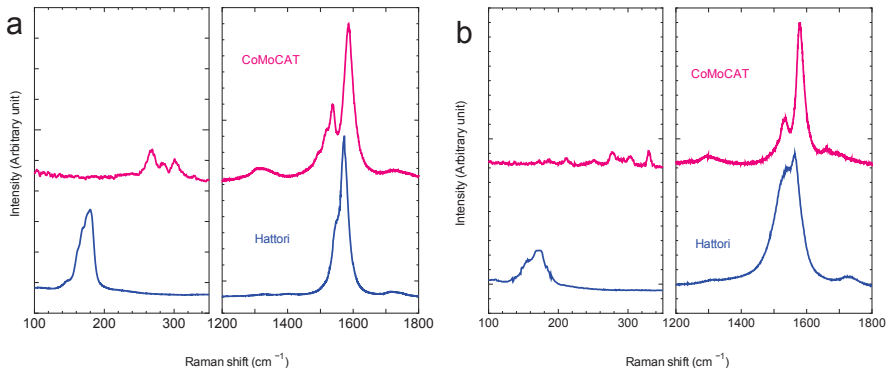

Figure 2.13: Raman spectra of two SWCNTs samples, probed using (a) 532 nm laser and (b) 633 nm laser.

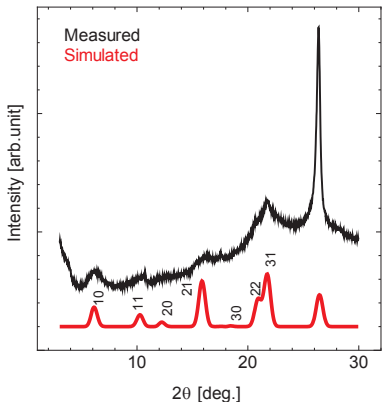

Figure 2.14: XRD measurements and pattern simulations for the SWCNT sample produced by laser ablation.

The other sample was produced by CVD (CoMoCAT®) method, and with low crystallinity that did not allow the observation of clear XRD patterns. However, the sample is enriched with semiconducting SWCNTs of mean diameter 0.75 nm and chirality (6, 5), which was used as the representative chirality to obtain the density of states data for the purpose of comparison.

CV measurements were performed for those two samples, and dumbbell-like voltammograms were obtained again. The dumbbell shape for the sample produced by CVD method is not well defined, which may be explained by its lower level of crystallinity compared to the other sample. Nevertheless, the voltammogram remains closer in shape to a dumbbell than to a butterfly.

The width of the dumbbell grip of each voltammogram is compared with the band gap energy E_{11}^{S} of the representative semiconducting tubes, which again resulted in close accordance between these two values as seen in Figure 2.15 below.

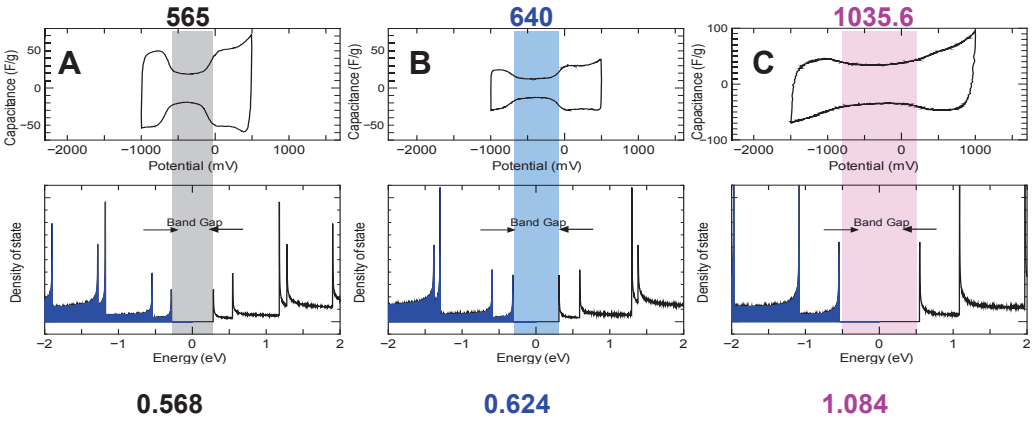

Figure 2.15: Comparison between band gap energy and grip width of three samples (A) d_t = 1.48 nm (B) d_t = 1.36 nm (C) d_t = 0.75 nm.

It should be noted that all the previous measurement were performed using open-end SWCNTs. When annealed (closed-end) samples were used, the dumbbell voltammogram was maintained but had a less defined shape, and the values of electrode capacitance were less than those obtained with open-end samples in the same electrolyte. This feature is related to the ion adsorption on the inner surfaces of SWCNTs. the consequence of using decapped SWCNTs as EDLC electrodes reflects not only on the obtained capacitance but also on the kinetics of ion adsorption, which will be discussed in detail in chapter 3.

2.4. Conclusion

The electrochemical behavior of highly crystallized SWCNT with small diameter distribution, demonstrated by cyclic voltammetry, displayed a distinct dumbbell shape rather than the typically expected butterfly shape. This shape resulted from the DOS of semiconducting tubes in the SWCNT sample. The dumbbell voltammogram includes a characteristic signature of the tubs' electronic structure in the region called the dumbbell grip, which was shown to correlate with SWCNT diameter and chirality irrespective of the electrolyte used. This behavior can be observed only in SWCNT with high crystallinity and narrow diameter distribution that represent more accurately the actual electrochemical behavior of SWCNTs.

CHAPTER 3

CHAPTER 3

Ion Adsorption on the Inner and outer Surface of Single-walled Carbon Nanotubes used as Electrodes for Electric Double-layer Capacitors

3.1. Overview

As energy storage electrode material, single-walled carbon nanotubes (SWCNTs) have well defined and controllable tubular morphology that promises with superior ion accessibility in compared to activated carbon whose intrinsically random and extremely complicated porous structure imposes a limitation on both the ion transfer inside the pores and the possibility of controlling the structure.

SWCNTs offer moderate surface area that can potentially be increased, as was previously accomplished by growing the nanotubes as vertically aligned forests [60] or by creating windows on their walls to utilize their inner surfaces as ion adsorption sites.[61] SWCNTs potentially have three adsorption sites: the outer surface of the bundle of tubes, the interstitial space between tubes, and the space inside the tubes. In regards to the latter, previous experiments that investigated lithium intercalation or methane and fullerenes filling into SWCNTs, demonstrated an increase in the amount of the stored species upon etching or creating defects, which might provide additional access inside the tubes to the diffusing species.[62] However, the potential advantage of the space inside SWCNTs may not be limited to the additional storage space; this internal space predictably provides superior confinement properties. The nano-size induced capillary action was shown to lead to absorption of dipolar molecules and efficient filling of SWCNTs.[63] Also, the confinement of material within the nanoscale space in carbon nanotubes has been reported to induce peculiar physical phenomena that are different from those in the bulk phase; for example, the quasi-high pressure effect had diverse effects on the confined material, [64, 65] such as super compression resulting in a high-pressure phase structure.

Considering this particularity in behavior, it becomes important for EDLC applications to not only to realize the highest possible surface area, but also to define where and how ions are

stored in a polarized SWCNT electrode, and the characteristics of capacitance in each adsorption site.

In chapter 2, it was demonstrated that unlike other carbon materials, the electrochemical behavior of SWCNTs is also influenced by their electronic structure. Due to the unique one-dimensional electronic density of states of SWCNTs, the variation in their charge carrier density and electrode capacitance is expected to be conspicuous and well-defined in relation to the applied potential. The qualitative shape of the obtained cyclic voltammogram was dependent on the tube diameter and chirality, irrespective of the electrolyte medium. The experiments performed in chapter 2 used open-end SWCNT samples, and were done with slow scan rate to allow sufficient time for ion adsorption to take place.

This chapter investigates ion storage and electrochemical behavior in closed-end and open-end SWCNTs, in different electrolyte solutions, and under different potential scan rates. The results provide insight on the difference between the outer and inner surfaces of SWCNTs in terms of the electrode capacitance, and noticeable changes in the manner of ion adsorption.

Differences between the voltammograms of open-end and closed-end SWCNT polarized under the same conditions point toward the difference in surface structure that influences the ion adsorption behavior. In addition, the use of different electrolytes offers information related to the role of ion type on electrode resistance and performance.

3.2. Experimental

3.2.1. Preparation and characterization of samples

The sample used in this chapter is the same SWCNT sample used in chapter 2. As previously mentioned in chapter 2, the as-grown samples were purified to remove catalyst impurities and heat-treated at 300 ˚C to remove amorphous carbon.

The sample was probed with Raman spectra excited by three laser sources (λ =514.5, 532, and = 632.8 nm) as indicated previously in chapter 2.

Two sample types were prepared: closed-end and open-end. The closed-end SWCNTs were prepared by annealing the purified samples at 1200 ˚C for 14 hours under vacuum.[53] The open-end SWCNTs were prepared by heating the closed-end SWCNTs at 450 °C in air for 20 min.[66] In order to verify the success of the decapping treatment, nitrogen adsorption/desorption

measurements were performed to evaluate the specific surface area of both closed-end and open-end samples. The measurements were performed at 77 K using a Gemini 2375 (Shimadzu).

3.2.2. Electrochemical measurement

All electrochemical measurement were conducted using a potentiostat/ galvanostat (Hokuto Denko) controlled by a computerized system. The same three electrode cell illustrated in Figure 2.2 was used for all measurements, with an SWCNT sheet sample and an activated carbon sample on a platinum mesh current collector as working and counter electrodes, respectively.

CV measurements were performed using three electrolyte solutions: aqueous 1.0 M H_2SO_4, 1.0 M NaCl, and organic 1.0 M triethylmethylammonium tetrafluoroborate ($TEMABF_4$) in propylene carbonate (PC). Ag/Ag^+ was used as reference electrode with $TEMABF_4$/PC, while Ag/AgCl was used for aqueous electrolytes. CV measurements were conducted at scan rates between 5 and 100 mV/s. An argon-filled dry box was used as the measurement environment for the organic electrolyte. Charge–discharge measurements were performed in the three electrolytes with current densities between 50 and 1000 mA/g.

3.3. Results and discussion

The Raman spectra of closed-end and open-end SWCNT samples are shown in Figure 3.1. The spectra show that Raman spectrum of the open-end SWCNT sample was nearly the same as that of the closed-end sample. Both closed-end and open-end SWCNT samples are well crystallized and have few defects on their surface structure, as is evident from the intensity of the D-band for both samples. The narrow diameter distribution in the samples is indicated by the narrow range of the RBM band, as shown in Figure 3.1.[56]

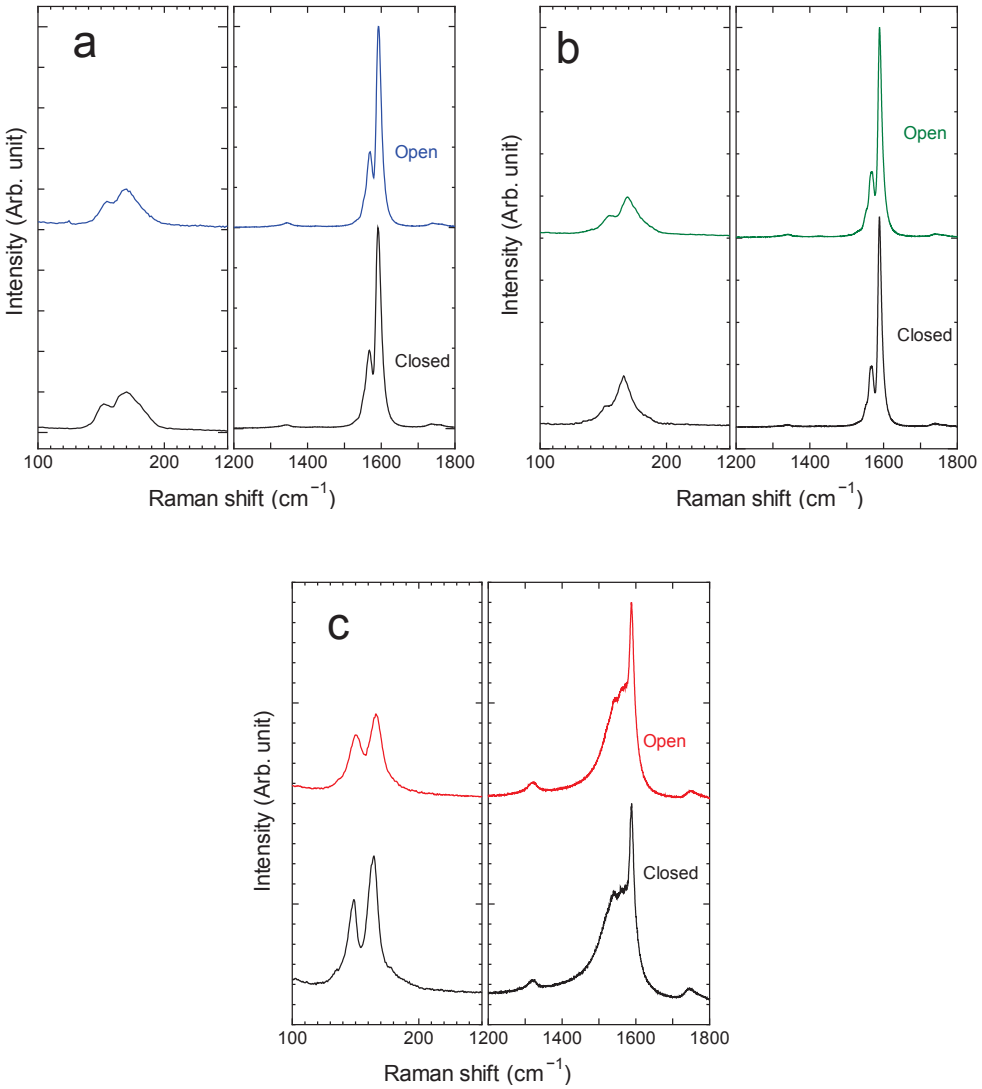

Figure 3.1: Raman spectra of sample A using (a) 514.5 nm (b) 532 nm, and (c) 632.8 nm laser.

Although Raman results indicate that the heat treatment for decapping induced few or no defects on the surface of the SWCNTs, the results of nitrogen adsorption measurement show drastic changes in Brunauer−Emmett−Teller surface area (S_{BET}). Closed-end sample had surface area 629 m^2/g versus 1011 m^2/g for open-end SWCNT sample (Figure 3.2).

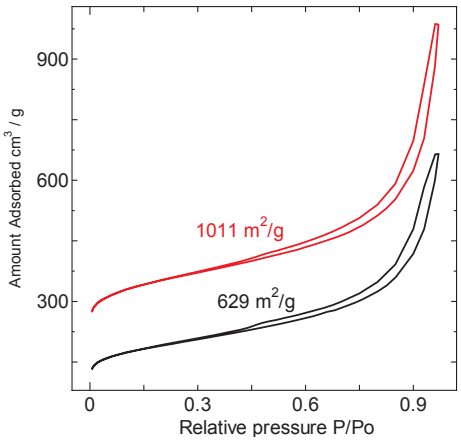

Figure 3.2: Nitrogen adsorption isotherms of closed-end (black line) and open-end (red line) SWCNT samples.

From the cyclic voltammograms for closed-end and open-end samples in $TEMABF_4$/PC in Figure 3.3, it can be seen that the dumbbell shape previously discussed in chapter 2 is seen for both closed-end and open-end samples. Both voltammograms of each sample resemble a dumbbell with a ‘‘grip’’ shaped region near the open circuit voltage followed by an increase in the capacitance, resulting in two step-like steps on both sides of the voltammogram.

However, it can be seen that the height of the dumbbell step (electrode capacitance) for the open-end samples is greater than that of closed-end SWCNT samples.

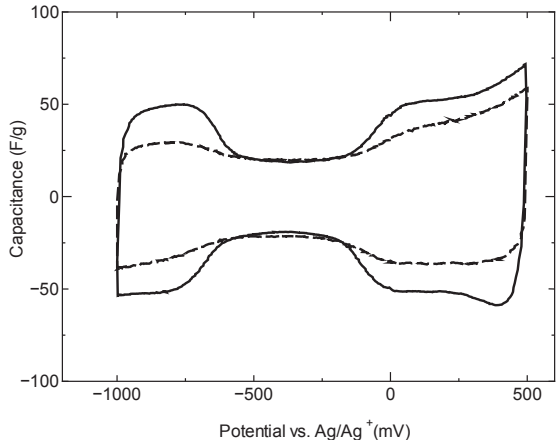

Figure 3.3: Cyclic voltammograms of closed-end and open-end SWCNTs in $TEMABF_4$/PC at scan rate 5 mV/s

The capacitance values in the dumbbell ‘‘step’’ region show that open-end SWCNTs have higher capacitance than closed-end SWCNTs. This apparently occurs in the post-doping stage

after the applied potential reaches the value that initiates carrier doping, which suggests that the increase in the number of charge carriers provides sufficient energy to push the ions inside the decapped tubes, and this additional ion adsorption could have increased the obtained capacitance. It can be dismissed that other factors may have caused the additional capacitance in open-end tubes, like functional groups or defects that may have resulted from the decapping treatment. To begin with, Raman spectra of the decapped samples (Figure 3.1) show that the intensity of the D-band for samples was maintained, which indicates that tube decapping could not have caused variation in the level of defects could. Also, the nitrogen adsorption measurement (Figure 3.2) shows that the S_{BET} of the decapped tubes is significantly higher than that of closed end tubes, hence open-end SWCNTs definitely had more space for possible additional ion adsorption.

Before the ion adsorption inside the tubes is considered, it is important to observe another observation concerning the region referred to as the ‘‘dumbbell grip’’ in the middle of the voltammograms in Figure 3.2. In that region the value of electrode capacitance of open-end tubes is similar to that of closed-end tubes. It was also observed from the values of capacitance calculated from charge/discharge measurements, that the capacitance per unit surface area of closed-end sample (4.9 $\mu F/cm^2$) was higher than that for open-end sample (3.6 $\mu F/cm^2$). This suggests that the ion adsorption at low applied potential is not favorable on the inner surface of the tube due to the constrained nature of the surface inside the tubes. The unfavorable free energy of the removal of solvation shells offers one possible explanation for the observation that open-end tubes have capacitance value similar to their closed-end counterparts at low applied potential.[67, 68] In other words, our observation suggests that depending on the ion size the wetting of the electrode pores with the electrolyte ions may or may not take place as a function of the applied potential, which seems to contradict the hypothesis that the electrode pores are completely wetted with the electrolyte even at the open circuit potential.[67]

Next, to consider the adsorption inside SWCNTs, the ‘‘grip’’ region is disregarded and the focus will be on the dumbbell step region. In this potential range, the capacitance of open-end tubes is higher than that of closed-end tubes. Therefore, ion adsorption seems to occur inside the tubes in the region of the dumbbell step. Thus, it is postulated that the characteristics of ion adsorption behavior in the step region are related to the specific nature of the space inside open-end SWCNTs. Unlike chapter 2, this time H_2SO_4 can be examined within this window

without decomposition. To analyze the ion adsorption behavior, cyclic voltammetry was performed in several electrolyte solutions at varying scan rates.

Neglecting the grip region, a potential between 0 and 800 mV was selected to investigate ion adsorption inside the SWCNTs. Over this range, the capacitance value of open-end tubes may be significantly higher than that of closed-end tubes. In the selected potential range, CV curves were investigated for H_2SO_4 (Figure 3.4) NaCl (Figure 3.5) in addition to $TEMABF_4$/PC (Figure 3.6) solutions. Figure 3.4 and 3.5 show the effect of decapping on the electrode capacitance; the capacitance of open-end tubes in both electrolytes is higher than that in closed-end tubes. It can be postulated that additional ion adsorption was taking place inside decapped tubes in both electrolytes, resulting in additional capacitance. Also, the two electrolytes seem to be different in terms of ion adsorption behavior inside SWCNTs. The CV curves for closed-end tubes in three electrolytes (Figures 3.4a, 3.5a and 3.6a, respectively) maintain uniform shape despite the increase in the scan rate. On the other hand, the shape of cyclic voltammograms and the values of the capacitance in open-end tubes apparently vary depending on the type of the electrolyte. With H_2SO_4 (Figure 3.4b), there is no deformation in the voltammograms despite the increase in scan rate. By contrast, increasing the scan rate causes deformation of the CV curves measured in NaCl (Figure 3.5b) and $TEMABF_4$/PC (Figure 3.6b), showing signs of ohmic drop and lower electrode capacitance.

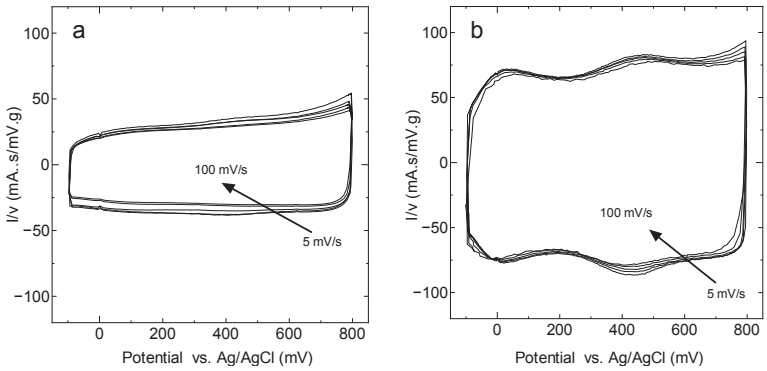

Figure 3.4: CV curves of (a) closed-end and (b) open-end SWCNTs in H_2SO_4, at scan rates of 5, 10, 20, 50, and 100 mV/s. The arrow indicates the direction of increasing the scan rate.

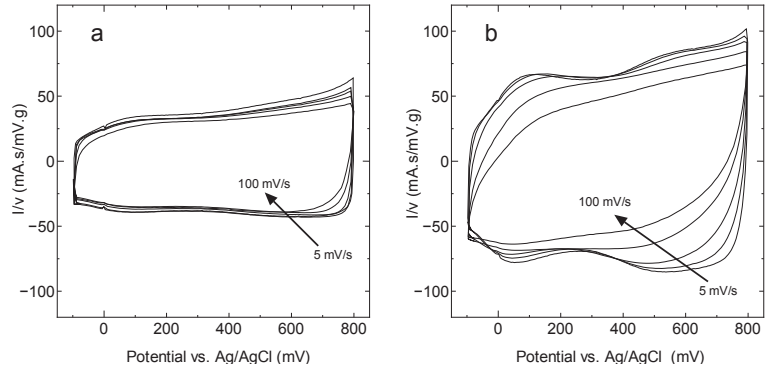

Figure 3.5: CV curves of (a) closed-end and (b) open-end SWCNTs in NaCl, at scan rates of 5, 10, 20, 50, and 100 mV/s. The arrow indicates the direction of increasing the scan rate.

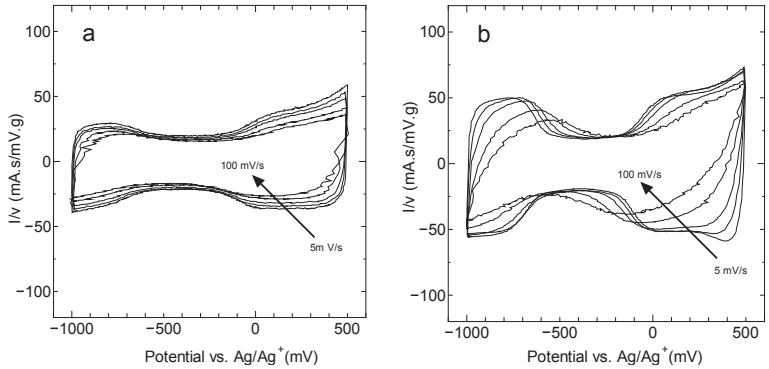

Figure 3.6: CV curves of (a) closed-end and (b) open-end SWCNTs in $TEMABF_4$/PC, at scan rates of 5, 10, 20, 50, and 100 mV/s. The arrow indicates the direction of increasing the scan rate.

Since the deformation was insignificant for closed-end tubes in NaCl and $TEMABF_4$/PC, the ohmic drop causing the deformation can be primarily attributed to the inner resistance to ion diffusion in the new porous structure introduced by decapping the tubes. Owing to the entanglement of SWCNTs in the bundle, ion storage in closed-end tubes possibly occurred on the outer surface of the bundle mat and in the inter-bundle spaces. This storage space is sufficiently large not to impose any constraints on ion adsorption, which resembles the behavior of a flat electrode, allowing ions to diffuse easily along the adsorption surface. Thus, the ohmic drop effect was not observed in closed-end tubes in the two electrolytes. In the open-end tubes, the additional ion storage space was the tubular channel inside the SWCNT, which provides a constrained diffusion path. The ion diffusion that requires sufficient time to proceed down the

tubular channel is likely to become dependent on the type of the ion. In the case of NaCl and $TEMABF_4$, the diffusion of ions is the result of ion migration. At high scan rates, the pores may not be able to follow the variation in potential as quickly as the outer surface of the bundle.[69] As a result, the time available is insufficient for the ions to diffuse all the way inside the tubes, and the scan is likely to be reversed before full-path penetration is attained. This shorter penetration depth reduces the electrolyte concentration and ionic conductivity and increases the internal resistance down the tubular pore, thus resulting in lower capacitance and a deformed voltammogram as the scan rate is increased on the voltammograms of both NaCl and $TEMABF_4$/PC.

With H_2SO_4, the fact that, at all scan rates investigated, the cyclic voltammograms of both closed-end and open-end do not exhibit any deformation, implies that the adsorption spaces outside and inside the tubes are both easily accessible. Such behavior might be expected, considering that H_2SO_4 dissociates in water to give protons H^+ with high ionic mobility. The proton mobility occurs as a result of two mechanisms: the hydrodynamic migration of hydronium ion (H_3O^+) and the ‘‘proton jump,’’ mechanism i.e., the transfer of an H^+ ion from one water molecule to the neighboring one, along a chain of water molecules. The combined effect of these two mechanisms leads to high mobility and high ionic conductivity.[70] On the other hand, the anion contribution to the observed behavior in Figure 3.4(b) cannot be easily judged. This is caused by the possibility of both HSO_4^- and $SO4^{-2}$ ions coexisting in the solution with a population that is crucially determined by the number of surrounding water molecules coordinating with the ions.[71] Nevertheless, the reported high conductivity of H_2SO_4 is significantly higher than that of NaCl (approximately 4 times higher) can be the origin behind the low ohmic drop shown in Figure 3.4(b).

To quantitatively assess the change in ohmic drop imposed by the nature of adsorption in the inner tubular structure of SWCNTs, an analytical approach is employed to reproduce the experimental results of the present study.[72] This approach explains the variation in the shape of the cyclic voltammogram relative to the time required for the ions to diffuse down the pore length at different scan rates. Ions generally require a longer time to travel down the path inside the porous structure of the space inside the tubes when compared with the outer surface of the tube that offers a shorter, straighter diffusion path.

The ion adsorption process is represented with the resistor–capacitor-in-series equivalent

circuit. The potential across the resistor is given by Ohm's law, ($E1 = IR$). Then the potential across the capacitor is defined as ($E2 = Q/C$). Both expressions are combined, and then differentiated with respect to time to obtain a time dependent expression for the potential across the equivalent circuit:

$$E(t) = RI(t) + \frac{Q(t)}{C} \tag{3.1}$$

In equation (3.1) above, R is the resistance, Q is the electric charge, and C is the double layer capacitance. The above equation is solved to obtain the current as a function of time:

$$I(t) = Cv\left\{1 - \left(1 - \frac{I_0}{Cv}\right)\exp\left(-\frac{t}{RC}\right)\right\} \tag{3.2}$$

where I_0 and I are electric current values at time values 0 and t, respectively. Then, the time is rephrased as (E/ν), where (ν) is the potential scan rate. The following is the final equation that predicts the current through the EDLC:

$$I(E) = Cv\left\{1 - \left(1 - \frac{I_0}{Cv}\right)\exp\left(-\frac{E - E_0}{vRC}\right)\right\} \tag{3.3}$$

Using equation (3.3), plots of mathematically are calculated CV curves under the same applied potential and scan rates used in the experiments. Using a trial and error procedure, the values of both the constants C and R were varied until the values that lead to the closest possible accordance between the experimentally measured and the mathematically calculated data were reached (Figure 3.7 for an example of open-end sample in NaCl). The value of R obtained from this trial and error procedure was considered to be the electrode resistance.

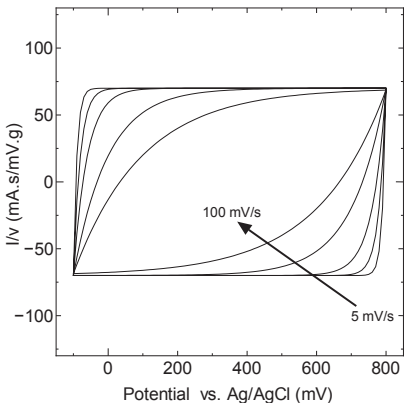

Figure 3.7: Example for Simulation of CV curve for open-end SWCNT in NaCl at scan rates of 5, 10, 20, 50, and 100 mV/s. The arrow indicates the direction of increasing the scan rate.

The process was performed for each of the different electrode/electrolyte combinations, as shown in Table 3.1. The results reflect the difference relative to the electrode resistance and its dependence on the type of electrolyte. For H_2SO_4, both closed- and open-end SWCNTs have the same resistance values. On the other hand, the electrode resistance of open-end tubes is three and 1.5 times that of closed-end tubes in NaCl and $TEMABF_4$, respectively.

Table 3.1 Total ohmic resistance for both types of SWCNTs

Sample	H_2SO_4	NaCl	$TEMABF_4$/PC
Closed-end SWCNT	0.005	0.01	0.037
Open-end SWCNT	0.005	0.028	0.055

3.4. Conclusion

Ion adsorption on the inner surface of SWCNTs requires higher energy than that on the outer surface within the range of parameters tested in this chapter. The constrained size makes this inner surface more sensitive to the nature and size of electrolyte ions. The increase in the number of charge carriers upon doping apparently provides the driving force required to push the ions inside open-end SWCNTs, leading to sudden increase in the electrode capacitance and resulting in the step-like step on the dumbbell voltammogram of SWCNTs.

CHAPTER 4

CHAPTER 4

Spectroscopic Evidence for the Origin of the Dumbbell Cyclic Voltammogram of Single-walled Carbon Nanotubes.

4.1. Overview

The unique electronic density of states (DOS) of single-walled carbon nanotubes (SWCNTs) is of significant relevance to both their optical and charge storage properties. The one-dimensional confinement of electrons results in a discontinuity known as a van Hove singularity (VHS) on the electronic density of states of SWCNTs. The energy required to excite an electron from one VHS in the valence band to a symmetrical one in the conduction band produces a spectroscopic signature that correlates to the tube chirality.[39] It follows that due to this quantization of electronic structure, the energy required to introduce a charge carrier into the valence or conduction band on the electronic density of states of SWCNTs also becomes a defined feature of the tube chirality. Using a combination of charge transfer processes and spectroscopic techniques, valuable information on the mechanism of charge storage in SWCNT electrodes can be obtained.[73-81]

In a sample of wide size distribution and low crystallinity, charge is stored as a collective response of all the tubes (as well as surface defects and chemical groups) in the sample, whereas the behavior of only a limited portion of the tubes is probed by spectroscopic methods such as Raman spectroscopy.[82] However, recent advancements in SWCNT science/applications now allow/require the synthesis and characterization of tubes with limited or specified chirality and diameter distribution.[83-85] In particular, for charge storage in electric double layer capacitors (EDLCs), recent studies revealed the importance of narrow-range or uni-modal pore size distributions in the maximization of the energy density of the porous electrode.[86] When SWCNTs with narrow diameter distribution are used as such electrode materials, the unique electronic structure of SWCNTs will be an important design factor that can be used to tune the potential window of the SWCNT electrode to optimize its charge storage. In addition, spectroscopic techniques will provide more information on the mechanism of charge transfer in

this new generation of SWCNTs that are well-defined in size and electronic properties.

Chapter 2 revealed that the cyclic voltammogram of SWCNT samples of high crystallinity and narrow diameter distribution had the shape of a dumbbell rather than either the typical rectangular shape obtained for other porous materials, or the butterfly shape previously reported for SWCNTs.[66] The dumbbell voltammogram was also observed in different aqueous electrolytes, and had a region of applied potential corresponding to the lowest capacitance, referred to as the "dumbbell grip." The width of that region, or the "grip distance," was shown to change as a function of the mean diameter of SWCNTs in the sample, confirming the intrinsic nature of the change in capacitance with applied potential. In chapter 3, it was revealed that the height of the step increase of SWCNT capacitance is related to the tube surface structure, where the cyclic voltammogram open-end SWCNTs showed higher electrode capacitance at the steps of the dumbbell.[87]

In this chapter, the evolution of the Raman spectra of SWCNTs as an EDLC electrode is followed within the potential range of the dumbbell voltammogram, to identify the origin of the change in charge carrier density giving rise to the aforementioned increase in capacitance. In addition, the same tests were performed on closed-end and open-end SWCNT samples to investigate the influence of surface structure, and again an array of different electrolytes was utilized to incorporate the potential effect of those additional elements on the spectro-electrochemical behavior of SWCNT electrodes.

4.2. Experimental

The sample used in the present study was sample referred to in previous chapters, produced by the arc discharge method (Meijo Nano Carbon Co. Ltd.), and has high crystallinity and narrow diameter distribution (Figure 3.1). The samples used after the as-grown samples were purified to remove amorphous carbon then purified and catalyst impurities, annealed at 1200 °C for 14 hours in vacuum,[53], then decapped as described in previous chapter to obtain two types of samples: closed-end and open-end SWCNTs. The *in situ* Raman measurements were performed in the potentiostatic mode using a potentiostat/galvanostat (Hokuto Denko) in a three electrode arrangement cell equipped with a quartz window directly above the working electrode (Figure 4.1). SWCNT sample and an activated carbon fiber sample on a platinum mesh current collector were used as the working and counter electrodes, respectively. Samples were sandwiched with

the current collector between two glass fiber sheets, with a small hole on one of them to allow access for the laser beam. Raman spectra were excited with two nitrogen-cooled excitation sources: green Nd:YAG laser (λ = 532, E_L = 2.33 eV), and red helium-neon laser (λ = 632.8, E_L = 1.96 eV), collected using a NRS 3300 (JASCO) spectrometer. The laser was focused on the working electrode and the spectra were collected for each applied potential at 0.1 V intervals. The spectra were fitted using Fityk software for further analyses.

Cyclic voltammetry (CV) was also conducted with a scan rate (5 mV/s). This scan rate is slow enough to allow sufficient time for ion diffusion into the porous structure inside the tubes, and permit to observe the characteristic dumbbell-shaped voltammogram that would not be observed otherwise, because of the deformation in the voltammogram at high scan rates due to ohmic drop in the porous structure as discussed in chapter 3.[87] All spectro-electro measurements were conducted for both closed- and open-end samples in different electrolytes (NaCl, NaBr, NaI, and KCl), each 1.0 M in concentration with Ag/AgCl as the reference electrode. The electrolytes used show a gradual change in the ion size which might shed light on individual differences between different ions.

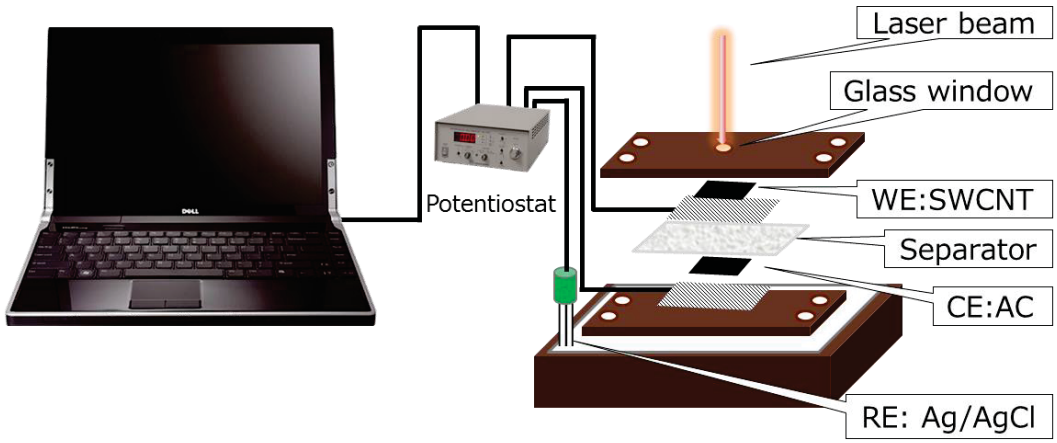

Figure 4.1: Cell arrangements for *in situ* Raman spectroscopy measurements.

4.3. Results and discussion

As shown in chapter 2, the cyclic voltammogram of SWCNTs having high crystallinity and narrow diameter distribution was recently observed in organic electrolytes, and shown to exhibit

the shape of a dumbbell. Upon performing cyclic voltammetry for separate samples of metallic and semiconducting SWCNTs, the cyclic voltammogram of semiconducting tubes had the shape of a dumbbell, while that of metallic tubes maintained a semi-rectangular shape in the same potential range. Moreover, the dumbbell voltammogram had a region of minimum capacity, referred to as the "dumbbell grip," whose width corresponded very closely to the energy band gap of the electronic density of states of the semiconducting tubes in the sample investigated. The dumbbell voltammogram was also observed using aqueous electrolytes. Based on these observations, the step-like increase in capacitance leading to the dumbbell shape was concluded to relate to the increase in charge carrier density that correlates with the electronic density of states of semiconducting tubes.

The goal of this chapter is to obtain spectroscopic evidence for the origin of the change in electrode capacitance leading to the appearance of the dumbbell-shaped voltammogram. Taking into consideration the aforementioned observations using cyclic voltammetry, it was expected to see considerable spectroscopic changes in the spectra of semiconducting SWCNTs.

Figure 4.2 shows the cyclic voltammogram of open-end SWCNTs (solid line) in NaCl, and also reveals the shape of a dumbbell. The center of the dumbbell grip is positioned at a potential value of about -0.31 V. Two step-like humps are observed roughly around -0.6 and 0 V, which will be referred to here as the "step potentials."

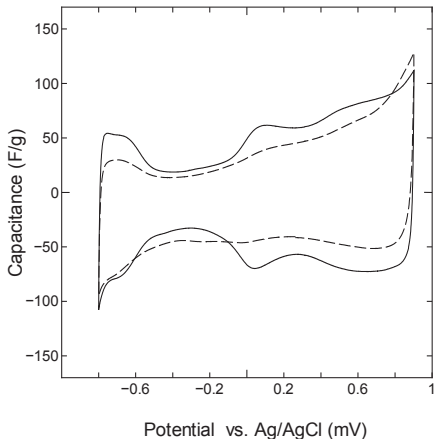

Figure 4.2: Cyclic voltammograms of closed-end (dashed line) and open-end (solid line).

The *in situ* Raman spectra of open-end SWCNTs in NaCl using two laser types (green, λ = 532 and red, λ = 632.8 nm) are shown in Figure 4.3 and Figure 4.4, which display the

potential-dependent spectral changes of semiconducting and metallic SWCNTs, respectively. The G band appears at a frequency shift around 1590 cm^{-1} in both figures.

Contrary to the results previously observed with cyclic voltammetry for semiconducting and metallic SWCNTs, the Raman spectra of semiconducting SWCNTs do not show any significant changes in the vibrational modes with applied potential. Raman spectra of metallic SWCNTs, on the other hand, exhibit significant potential-dependent changes in the shape and frequency of different characteristic peaks as discussed in more detail below.

The lower component of the tangential G band (called the G^- band), exhibits a conspicuous enhancement in intensity with applied potential. Similar results were observed with other electrolytes as seen in Figures A1 – A4 using 632.8 nm laser, and A5 –A8 using 532 nm laser.

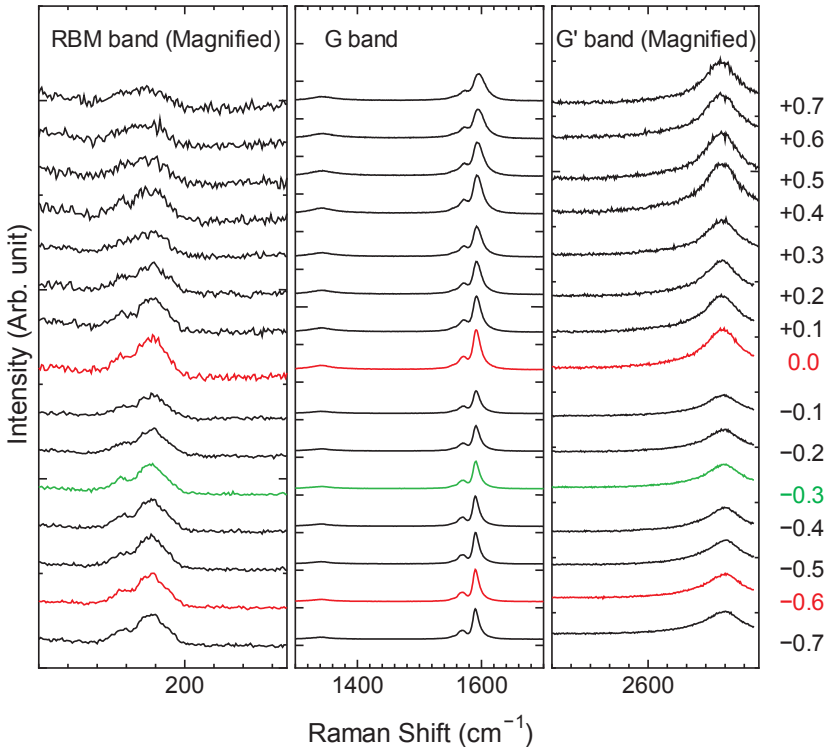

Figure 4.3: Raman spectra of the RBM mode (left), tangential mode (middle), and G' band (right), for open-end SWCNTs in NaCl using green laser. Values of applied potential in (V) are indicated on the right.

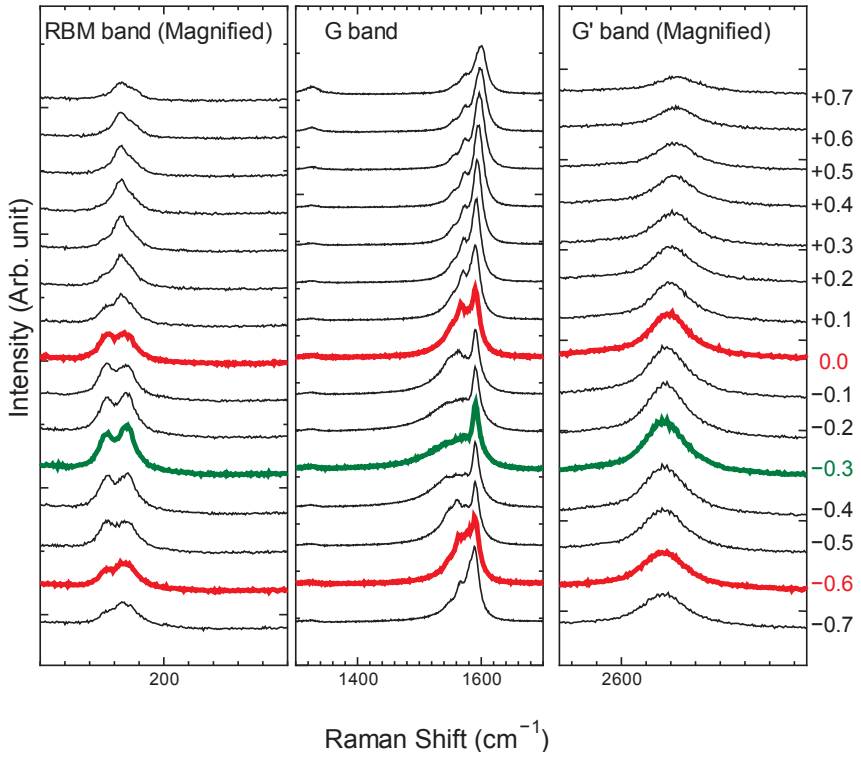

Figure 4.4: Raman spectra of the RBM mode (left), tangential mode (middle), and G' band (right), for open-end SWCNTs in NaCl using red laser. Values of applied potential in (V) are indicated on the right.

Contrary to other characteristic peaks in the spectra of SWCNTs, which can normally be fitted by a Lorentzian function that is symmetrical in shape, the G^- band of metallic SWCNTs is normally fitted by the asymmetrical Breit–Wigner–Fano (BWF) line shape. This feature appears only when the carrier density at the Fermi energy has a finite value;[56] hence it is considered an intrinsic and characteristic feature that can be used to distinguish the spectra of metallic SWCNTs from those of semiconducting ones. The intensity of the BWF feature, however, is of a collective nature, in the sense that it is enhanced in bundles of metallic SWCNTs compared to its value in the spectrum of individual tubes.[88] It is also known to change as a function of charge carrier density, and is enhanced upon charge transfer.[56, 89] This enhancement occurs not only with metallic SWCNTs, but was also observed in alkaline-metal doped (GIC's) due to the transfer of electrons from alkaline metals to the graphite layers for the low stage forms.[90]

Quite interestingly, the onset of intensity enhancement of the BWF feature seems to occur at values of applied potential that correspond closely to those of the "step potentials" on the dumbbell voltammogram in Figure 4.2. This was unexpected, considering that the step

potentials are supposed to correlate with the energy transition between the first singularities on the density of states of semiconducting but not metallic SWCNTs. This observation leads us to presume that the charge generated due to doping of semiconducting tubes is possibly being transferred to metallic ones, thereby enhancing the BWF feature in the spectra of Figure 4.4, due to some form of inter-tube free carrier transfer tendency from semiconducting tubes towards metallic tubes and semiconducting tubes with smaller energy gaps.[91] However, in the absence of an exact mechanism to explain this hypothesis, it remains unverified without at least further examination of other charge transfer-dependent Raman modes besides the BWF feature. For this purpose, other features that are known to be sensitive to charge transfer were examined: the position of the higher frequency component of the tangential G mode (G^+ band), the intensity of the radial breathing mode (RBM band), and the frequency shift of the G' band.

First, the frequency shift of the G^+ band was examined as shown in Figure 4.5. The frequency of the G^+ band is expected to show an upshift due to doping, which is explained by the stiffening of the C–C bond associated with electron removal from the π-band of the electronic structure of SWCNTs.[89, 92, 93] Figure 4.5 shows the frequency shift of the G^+ band for semiconducting and metallic SWCNTs, probed by green and red laser respectively. It can clearly be seen that the frequency upshift is higher for metallic tubes in the potential region where the charge carrier density of only semiconducting tubes is being altered.

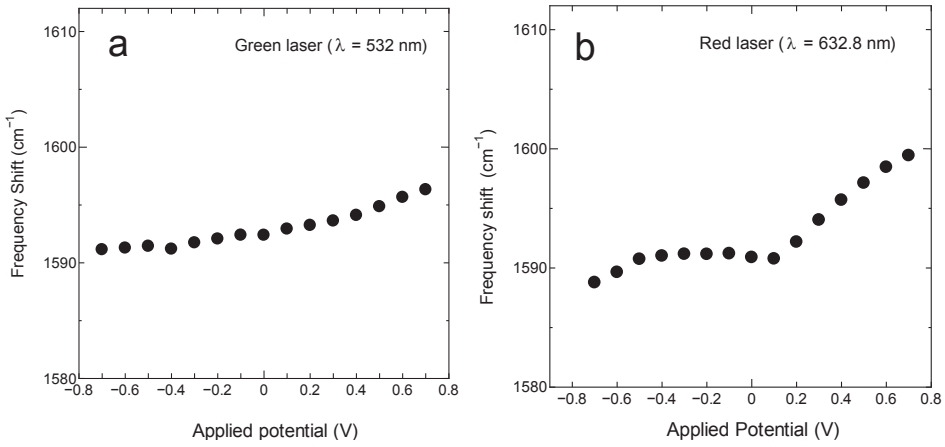

Figure 4.5: Frequency shift of G^+ band with applied potential in different electrolytes for open-end SWCNTs using (a) green laser and (b) red laser.

Next, the change in intensity was examined for the radial breathing mode (RBM), which is a

low energy mode that is sensitive to the charge density on the tubes. As shown in Figures 4.3 and 4.4, two RBM peaks can be seen with each laser type. For comparison purposes, each peak was fitted with a Lorentzian function, and plotted the change in peak intensity relative to that of the G band with applied potential (Figures 4.6 and 4.7). The peaks denoted as P1 and P2 are peaks probed using the red laser, and P3 and P4 are for those probed with the green laser. Upon comparing the two figures, it can be seen that P1 and P2 in Figure 4.6 exhibit a sharp drop in intensity, while little or no change in the intensity is seen with P3 and P4 in Figure 4.7. Another observation is that the trend in intensity loss for P1 is quite different from P2 despite the fact that both peaks are probed using the same laser source. P1 has a point of maximum intensity, and then loses intensity gradually and progressively on both sides of the applied potential. The intensity of P2 maintains a plateau of constant value, after which it starts to lose intensity rather sharply. Further, the plateau of constant intensity of P2 matches the potential interval of the voltammogram dumbbell grip in Figure 4.2. Following previous analyses on the evolution of the RBM band with applied potential, P1 can be attributed to metallic SWCNTs, while P2 is designated as semiconducting.[94] This assumption can be rationalized since it is possible to probe both metallic and semiconducting SWCNTs using red laser, whose energy is close to both E_{11}^{M} and E_{33}^{S} on the density of states of SWCNTs in our samples.[59, 93]

The intensity drop with applied potential for the tubes probed in Figure 4.6 but not in Figure 4.7 has two possible explanations. One reason is based on the hypothesis that doping charges can decrease the electron-photon interaction, thus reducing the Raman intensity.[94] One might speculate that these doping-induced changes cause more significant changes to the electron-photon interaction at E_{11}^{M} (probed with red laser), which is lower in energy than E_{33}^{S} (probed with green laser). The other possible reason is the aforementioned possibility of charge transfer from semiconducting tubes probed with a green laser, which has an approximate band gap of 0.51 eV, towards tubes probed with a red laser that consist of metallic tubes and semiconducting tubes with an approximate band gap of 0.49.[59]

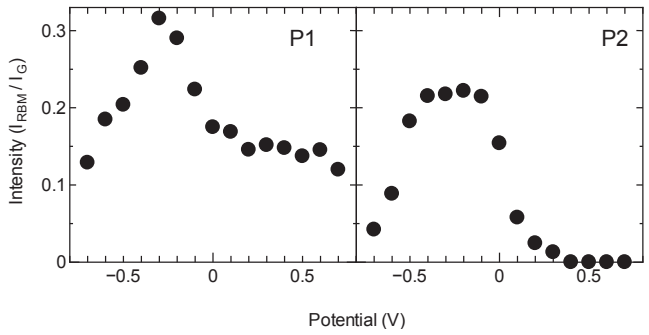

Figure 4.6: RBM intensity for peaks probed for open-end SWCNTs in NaCl using red (λ = 632.8 nm) laser.

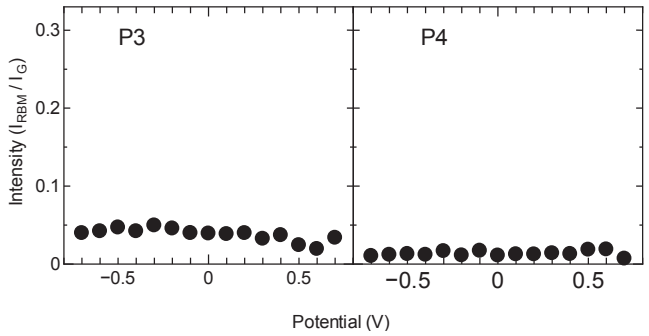

Figure 4.7. RBM intensity for peaks probed for open-end SWCNTs in NaCl using green (λ= 532 nm) laser.

Nevertheless, due to the multiple possibilities behind the drop in RBM intensity, the assumption of inter-tube charge transfer as the origin of change of both RBM intensity and G^+ band remains inconclusive. Thus, the frequency shift of the G' band was analyzed, and compared with previous studies that reported particular sensitivity in G' band position to charge transfer, by exhibiting upshifts in the region of anodic potential and downshifts in the cathodic potential region.[89] In Figure 4.8, it can be seen the potential-dependent change in frequency shift of the G' band, probed employing the two laser sources as before. It can be seen that the G' band of metallic tubes (632.8 nm laser) shows a region of constant frequency shift, followed by significant upshifts. In contrast, the frequency shift of G' of semiconducting tubes (532 nm laser) does not exhibit any frequency upshift with applied potential. In fact, its frequency shows a slight downshift in the anodic region. The reason behind the slight difference for semiconducting tubes in terms of direction of shift remains unexplainable, but it is clear that (i)

unlike metallic tubes, semiconducting tubes do not show the previously predicted upshift in the anodic region, and (ii) similar to the above mentioned enhancement in the BWF feature, the onset of upshift in the G' band frequency of metallic tubes corresponds closely to the band gap of semiconducting tubes. It is therefore assumed that the charge generated on semiconducting tubes due to doping is adopted by the metallic tubes, thereby triggering the aforementioned observations in their Raman features. In other words, the above analysis suggests that when semiconducting tubes are doped, the electrons removed from the valance band transfer to the metallic tubes, enhancing the BWF feature. This leads to more ion adsorption on the surface once they travel through the outer circuit and causes more frequency upshift in the G' band.

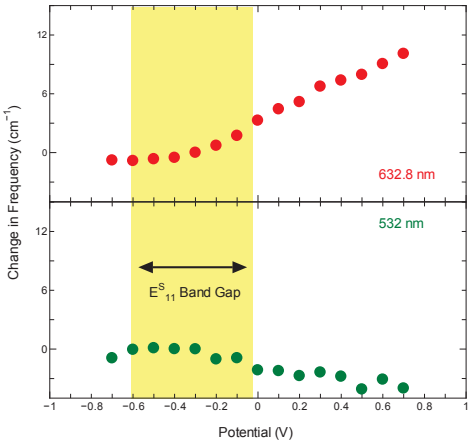

Figure 4.8: G' band for open-end SWCNTs in NaCl using red (λ = 632.8 nm) and green (λ = 532 nm) lasers.

Due to the major role of adsorbed ions in the process of electrochemical doping as indicated from the analysis above, the influence of surface structure was next incorporated, by comparing the results obtained for open-end tubes with those obtained for closed-end tubes. It is interesting that all the aforementioned changes in Raman spectra are observed more clearly in open-end SWCNT samples. With closed-end samples, the enhancement in the BWF feature is separated by a larger interval of potential (Figure 4.9 and Figures A9 to A16). The cyclic voltammogram of closed-end SWCNTs (dashed line in Figure 4.2) is also less defined and does not correlate accurately with the electronic band gap of semiconducting tubes, and the capacitance calculated from integrating the CV curve (44.9 F/g) is lower than that with the open-end SWCNT sample (55.9 F/g). It can also be seen that the frequency upshift of the G^+ band for closed-end SWCNTs (Figure 4.10) is much less than that shown in Figure 4.5 for open-end SWCNTs. Despite the fact

that both samples include the same chiralities of metallic and semiconducting tubes, the upshift of the G^+ band for open-end SWCNTs during the anodic potential reaches a maximum of 12.8 cm^{-1}. The closed-end SWCNTs sample, on the other hand, shows little upshift (around 4 cm^{-1}). With the G' band, open-end tubes exhibit a maximum frequency upshift of 10 cm^{-1} while closed-end tubes show almost no frequency upshift (Figure 4.11).

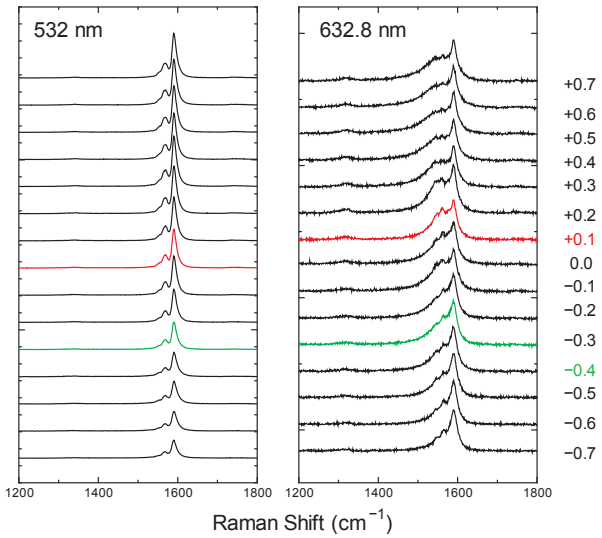

Figure 4.9: Raman spectra of the tangential G band for closed-end SWCNTs in NaCl using two laser types. Values of applied potential in (V) are indicated on the right.

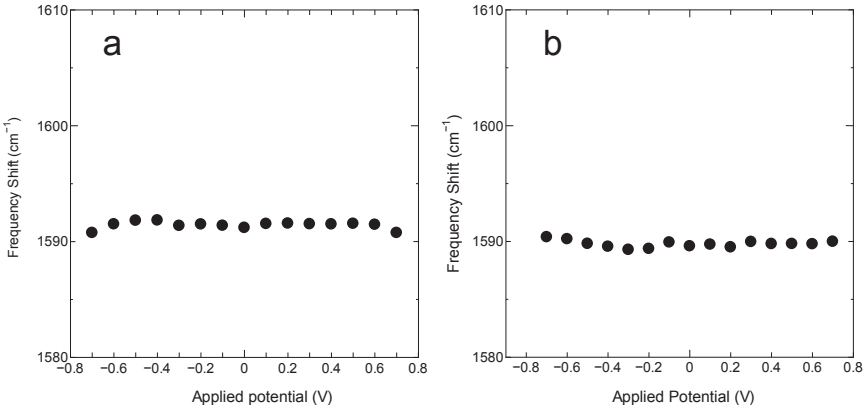

Figure4.10: Frequency shift of G^+ band of closed-end SWCNTs with applied potential in NaCl probed with (a) green (λ= 532 nm) and (b) red (λ= 632.8 nm) laser.

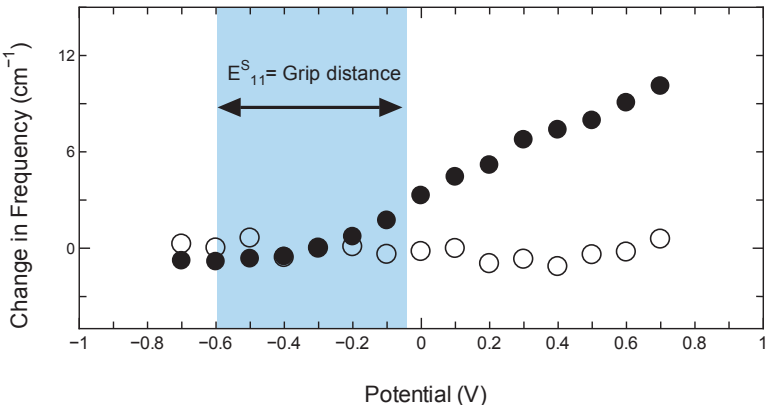

Figure 4.11: Frequency shift of G' band for open-end (solid circles) and closed-end (hallow circles) SWCNTs in NaCl probed using red laser (λ= 632.8 nm).

These differences invoke the surface structure as an important factor where electrochemical doping is concerned, and suggest that electrochemical doping and the resulting magnitude of shift are bound by the availability of surface area for ion adsorption. Since charge storage in EDLC is achieved by adsorption of ions on the electrode surface, the availability of the surface area for adsorption of ions will determine the magnitude of charge transferred. The BET surface area of open-end SWCNTs samples is much higher than that for closed-end ones (as seen from Figure 3.2) due to the additional surface area of the cylindrical cavity inside the tubes, and the usability of this additional space for ion storage can be inferred from the higher electrode capacitance obtained with open-end SWCTs. This indicates that exact knowledge of the surface area exposed for ion adsorption is essential to correlate the doping level of SWCNTs, which also hinders the comparison of the present results to previous work in which information about the surface structure of the tubes was not accurately specified.

Furthermore, and to avoid confusion about the origin of the observed changes in spectroscopic features, the *in situ* spectroscopic changes were observed for an as-grown SWCNT sample that did go through any purification or annealing treatment. The frequency shift of G^+ band is plotted with applied potential in Figure 4.12. The as grown sample shows slightly higher frequency upshifts, especially at high applied potentials. This difference might be simply due to experimental error, or might probably be associated with some additional charge transfer due to metallic nanoparticles, and/or any chemical groups and defects that might exist on the surface on the as grown sample.

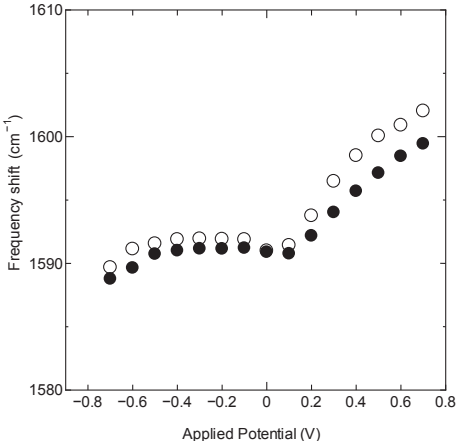

Figure 4.12: Frequency shift of G^+ band with applied potential in different electrolytes for open-end (solid circles) and As-grown (hollow circles) SWCNTs using red laser.

Finally, and within the range of electrolytes tested in the present study, no conspicuous changes in the magnitude of frequency upshift were observed by changing the type of adsorbed ion (Figure 4.13). One exception is seen with NaI where the upshift for the anodic doping (anion adsorption) side starts to surpass the other electrolytes. This occurs for both closed-end and open-end SWCNT samples at potential value around +0.3 V, which corresponds to the redox potential of iodine, suggesting an additional mechanism behind the change in the frequency upshift in the case of NaI.[95]

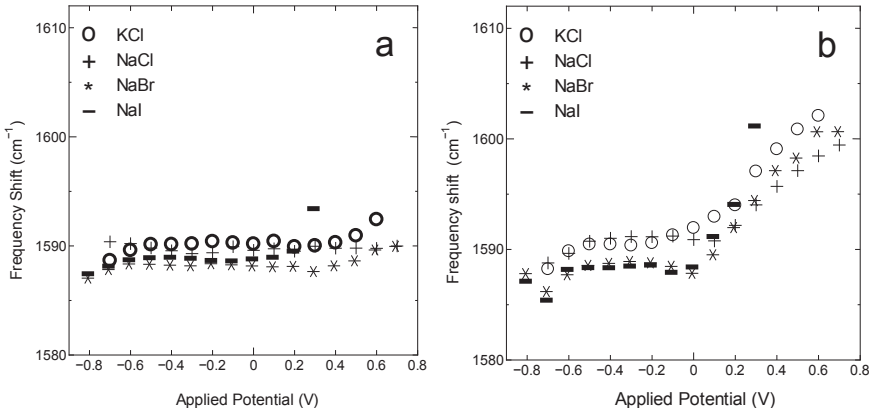

Figure 4.13: Frequency shift of G^+ band with applied potential in different electrolytes for (a) closed-end and (b) open-end SWCNTs, probed with red laser (λ = 632.8 nm).

4.4. Conclusion

This chapter revealed that the sharp, step-like increase in SWCNT electrode capacitance is associated with an enhancement in the charge carrier density in SWCNTs. The additional charge occurs as a result of doping of semiconducting tubes, which seems to be transferred to metallic tubes, leading to an enhancement in the BWF feature in the Raman spectra at certain potential values. This results in an increase in charge carrier density hence enhances ion adsorption, all of which correlate with the electronic band gap of semiconducting tubes. Similarly, the intensity of the RBM band of metallic tubes decreases and the positions of the G^+ and G' bands upshift with applied potential. In contrast, those of semiconducting tubes do not seem to be significantly disturbed by the increase in charge carrier density. The surface area of the tubes remains an important factor, as seen from the higher ion adsorption-related frequency upshift for G^+ and G' bands. This shows that optimizing the SWCNTs surface area is essential to fully utilize the advantages obtained from the enhancement of charge carrier density in this class of SWCNTs highly-defined in diameter distribution and electronic structure.

CHAPTER 5

CHAPTER 5

Nitrogen Doping and Electrode Capacitance of Doped Single-walled Carbon Nanotubes

5.1. Overview

As discussed in chapter 1, Van der Waals forces between SWCNTs cause them to aggregate and form bundles. As a result, the interstitial space between the tubes may not be useable for ion storage. In addition, it was shown in chapter 3 that while the space inside SWCNTs can be used to store ions and increase the usable electrode specific surface area, it is also likely to increase the electrode resistance, leading to performance deterioration at high rates.

One approach to address the above considerations is to create defects on the surface of the tube, to offer additional windows for ion adsorption, an approach that was shown to result in specific surface area to a value comparable to that of theoretical maximum of a graphene sheet.[49] However, this method may also result in proportionally higher electrode resistance and lead to the formation of surface chemical groups that may catalyze electrolyte decomposition and reduce the stable potential window, and also cause capacitor aging.[96]

An alternative approach is to manipulate the electronic structure of SWCNTs by doping with foreign species. This approach can be realized by several methods. Doping by intercalation was demonstrated in the form of nanotube bundles intercalated with atoms or ions,[97] and doping by encapsulation is also reported by incorporation of fullerenes inside open-end SWCNTs to prepare peapods.[98, 99] Another form of doping is possible by foreign elements substitution, and involves the incorporation of foreign elements within the graphitic network of the tube. Doping SWCNTs using this approach is increasingly being reported to enhance their capacitance and electronic conductivity hence their charge storage performance as electrodes for diverse energy devices.

Among the methods investigated, nitrogen doping to several kinds of carbon materials has been performed in order to improve their physicochemical properties as fuel-cell, lithium-ion battery electrodes (LIB), and other energy devices. [100-111] For fuel-cell application, it has been well known that the nitrogen doped carbon materials can work as efficient metal-free catalyst

for oxygen reduction reaction (ORR). These unique ORR catalytic properties can be utilized for air-electrode of metal-air cells which have much higher specific energy densities than LIB has.[112] N-doped carbon materials are also charming materials for LIBs, since it is well recognized that the presence of N atoms in the carbon materials can enhance the electric conductivity and hence the Li ion storage capacity.[109, 110]

A variety of carbon materials have been used for the N-doping host and several doping methods have been tested. The methods can be divided to two groups by the timing of N-doping. Nitrogen atoms can be incorporated in the carbon framework while the framework is being constructed; this method is denoted as on-synthesis doping.[109, 113, 114] On the other hand, nitrogen atoms can replace the carbon position of some kinds of carbon materials and/or they can be added to the edge part of carbon materials: post-synthesis doping.[102, 104, 106, 115] Although post-synthesis doping has some advantages such as easy control of doping level compared to on-synthesis doping, it has only been applied to limited kinds of carbon materials, and only to relatively low crystalline carbon materials which have chemically active sites.

For well crystalized carbon materials such as diamond and SWCNTs, it has been believed that the post-synthesis doping should not be effective.

Recently, and using graphite oxide as starting material, Parvez *et al*.[102] succeeded in preparing N-doped graphene by a post synthesis method using cyanamide as nitrogen source. In this chapter, doping nitrogen into SWCNTs is attempted by this post-synthesis method. With the obtained SWCNT samples, the N-doping effect on the properties of SWCNT EDLC electrodes was investigated

5.2. Experimental

5.2.1. Preparation of samples

Three kinds of SWCNTs were used: one CVD produced SWCNT sample (CoMoCAT: Sigma Aldrich), and two arc-discharge produced SWCNT samples (FHP and SO: Meijo Nano Carbon). Hereinafter, the three kinds of SWCNT samples will be denoted as CoMoCAT, FHP, and SO.

First, the SWCNT samples were purified to remove the metal nanoparticle catalysts by appropriate acid treatments. Then, samples were acid treated to introduce defects on their walls in the following manner:

The type of treatment varied depending on the level of crystallinity of each sample. While CoMoCAT sample has small mean diameter and already contained a significant level of defects, FHP and SO samples, on the other hand were produced by arc discharge method and had high level of crystallinity, hence more aggressive approaches were necessary as explained below:

1. CoMoCAT: To avoid destruction of the sample, HCl purification treatment was deemed sufficient and no further treatment was performed.
2. FHP: The purified sample was sonicated for 3hr in a mixture of H_2SO_4 and HNO_3 with a volume ratio of 3:1 under ice bath, then vacuum-filtered and washed by deionized water.
3. SO: Electrochemical oxidation was performed. The sample is assembled in a capacitor-like arrangement, and the Pt mesh is used as counter electrode. 5 M HCl was used as electrolyte. A voltage of 2.0 V was applied for 30 min in a current range of 1.0A. After that, the sample is vacuum-filtered and washed with deionized water.

Nitrogen doping treatments were performed according to the method developed by Parvez *et al*.[102] Sodium dodecyl sulfate was added to SWCNT dispersed water (1 mg/ml), and sonicated for 30 min to form a homogeneous dispersion. Then, cyanamide solution (50wt % in water) was added dropwise while stirring. The mixture was then stirred continuously and heated at 100 °C to remove water. The resulting solid was annealed under argon atmosphere as follows.

The sample was heated to 550 °C at a rate of 2 °C /min. After the temperature has been maintained at 550 °C for 4h, it was further heated to 800 °C at a rate of 2 °C /min and kept at this temperature for another 1h. After that, the sample was cooled to room temperature at a rate of 2.5 °C /min.

The doped nitrogen contents were evaluated by X-ray photoelectron spectroscopy (XPS) measurements using ULVAC PHI 5000. The structural changes of the SWCNT samples by the N-doping treatments were investigated by SEM (JSM-7001FF (JEOL)), Raman (JASCO NRS 3300) and N_2 adsorption/desorption measurements (Shimadzu Gemini 2375).

5.2.2. Electrochemical measurement

Cyclic voltammetry measurements were performed using a three-electrode cell where glass fiber-sandwiched sample of SWCNTs was used as the working electrode, and activated carbon fiber was used as the counter electrode. The measurements were conducted under ambient temperature in aqueous NaCl and organic $TEMABF_4$/PC as electrolytes using Ag/AgCl and

Ag/Ag^+ reference electrodes respectively. Charge/discharge measurements with constant current (charge-discharge measurements) were also performed in the potential range of -700 – 700 mV in NaCl, and -1400 – 800mVin $TEMABF_4$, at constant current rate of 100 mA/g.

5.3. Results and discussion

The difference in crystallinity between the three (CoMoCAT, FHP, SO) SWCNT samples can be seen in their Raman spectra from the relative intensity of the D band (seen around 1330 cm^{-1} (Figure 5.1) compared to that of G band (at around 1590 cm^{-1}). Especially, in the case of SO, apparently D-band peak could not be seen in the spectrum. The peaks observed in low frequency region are the radial breathing modes (RBMs) whose peak positions are inversely proportional to the tube diameters.[56]

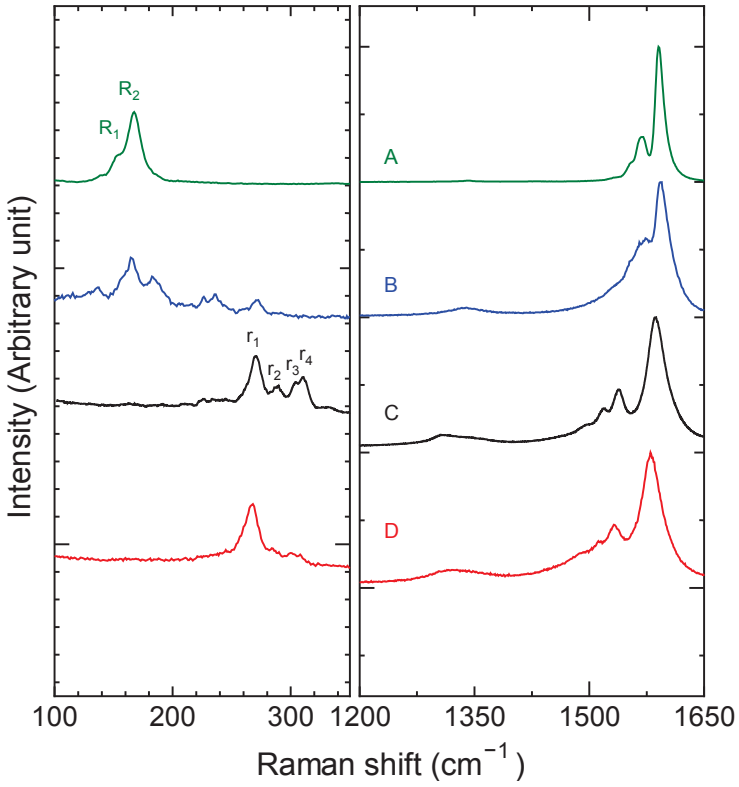

Figure 5.1: Raman spectra for (A) SO (B) FHP (C) CoMoCAT, and (D) NCoMoCAT SWCNT samples, excited using Nd:YAG laser ($\lambda = 532$, $E_L = 2.33$ eV).

Judging from the RBM peak pattern, it can be understood that SO and CoMoCAT have a small diameter distribution while FHP consists of wide range diameter tubes. The tube diameters can be evaluated for SO and CoMoCAT using $d_t = 234/(\omega_{RBM} - 10)$[56] (nm) and the calculated values are R_1(1.6 nm), R_2(1.45 nm), r_1(0.9 nm), r_2(0.84 nm), r_3(0.8 nm), r_4(0.78 nm). Figure 5.2 shows the N1s XPS spectra of SO, FHP and CoMoCAT samples after the N-doping treatments.

As shown in the figure, no peaks could be observed for SO and FHP samples. On the other hand, in the case of CoMoCAT, N1s XPS peaks could be clearly seen. This N-doping treated CoMoCAT sample will denoted as NCoMoCAT. The nitrogen content of NCoMoCAT is evaluated to be 1.8% by the integrated XPS peak intensities. The N1s XPS spectrum of NCoMoCAT is constructed from two peaks. By the curve fitting procedure, the peak positions are determined to be 398.4 and 400.4 eV. The former and latter peaks are assigned as pyridinic (P-N) and graphitic (G-N) nitrogen atoms, respectively.

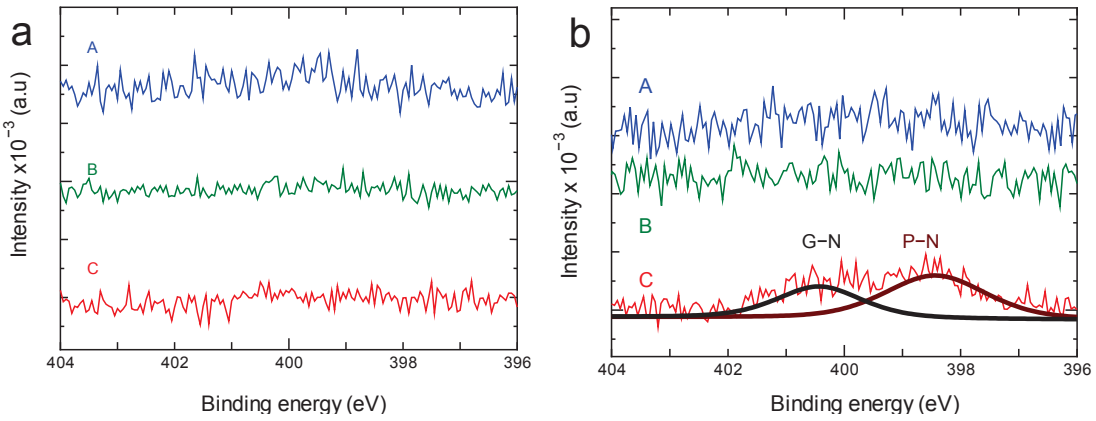

Figure 5.2: XPS N1s spectra for (a) pristine and (b) N-doped samples (A) FHP (B) SO, and (C) CoMoCAT.

Cyclic voltammogram (CV) and charge/discharge (C/D) measurements were performed for CoMoCAT and NCoMoCAT EDLC electrodes. Both measurement data showed that the EDLC capacity of NCoMoCAT (evaluated from C/D data with current density of 100 mA/g) is significantly larger than that of CoMoCAT (83.4 F/g and 48 F/g in NaCl for CoMoCAT and NCoMoCAT, respectively). CV diagrams taken at scan rate 100 mV/s in NaCl and $TEMABF_4$ are shown in Figure 5.3 and Figure 5.4 respectively. It can be seen in Figure 5.3 that in NaCl the capacitance per unit surface area for NCoMoCAT sample is higher than that for CoMoCAT.

Also, the CV shape of NCoMoCAT is closer to the dumbbell shape than that of CoMoCAT, which resembles a spindle and shows greater deformation. On the other hand, CV shapes of both pristine and N-doped samples in $TEMABF_4$/PC (Figure 5.4) show deformed voltammograms.

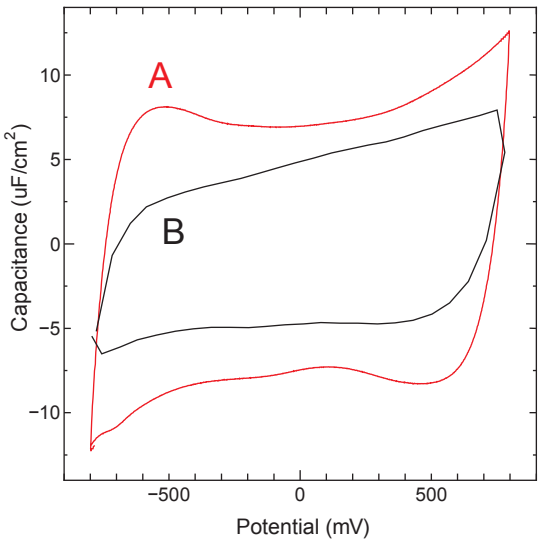

Figure 5.3: Cyclic voltammetry results of (A) NCoMoCAT and (B) CoMoCAT samples in 1.0 M aqueous NaCl at scan rate 100 mV/s.

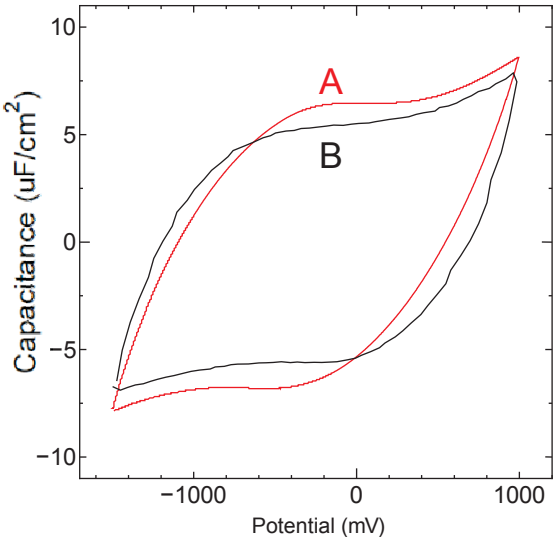

Figure 5.4: Cyclic voltammetry results of (A) NCoMoCAT and (B) CoMoCAT samples in $TEMABF_4$/PC

electrolyte at scan rate 100 mV/s.

As discussed in the chapter 3, such difference in CV shape is due to the difference in resistance factor for ion adsorption (eq. 3.3).

$$I(E) = Cv\left\{1 - \left(1 - \frac{I_0}{Cv}\right)\exp\left(-\frac{E - E_0}{vRC}\right)\right\} \tag{3.3}$$

It means that the resistance factor of CoMoCAT is significantly larger than that of NCoMoCAT. Therefore, it is plausible that the electric conductivity of NCoMoCAT is increased by the N-doping treatment. This explanation is also supported by Figure 5.5 in which, in NaCl the capacitance of CoMoCAT shows a sharper decline with increasing the scan rate than that of NCoMoCAT (Figure 5.5a). In TEMABF$_4$/PC, on the other hand Figure 5.5b shows that the decline in capacitance with scan rate of NCoMoCAT does not show improvement from that of CoMoCAT.

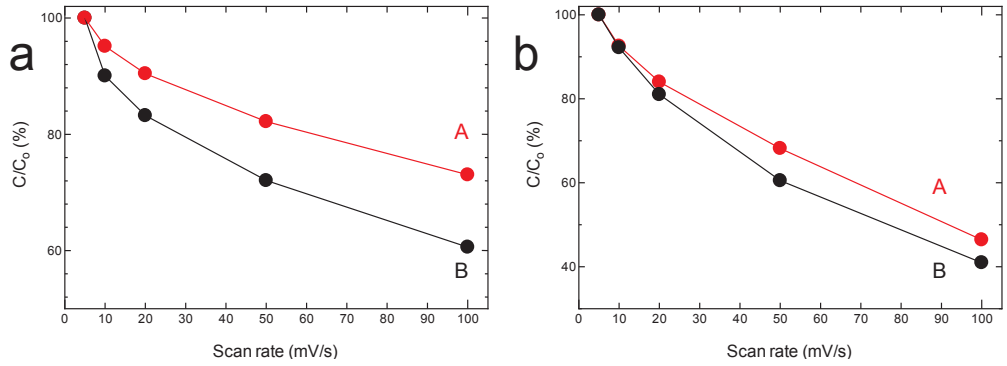

Figure 5.5: Capacitance change with scan rate for (A) NCoMoCAT and (B) CoMoCAT samples, taken in (a) NaCl and (b) TEMABF4/PC. (C/Co) is calculated as percentage from the capacitance at scan rate 5 mV/s.

One may suspect that some kinds of structural defects may occur by N-doping treatment which leads to the increase of specific surface area and EDLC capacity. However, this possibility can be dismissed by the following two experimental results. As shown in Figure 5.1, the G/D peak intensity ratio of NCoMoCAT is almost the same as that of CoMoCAT. It indicates no significant structural defects occurred by the N-doping. Furthermore, the specific surface area of NCoMoCAT derived from N_2 adsorption measurement is 489.9 m^2/g, which is rather smaller than that of CoMoCAT (540.7 m^2/g) as seen from Figure 5.6. This indicates that the

increase in capacitance is not related to the specific surface area, and that a kinematical reason lies behind the higher resistance of CoMoCAT sample for ion adsorption. This reason originates from the decrease in resistance upon N-doping, due to the enhancement of the electric conductivity by the N-doping.[116]

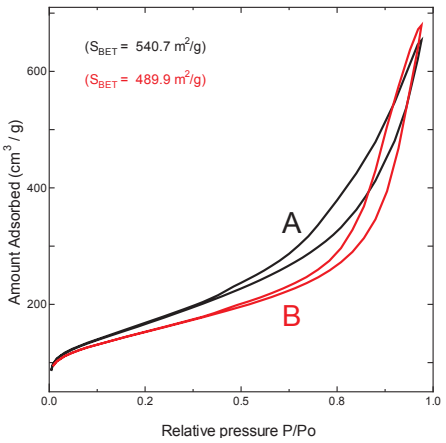

Figure 5.6: Nitrogen adsorption isotherms for (A) CoMoCAT and (B) NCoMoCAT SWCNT samples.

It is therefore reasonable that N atoms should be incorporated somewhere in SWCNTs. On the other hand, as indicated earlier, doping of N atoms was no possible into SO and FHP SWCNTs which have higher crystallinity than CoMoCAT does. Furthermore, graphitic N 1s XPS peak was observed for NCoMoCAT sample. Judging from these experimental data and from the energetical point of view, substitutional N-doping into perfect graphene sheet may not occur. Instead of that, N atoms are incorporated to CoMoCAT SWCNTs from some defective sites. CoMoCAT SWCNTs are produced by CVD method at relatively low temperature. Therefore, some defect sites should exist on the surface of CoMoCAT SWCNTs. From observing the change in the RBM peak pattern of CoMoCAT by N-doping, it can be seen that before N-doping, r_1~r_4 peaks are clearly observed. However, the peak intensity of higher wavenumber RBM peaks decrease after N-doping. As explained already, higher wavenumber corresponds to smaller SWCNT diameters. It indicates that smaller tubes having higher chemical activity tended to react with N atoms.

Finally the cyclability of the NCoMoCAT EDLC electrode is addressed. Figure 5.7 shows the EDLC capacitance determined from charge/discharge curves as a function of cycle number. CoMoCAT sample show constant capacity for 200 cycles. On the other hand, NCoMoCAT

sample shows increasing trend of capacity with cycle number although somehow the data are fluctuated. This increase is not observed with pristine CoMoCAT sample, so it is plausible to assume that this increase is associated with the existence of nitrogen in the graphitic network. Thorough investigation is necessary to determine the exact mechanism behind the increase in capacitance with cycling.

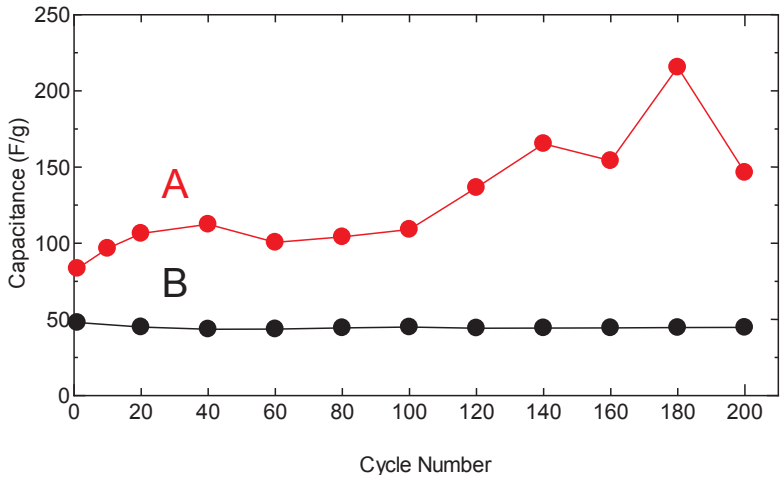

Figure5.7: Capacitance versus cycle number for (A) NCoMoCAT and (B) CoMoCAT samples cycled between -700 mV and +700 mV in 1.0 M NaCl electrolyte at current density 100mA/g.

By contrast, cyclability test of NCoMoCAT using organic $TEMABF_4$/PC electrolyte (Figure 5.8), does not show the unusual capacity increase for this experiment. It is also found that unlike the case with NaCl, the EDLC capacity of NCoMoCAT (45 F/g) for this organic electrolyte is only slightly enhanced compared to that of CoMoCAT (35 F/g), which is expected considering that the effective ion sizes of this organic electrolyte including the solvated molecules are too big to enter inside the small diameter SWCNTs.

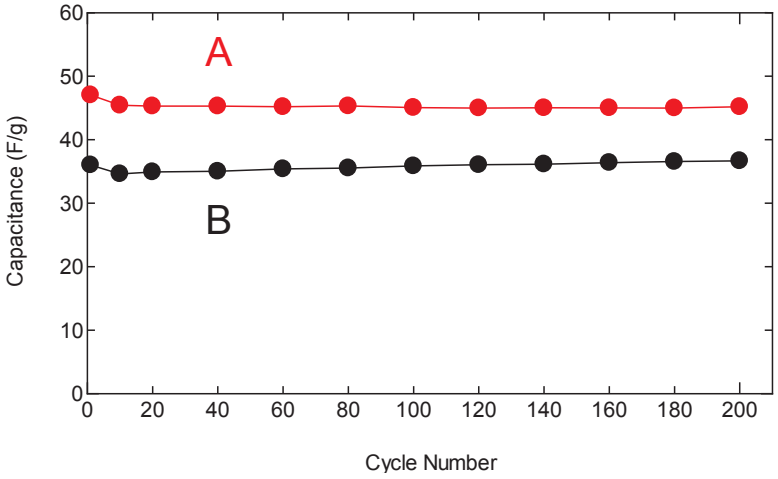

Figure5.8: Capacitance versus cycle number for (A) NCoMoCAT and (B) CoMoCAT samples cycled between -1400 mV and +800 mV in 1.0 M TEMABF$_4$ electrolyte at current density 100mA/g.

5.4. Conclusion

This chapter demonstrated the process of doping SWCNTs with nitrogen, and the resulting changes in their electrochemical behaviour and electrode capacitance. The incorporation of nitrogen atom was not possible into SO and FHP SWCNTs which had higher crystallinity. On the other hand, N atoms were successfully incorporated into CoMoCAT SWCNTs that had lower crystallinity and higher level of defects, as was shown from XPS spectra of the three samples. It is concluded that substitutional N-doping into perfect graphene sheet may not occur. The doped samples had enhanced capacitance at high scan rate. In addition, charge discharge measurements showed unusual increase with cycling, which is not observed in pristine samples. This suggests that the increase is associated with the presence of nitrogen atoms in the graphitic network of doped SWCNTs sites. Thorough investigation is required to elucidate the mechanism of capacitance enhancement with cycling in NaCl, and its absence in organic electrolyte.

CHAPTER 6

CHAPTER 6

Conclusions and Perspective

6.1. Conclusions

Single-walled carbon nanotubes SWCNTs are fascinating nano-scale aromatic macromolecule with superior conductivity, controllable morphology, and characteristic one-dimensional electronic structure. The successful exploitation in electronic, mechanical, and energy storage applications is bound by the realizing of these promising characteristics. With the advancement in science, we are now able to synthesize or isolate high quality and limited/specific diameter and chirality SWCNTs that will approach hypothetically anticipated properties, which in turn requires us to revisit their performance in diverse fields, and accurately characterize this new class of one dimensional allotrope of carbon.

This study investigated the electrochemical performance of SWCNTs as electrode material for electrochemical capacitors. The samples used in this study had high crystallinity and narrow diameter distribution. In terms of surface structure, the samples were processed into two types: closed-end and open-end SWCNTs. Diverse characterization techniques, electrochemical measurements, and electrolyte media were employed to map the electrochemical behavior of the samples in relation to their fundamental properties, surface morphology, and performance environment. The study came to the following conclusions:

1. From Chapter 2, it was concluded that, unlike other carbon material, SWCNTs have a unique electrochemical behavior, directly influenced by their electronic density of states. This was demonstrated through the cyclic voltammogram of SWCNT that displayed a distinct dumbbell shape rather than the conventionally expected butterfly shape. This shape resulted from the DOS of semiconducting tubes in the SWCNT sample. The dumbbell voltammogram is composed of a region of minimum capacitance, referred to as the “dumbbell grip”, and two step-like humps on both sides of the potential of zero charge, and result from a sudden increase in the electrode capacitance. The dumbbell grip was shown to represent a characteristic signature of the tubs’ electronic structure, and correlate with SWCNT chirality and diameter irrespective of the electrolyte used. The increase in capacitance leading to the two dumbbell steps is the result of the increase in charge carrier density that occurs once the applied potential reaches the energy value that corresponds to the first van Hove singularity on the density of states of semiconducting SWCNTs in the

sample. These changes were shown be intrinsic and dependent on the tubes' chirality and mean diameter, and independent of the electrolyte. This distinct behavior can be observed only in SWCNT with a narrow diameter distribution that represent more accurately the actual electrochemical behavior of SWCNTs.

2. From Chapter 3, we showed that, while the dumbbell voltammogram reflects intrinsic properties of SWCNTs, the amount of obtained electrode capacitance and the "height of the dumbbell steps" is bound by the available surface area for ion adsorption. Using closed-end and open-end SWCNT sample as EDLC electrodes verified that the space inside SWCNTs can be used to store ions, because open-end SWCNT sample had higher specific area, and higher electrode capacitance than closed-end sample. In addition, no changes were seen in the level of defects upon decapping SWCNTs, which rules out the possibility of relating the higher capacitance to pseudo-type capacitance that normally originates from chemical groups attached to the tube surface. In addition to the possibility of ion adsorption inside the tubes, the nature of ion adsorption on the outer and inner surfaces of single-walled carbon nanotubes (SWCNTs) in different aqueous and organic electrolytes was also addressed, and the difference between the nature of adsorption on the inner and outer surface of the tube is investigated, by preforming CV electrochemical measurements at different scan rates, on closed-end and open-end SWCNTs, and in different aqueous and organic electrolytes. The outer surface of the tubes demonstrated the behavior of a flat electrode with less dependence on the potential scan rate when compared to the inner surface that acts as a porous electrode showing an ohmic drop and a distorted voltammogram at high scan rates. We showed that the electrochemical behavior of the outer surface of the tubes resembles that of a flat electrode with less dependence on the potential scan rate when compared to the inner surface that which acts as a porous electrode showing an ohmic drop and a distorted voltammogram at high scan rates. Mathematical analysis showed that opening the inner channel of the tubes increases electrode resistance, and that the magnitude of variation in the resistance depends on the type of electrolyte.

3. In Chapter 4, we combined electrochemical measurements with Raman spectroscopy to investigate the origin of the dumbbell-shaped voltammogram, by *in situ* monitoring spectroscopic changes with applied potential, and correlating them with changes in charge carrier density leading to the dumbbell-like cyclic voltammogram of SWCNTs used as EDLC electrodes. We performed these spectro-electorchemical measurements using two laser excitation sources to probe metallic and semiconducting SWCNTs in the sample, and using closed-end and open-end SWCNT samples to elucidate the joined influence of both electronic and surface structure on the changes in charge carrier and capacitance. Our study

revealed unexpected sharp spectroscopic changes on Breit–Wigner–Fano (BWF) feature of metallic SWCNTs that coincided with the two step-like jumps in the dumbbell voltammogram that correlates with the electronic band gap of semiconducting SWCNTs, and suggested possible charge transfer from semiconducting to metallic tubes upon doping. In addition, we observed that the spectra of open-end SWCNT samples exhibited more defined changes that correlated more accurately with the electronic structure of the tubes compared to those observed with closed-end SWCNTs. These observations support both findings obtained in Chapter 2 and Chapter 3, in the sense that the capacitance of SWCNTs depends on a characteristic level of charge carrier that correlates with their fundamental properties, while the surface area of the tubes remains an important factor that decide the total amount of adopted charge hence electrode capacitance. It becomes essential to optimize the SWCNTs surface area to fully utilize the advantages obtained from the enhancement of charge carrier density of SWCNTs.

4. Finally, in Chapter 5 we demonstrated the possibility of increasing the electrode capacitance of SWCNTs, by introducing nitrogen atoms into their graphitic network. We showed that, depending on the electrolyte employed, nitrogen-doped SWCNTs can exhibit an enhancement in their capacitance, and we also showed unusual increase in the capacitance with continued cycling, which is not observed in pristine SWCNTs sample. The increase is thought to be related to the presence of nitrogen atoms in the graphitic network.

6.2. Perspective

There remain other possible factors to further address in the future. The surface area of SWCNTs remains far from being completely utilized for ion storage, and the usability for the interstitial spaces between the tubes is yet to be addressed and optimized.

In terms of utilizing the characteristic electronic properties of SWCNTs, there is still room for further development, which can be achieved if mono-chirality SWCNTs can be realized through separation techniques.

In addition, the ohmic drop and deformation in the cyclic voltammogram with increasing scan rate must be addressed theoretically and experimentally in relation to SWCNTs mean diameter and extract a general relation of between relevant parameters, towards a systematic selection process of SWCNTs as EDLC electrode materials.

Finally, the electrolyte-dependence of the capacitance obtained from nitrogen-doped SWCNTs must also be investigated, and the exact mechanism of capacitance increase with charge-discharge cycles must be elucidated.

REFERENCES

REFERENCES:

1. Conway, B. E. *Electrochemical Supercapacitors: Scientific Fundamentals and Technological Applications*; Springer Science+Business Media: New York, 1999.
2. Chmiola, J.; Yushin, G.; Gogotsi, Y.; Portet, C.; Simon, P.; Taberna, P. L.; Anomalous Increase in Carbon Capacitance at Pore Sizes Less Than 1 Nanometer. *Science* 2006, *313*, 1760- 1763.
3. Kötz, R.; Carlen, M. Principles and applications of electrochemical capacitors. *Electrochim. Acta* 2000, *45*, 2483- 2498.
4. L. Eliad, G. Salitra, I. Soffer and D. Aurbach, *J. Phys. Chem. B* 2001, 105, 6880- 6887.
5. Chmiola, J.; Yushin, G.; Dash, R. K.; Hoffman, E. N.; Fischer, J. E.; Barsoum, M. W.; Gogotsi, Y. Double-Layer Capacitance of Carbide Derived Carbons in Sulfuric Acid. *Electrochem. Solid-State Lett.* 2005, 8(7), A357- A360.
6. Eikerling, M.; Kornyshev, A. A.: Lust, E. Optimized Structure of Nanoporous Carbon-Based Double-Layer Capacitors. *J. Electrochem. Soc.* 2005, 152(1), E24- E33.
7. Simon, P.; Gogotsi, Y. Materials for electrochemical capacitors. *Nat. Mater.* 2008, 7, 845−854.
8. Portet, C.; Yushin, G.; Gogotsi, Y. Effect of Carbon Particle Size on Electrochemical Performance of EDLC. *J. Electrochem. Soc.* 2008, 155, 7, A531- A536.
9. Chmiola, J.; Largeot, C.; Taberna, P. L.; Simon, P. Gogotsi, Y. Desolvation of Ions in Subnanometer Pores and Its Effect on Capacitance and Double-Layer Theory. *Angew. Chem., Int. Ed.*, 2008, 47, 3392- 3395.
10. Lin, R.; Taberna, P. L.; Chmiola, J.; Guay, D.; Gogotsi, Y.; Simon, P. Microelectrode Study of Pore Size, Ion Size, and Solvent Effects on the Charge/Discharge Behavior of Microporous

Carbons for Electrical Double-Layer Capacitors. *J. Electrochem. Soc.* 2009, 156(1), A7- A12.

11. Kajdos, A.; Kvit, A.; Jagillo, J.; Yushin, G. Tailoring the Pore Alignment for Rapid Ion Transport in Microporous Carbons. *J. Am. Chem. Soc.* 2010, 132(10), 3252- 3253.
12. Bard, A. J.; Faulkner, L. R. *Electrochemical Methods: Fundamentals and Applications*, 2nd ed.; John Wiley & Sons, Inc., 2001.
13. Srinivasan S. *Fuel Cells: From Fundamentals to Applications*, Springer Science+Business Media, LLC, 2006.
14. Tipler, P. A. *Physics*; Worth Publishers, Incorporated, 1976.
15. Chmiola, J.; Yushin, G.; Dash, R.; Gogotsi, Y. Effect of pore size and surface area of carbide derived carbons on specific capacitance *J. Power Sources* 2006, *158*, 1, 765–772.
16. Shi, H. Activated carbons and double layer capacitance. *Electrochim. Acta*. 1996, 41, 10, 1633-1639.
17. Qu, D. Studies of the activated carbons used in double-layer supercapacitors. *J. Power Sources* 2002, 109, 2, 403-411.
18. Kim, Y.J.; Horie, Y.; Ozaki, S.; Matsuzawa, Y.; Suezaki, H.; Kim, C.; Miyashita, N.; Endo, M. Correlation between the pore and solvated ion size on capacitance uptake of PVDC-based carbons. *Carbon* 2004, 42, 8–9, 1491–1500.
19. Salitra, G.; Soffer, A.;Eliad, L.; Cohen, Y.; Aurbach, D. Carbon Electrodes for Double‐Layer Capacitors I. Relations Between Ion and Pore Dimensions. *J. Electrochem. Soc.* 2000, *147*, 7, 2486-2493.
20. Vix-Guterl, .; Frackowiak, E.; Jurewicz, K.; Friebe, M.; Parmentier, J.; Béguin, B. Electrochemical energy storage in ordered porous carbon materials. *Carbon* 2005, *43*, 6, 1293–1302.
21. Eliad, L.; Salitra, G.; Soffer, A.; Aurbach, D. On the Mechanism of Selective

Electroadsorption of Protons in the Pores of Carbon Molecular Sieves. *Langmuir* 2005, 21,7, 3198–3202.

22. Eliad, L.; Pllak, E.; Levy, N.; Salitra, G.; Soffer, A.; Aurbach, D. Assessing optimal pore-to-ion size relations in the design of porous poly(vinylidene chloride) carbons for EDL capacitors. *Appl. Phys. A: Mater. Sci. Process.* 2006, *82*, 4, 607-613.
23. Arulepp, M.; Leis, J.; Lätt, M. ; Miller F.; Rumma, K.; Lust, E.; Burke, A.F. The advanced carbide-derived carbon based supercapacitor. *J. Power Sources* 2006, 162, 2, pp. 1460–1466.
24. Arulepp, M.; Permann, L.; Leis, J.; Perkson, A.; Rumma, K.; Jänes, A.; Lust, E. Influence of the solvent properties on the characteristics of a double layer capacitor. *J. Power Sources* 2004, 133, 320–328.
25. Raymundo-Piñero, E.; Kierzek, K.; Machnikowski, J.; Béguin, F. Relationship between the nanoporous texture of activated carbons and their capacitance properties in different electrolytes. *Carbon* 2006, 44, 12, Pages 2498–2507.
26. Jänes, A.; Permann, L.; Arulepp, M; Lust, E. Electrochemical characteristics of nanoporouscarbide-derived carbon materials in non-aqueous electrolyte solutions. *Electrochem. Commun.* 2004, *6*, 3, 313–318.
27. Shanina, B.D.; Konchits, A.A.; Kolesnik, S.P.; Veynger, A.I.; Danishevskii, A.M.; Popov, V.V.; Gordeev, S.K.; Grechinskaya, A.V. A study of nanoporous carbon obtained from ZC powders (Z=Si, Ti, and B) *Carbon* 2003, *41*, 15, 3027–3036.
28. Huang, J.; Sumpter, B. G.; Meunier, V. Theoretical Model for Nanoporous Carbon Supercapacitors. *Angew. Chem., Int. Ed.*, 2008, *47*, 3, 520- 524.
29. Huang, J.; Sumpter, B. G.; Meunier, V. A Universal Model for Nanoporous Carbon Supercapacitors Applicable to Diverse Pore Regimes, Carbon Materials, and Electrolytes. *Chem.--Eur. J.* 2008, *14*, 22, 6614–6626.

30. Largeot, C.; Portet, C.; Chmiola, J.; Taberna, P.; Gogotsi Y.; Simon, P. *J. Am. Chem. Soc.* 2008, *130*, 2730- 2731.

31. Lu, G. Q.; Zhao, X. S.; Nanoporous Materials – An overview. In *Nanoporous Materials: Science and Engineering*; Lu, G. Q.; Zhao, X. S, Eds.; World Scientific, Singapore, 2004; pp. 1-13.

32. François Béguin; Elzbieta Frackowiak Nanotextured Carbons for Electrochemical Energy Storage. In *Nanomaterials Handbook*; CRC Press, 2006.

33. Takashi Kyotani; John Chmiola; Yury Gogotsi Carbide-Derived Carbons and Templated Carbons. In *Carbons for Electrochemical Energy Storage and Conversion Systems; Advanced Materials and Technologies*; CRC Press, 2009; pp. 77–113.

34. Futaba, D. N.; Hata, K.; Yamada, T.; Hiraoka, T.; Hayamizu, Y.; Kakudate, Y.; Tanaike, O.; Hatori, H.; Yumura, M.; Iijima, S. Shape-engineerable and Highly Densely Packed Single-walled Carbon Nanotubes and Their Application as Super-capacitor Electrodes. *Nat Mater.* 2006, *5*, 987–994.

35. Portet, C.; Chmiola, J.; Gogotsi, Y.; Park, S.; Lian, K. Electrochemical Characterizations of Carbon Nanomaterials by the Cavity Microelectrode Technique. *Electrochim. Acta* 2008, *53*, 7675 – 7680.

36. Yang, C.-M.; Kim, Y.-J.; Endo, M.; Kanoh, H.; Yudasaka, M.; Iijima, S.; Kaneko, K. Nanowindow-Regulated Specific Capacitance of Supercapacitor Electrodes of Single-Wall Carbon Nanohorns. *J. Am. Chem. Soc.* 2007, *129*, 20–21.

37. Zhang, Y.; Feng, H.; Wu, X.; Wang, L.; Zhang, A.; Xia, T.; Dong, H.; Li, X.; Zhang, L. Progress of Electrochemical Capacitor Electrode Materials: A Review. *Int. J. Hydrogen Energy* 2009, *34*, 4889 – 4899.

38. Wang, G.; Zhang, L.; Zhang, J. A Review of Electrode Materials for Electrochemical

Supercapacitors. *Chem. Soc. Rev.* 2012, *41*, 797–828.

39. Saito, R.; Dresselhaus, G.; Dresselhaus, M. S. *Physical Properties of Carbon Nanotubes*; World Scientific Publishing Co. Pte. Ltd. Singapore; 1998.
40. Jie Han Structures and Properties of Carbon Nanotubes. In *Carbon Nanotubes*; CRC Press, 2004; pp. 1–24.
41. Dresselhaus, M.; Avouris, P. Introduction to Carbon Materials Research. In *Carbon Nanotubes*; Dresselhaus, M.; Dresselhaus, G.; Avouris, P., Eds.; Topics in Applied Physics; Springer Berlin Heidelberg, 2001; Vol. 80, pp. 1–9.
42. Dresselhaus, M. S.; Dresselhaus, G.; Saito, R. Physics of Carbon Nanotubes. *Carbon* 1995, 33, 883 – 891.
43. Saito, R.; Dresselhaus, G.; Dresselhaus, M. S. Trigonal Warping Effect of Carbon Nanotubes. *Phys. Rev. B* 2000, 61, 2981–2990.
44. Shah, D.; Bruque, N.; Alam, K.; Lake, R.; Pandey, R. Electronic Properties of Carbon Nanotubes Calculated from Density Functional Theory and the Empirical Π-bond Model. *J. Comput. Electron.* 2007, *6*, 395–400.
45. Barone, V.; Peralta, J. E.; Wert, M.; Heyd, J.; Scuseria, G. E. Density Functional Theory Study of Optical Transitions in Semiconducting Single-Walled Carbon Nanotubes. *Nano Lett.* 2005, 5, 1621–1624.
46. Kimizuka, O.; Tanaike, O.; Yamashita, J.; Hiraoka, T.; Futa-ba, D. N.; Hata, K.; Machida, K.; Suematsu, S.; Tamamitsu, K.; Saeki, S.; Yamada, Y.; Hatori, H. *Carbon* 2008, 46, 1999−2001.
47. Yamada, Y.; Kimizuka, O.; Tanaike, O.; Machida, K.; Suematsu, S.; Tamamitsu, K.; Saeki, S.; Yamada, Y.; Hatori, H. *Electrochem. Solid- State Lett.* 2009, 12 (3), K14−K16.
48. Yamada, Y.; Kimizuka, O.; Machida, K.; Suematsu, S.; Tamamitsu, K.; Saeki, S.; Yamada, Y.; Yoshizawa, N.; Tanaike, O.; Yamashita, J.; Don, F.; Hata, K.; Hatori, H. *Energy Fuels* 2010,

24, 3373−3377.

49. Hiraoka, T.; Izadi-Najafabadi, A.; Yamada, T.; Futaba, D. N.; Yasuda, S.; Tanaike, O.; Hatori, H.; Yumura, M.; Iijima, S.; Hata, K. *Adv. Funct. Mater.* 2010, 20, 422−428.
50. Izadi-Najafabadi, A.; Yamada, T.; Futaba, D. N.; Hatori, H.; Iijima, S.; Hata, K. *Electrochem. Commun.* 2010, 12, 1678−1681.
51. Jang, I. Y.; Muramatsu, H.; Park, K. C.; Kim, Y. J.; Endo, M. *Electrochem. Commun.* 2009, 11, 719−723.
52. Yamada, Y.; Tanaka, T.; Machida, K.; Suematsu, S.; Tamamitsu, K.; Kataura, H.; Hatori, H. *Carbon* 2012, 50, 1422−1444.
53. Rinzler, A. G.; Liu, J.; Dai, H.; Nikolaev, P.; Huffman, C. B.; Rodríguez-Macías, F. J.; Boul, P. J.; Lu, A. H.; Heymann, D.; Colbert, D. T.; et al. Large-scale Purification of Single-wall Carbon Nanotubes: Process, Product, and Characterization. *Appl. Phys. A: Mater. Sci. Process.* 1998, 67, 29–37.
54. Seto, Y.; Nishio-Hamane, D.; Nagai, T.; Sata, N. *Rev. High Pressure Sci. Technol.* 2010, 20 (3), 269−276.
55. Thess, A.; Lee, R.; Nikolaev, P.; Dai, H.; Petit, P.; Robert, J.; Xu, C.; Lee, Y. H.; Kim, S. G.; Rinzler, A. G.; Colbert, D. T.; Scuseria, G. E.; Tomanek, D.; Fischer, J. E.; Smalley, R. E. *Science* 1996, 273, 483− 487.
56. Dresselhaus, M. S.; Dresselhaus, G.; Saito, R.; Jorio, A. Raman Spectroscopy of Carbon Nanotubes. *Phys. Rep.* 2005, 409, 47–99.
57. Melle-Franco, M.; Marcaccio, M.; Paolucci, D.; Paolucci, F.; Georgakilas, V.; Guldi, D. M.; Prato, M.; Zerbetto, F. *J. Am. Chem. Soc.* 2004, 126, 1646−1647.
58. Moonoosawmy, K. R.; Kruse, P. *J. Am. Chem. Soc.* 2008, 130, 13417−13424.
59. Dr. Shigeo MARUYAMA's Fullerene and Carbon Nanotube Site, University of Tokyo.

Kataura-Plot for Resonant Raman: 1D DOS (van Hove singularity); http://www.photon.t.u-tokyo.ac.jp/~maruyama/kataura/1D_DOS.html.

60. Hata, K.; Futaba, D. N.; Mizuno, K.; Namai, T.; Yumura, M.; Iijima, S. Water-Assisted Highly Efficient Synthesis of Impurity-Free Single-Walled Carbon Nanotubes. *Science* 2004, 306, 1362–1364.
61. Hiraoka, T.; Izadi-Najafabadi, A.; Yamada, T.; Futaba, D. N.; Yasuda, S.; Tanaike, O.; Hatori, H.; Yumura, M.; Iijima, S.; Hata, K. Compact and Light Supercapacitor Electrodes from a Surface-Only Solid by Opened Carbon Nanotubes with 2 200 M2 G−1 Surface Area. *Adv. Funct. Mater.* 2010, 20, 422–428.
62. Geng, H. Z.; Zhang, X. B.; Mao, S. H.; Kleinhammes, A.; Shimoda, H.; Wu, Y.; Zhou, O. Opening and Closing of Single-wall Carbon Nanotubes. *Chem. Phys. Lett.* 2004, 399, 109 – 113.
63. Pederson, M. R.; Broughton, J. Q. Nanocapillarity in Fullerene Tubules. *Phys. Rev. Lett.* 1992, 69, 2689–2692.
64. Urita, K.; Shiga, Y.; Fujimori, T.; Iiyama, T.; Hattori, Y.; Kanoh, H.; Ohba, T.; Tanaka, H.; Yudasaka, M.; Iijima, S.; et al. Confinement in Carbon Nanospace-Induced Production of KI Nanocrystals of High-Pressure Phase. *J. Am. Chem. Soc.* 2011, 133, 10344–10347.
65. Liu, Q. X.; Wang, C. X.; Li, S. W.; Zhang, J. X.; Yang, G. W. Nucleation Stability of Diamond Nanowires Inside Carbon Nanotubes: A Thermodynamic Approach. *Carbon* 2004, 42, 629 – 633.
66. Al-zubaidi Ayar; Inoue, T.; Matsushita, T.; Ishii, Y.; Hashimoto, T.; Kawasaki, S. Cyclic Voltammogram Profile of Single-Walled Carbon Nanotube Electric Double-Layer Capacitor Electrode Reveals Dumbbell Shape. *J. Phys. Chem. C* 2012, 116, 7681–7686.
67. Merlet, C.; Rotenberg, B.; Madden, P. A.; Taberna, P.-L.; Simon, P.; Gogotsi, Y.; Salanne, M.

On the Molecular Origin of Supercapacitance in Nanoporous Carbon Electrodes. *Nat Mater.* 2012, 11, 306–310.

68. Kondrat, S.; Georgi, N.; Fedorov, M. V.; Kornyshev, A. A. A Superionic State in Nano-porous Double-layer Capacitors: Insights from Monte Carlo Simulations. *Phys. Chem. Chem. Phys.* 2011, 13, 11359–11366.
69. Levie, R. de On Porous Electrodes in Electrolyte Solutions: I. Capacitance Effects. *Electrochim. Acta* 1963, 8, 751 – 780.
70. Erdey-Gruz, T. *Transport Phenomena in Aqueous Solutions*; Adam Hilger: Bristol, England, 1974, pp. 278–284.
71. Sugawara, S.; Yoshikawa, T.; Takayanagi, T.; Shiga, M.; Tachikawa, M. Quantum Proton Transfer in Hydrated Sulfuric Acid Clusters: A Perspective from Semiempirical Path Integral Simulations. *J. Phys. Chem. A* 2011, 115, 11486–11494.
72. 陽祐石井; 早紀山田; 知弘松下; Al-zubaidi Ayar; 晋司川崎 カーボンナノチューブ電極のハロゲンイオン吸着特性. 炭素 2011, 2011, 253–262.
73. Tarábek, J.; Kavan, L.; Dunsch, L.; Kalbac, M. Chemical States of Electrochemically Doped Single Wall Carbon Nanotubes As Probed by Raman Spectroelectrochemistry and Ex Situ X-ray Photoelectron Spectroscopy. *J. Phys. Chem. C* 2008, 112, 13856–13861.
74. Rafailov, P. M.; Stoll, M.; Maultzsch, J.; Thomsen, C. Raman Measurements on Electrochemically Doped Single-Walled Carbon Nanotubes. *AIP Conf. Proc.* 2003, 685, 135–138.
75. Stoll, M.; Rafailov, P. M.; Frenzel, W.; Thomsen, C. Electrochemical and Raman Measurements on Single-walled Carbon Nanotubes. *Chem. Phys. Lett.* 2003, 375, 625 – 631.
76. Rafailov, P. M.; Thomsen, C.; Dettlaff-Weglikowska, U.; Roth, S. High Levels of Electrochemical Doping of Carbon Nanotubes: Evidence for a Transition from Double-Layer

Charging to Intercalation and Functionalization. *J. Phys. Chem. B* 2008, 112, 5368–5373.

77. Kalbac, M.; Kavan, L.; Dunsch, L.; Dresselhaus, M. S. Development of the Tangential Mode in the Raman Spectra of SWCNT Bundles During Electrochemical Charging. *Nano Lett.* 2008, 8, 1257–1264.
78. Rafailov, P. M.; Maultzsch, J.; Thomsen, C.; Kataura, H. Electrochemical Switching of the Peierls-like Transition in Metallic Single-walled Carbon Nanotubes. *Phys. Rev. B* 2005, 72, 045411.
79. Kalbac, M.; Kavan, L.; Dunsch, L. Changes in the Electronic States of Single-Walled Carbon Nanotubes as Followed by a Raman Spectroelectrochemical Analysis of the Radial Breathing Mode. *J. Phys. Chem. C* 2008, 112, 16759–16763.
80. Claye, A.; Rahman, S.; Fischer, J. E.; Sirenko, A.; Sumanasekera, G. U.; Eklund, P. C. In Situ Raman Scattering Studies of Alkali-doped Single Wall Carbon Nanotubes. *Chem. Phys. Lett.* 2001, 333, 16 – 22.
81. Kavan, L.; Rapta, P.; Dunsch, L.; Bronikowski, M. J.; Willis, P.; Smalley, R. E. Electrochemical Tuning of Electronic Structure of Single-Walled Carbon Nanotubes: In-situ Raman and Vis-NIR Study. *J. Phys. Chem. B* 2001, 105, 10764–10771.
82. Ruch, P. W.; Hardwick, L. J.; Hahn, M.; Foelske, A.; Kötz, R.; Wokaun, A. Electrochemical Doping of Single-walled Carbon Nanotubes in Double Layer Capacitors Studied by in Situ Raman Spectroscopy. *Carbon* 2009, 47, 38 – 52.
83. Tulevski, G. S.; Franklin, A. D.; Afzali, A. High Purity Isolation and Quantification of Semiconducting Carbon Nanotubes via Column Chromatography. *ACS Nano* 2013, 7, 2971–2976.
84. Flavel, B. S.; Kappes, M. M.; Krupke, R.; Hennrich, F. Separation of Single-Walled Carbon Nanotubes by 1-Dodecanol-Mediated Size-Exclusion Chromatography. *ACS Nano* 2013, 7,

3557–3564.

85. He, M.; Jiang, H.; Liu, B.; Fedotov, P.; Chernov, A.; Obraztsova, E.; Cavalca, F.; Wagner, J.; Hansen, T.; Anoshkin, I.; et al. Chiral-selective Growth of Single-walled Carbon Nanotubes on Lattice-mismatched Epitaxial Cobalt Nanoparticles. *Sci. Rep.* 2013, 3, 1460.
86. Kondrat, S.; Perez, C. R.; Presser, V.; Gogotsi, Y.; Kornyshev, A. A. Effect of Pore Size and Its Dispersity on the Energy Storage in Nanoporous Supercapacitors. *Energy Environ. Sci.* 2012, 5, 6474–6479.
87. Al-zubaidi A.; Inoue, T.; Matsushita, T.; Ishii, Y.; Kawasaki, S. Ion Adsorption on the Inner Surface of Single-walled Carbon Nanotubes Used as Electrodes for Electric Double-layer Capacitors. *Phys. Chem. Chem. Phys.* 2012, 14, 16055–16061.
88. Kempa, K. Gapless Plasmons in Carbon Nanotubes and Their Interactions with Phonons. *Phys. Rev. B* 2002, 66, 195406.
89. Corio, P.; Santos, P. S.; Brar, V. W.; Samsonidze, G. G.; Chou, S. G.; Dresselhaus, M. S. Potential Dependent Surface Raman Spectroscopy of Single Wall Carbon Nanotube Films on Platinum Electrodes. *Chem. Phys. Lett.* 2003, 370, 675 – 682.
90. Ohana, I.; Dresselhaus, M. S.; Tanuma, S. Resonant Raman Effect and Fano Distortion in the Stage-2 Graphite Donor Intercalation Compound C/Rb. *Phys. Rev. B* 1991, 43, 1773–1776.
91. Galimberti, G.; Pagliara, S.; Ponzoni, S.; Conte, S. D.; Cilento, F.; Ferrini, G.; Hofmann, S.; Arshad, M.; Cepek, C.; Parmigiani, F. The Photoinduced Charge Transfer Mechanism in Aligned and Unaligned Carbon Nanotubes. *Carbon* 2011, 49, 5246 – 5252.
92. Chan, C. T.; Ho, K. M.; Kamitakahara, W. A. Zone-center Phonon Frequencies for Graphite and Graphite Intercalation Compounds: Charge-transfer and Intercalate-coupling Effects. *Phys. Rev. B* 1987, 36, 3499–3502.
93. Das, A.; Sood, A. K.; Govindaraj, A.; Saitta, A. M.; Lazzeri, M.; Mauri, F.; Rao, C. N. R.

Doping in Carbon Nanotubes Probed by Raman and Transport Measurements. *Phys. Rev. Lett.* 2007, 99, 136803.

94. Dragin, F.; Pénicaud, A.; Iurlo, M.; Marcaccio, M.; Paolucci, F.; Anglaret, E.; Martel, R. Raman Doping Profiles of Polyelectrolyte SWNTs in Solution. *ACS Nano* 2011, 5, 9892–9897.
95. Song, H.; Ishii, Y.; Al-zubaidi Ayar; Sakai, T.; Kawasaki, S. Temperature-dependent Water Solubility of Iodine-doped Single-walled Carbon Nanotubes Prepared Using an Electrochemical Method. *Phys. Chem. Chem. Phys.* 2013, 15, 5767–5770.
96. Azaïs, P.; Duclaux, L.; Florian, P.; Massiot, D.; Lillo-Rodenas, M.-A.; Linares-Solano, A.; Peres, J.-P.; Jehoulet, C.; Béguin, F. Causes of Supercapacitors Ageing in Organic Electrolyte. *J. Power Sources* 2007, 171, 1046 – 1053.
97. Grigorian, L.; Williams, K. A.; Fang, S.; Sumanasekera, G. U.; Loper, A. L.; Dickey, E. C.; Pennycook, S. J.; Eklund, P. C. Reversible Intercalation of Charged Iodine Chains into Carbon Nanotube Ropes. *Phys. Rev. Lett.* 1998, 80, 5560–5563.
98. Hornbaker, D. J.; Kahng, S.-J.; Misra, S.; Smith, B. W.; Johnson, A. T.; Mele, E. J.; Luzzi, D. E.; Yazdani, A. Mapping the One-Dimensional Electronic States of Nanotube Peapod Structures. *Science* 2002, 295, 828–831.
99. Matsushita, T.; Ishii, Y.; Kawasaki, S. Sodium Ion Battery Anode Properties of Empty and C60-inserted Single-walled Carbon Nanotubes. *Mater. Express* 2013, 3, 30–36.
100. Ayala, P.; Arenal, R.; Rümmeli, M.; Rubio, A.; Pichler, T. The Doping of Carbon Nanotubes with Nitrogen and Their Potential Applications. *Carbon* 2010, 48, 575–586.
101. Lota, G.; Lota, K.; Frackowiak, E. Nanotubes Based Composites Rich in Nitrogen for Supercapacitor Application. *Electrochem. Commun.* 2007, 9, 1828–1832.
102. Parvez, K.; Yang, S.; Hernandez, Y.; Winter, A.; Turchanin, A.; Feng, X.; Müllen, K.

Nitrogen-Doped Graphene and Its Iron-Based Composite As Efficient Electrocatalysts for Oxygen Reduction Reaction. *ACS Nano* 2012, 6, 9541–9550.

103. Wu, G.; Mack, N. H.; Gao, W.; Ma, S.; Zhong, R.; Han, J.; Baldwin, J. K.; Zelenay, P. Nitrogen-Doped Graphene-Rich Catalysts Derived from Heteroatom Polymers for Oxygen Reduction in Nonaqueous Lithium–O2 Battery Cathodes. *ACS Nano* 2012, 6, 9764–9776.

104. Mo, Z.; Zheng, R.; Peng, H.; Liang, H.; Liao, S. Nitrogen-doped Graphene Prepared by a Transfer Doping Approach for the Oxygen Reduction Reaction Application. *J. Power Sources* 2014, 245, 801–807.

105. Yan, J.; Meng, H.; Xie, F.; Yuan, X.; Yu, W.; Lin, W.; Ouyang, W.; Yuan, D. Metal Free Nitrogen Doped Hollow Mesoporous Graphene-analogous Spheres as Effective Electrocatalyst for Oxygen Reduction Reaction. *J. Power Sources* 2014, 245, 772–778.

106. Lu, Z.-J.; Xu, M.-W.; Bao, S.-J.; Tan, K.; Chai, H.; Cai, C.-J.; Ji, C.-C.; Zhang, Q. Facile Preparation of Nitrogen-doped Reduced Graphene Oxide as a Metal-free Catalyst for Oxygen Reduction Reaction. *J. Mater. Sci.* 2013, 48, 8101–8107.

107. Zheng, Y.; Jiao, Y.; Jaroniec, M.; Jin, Y.; Qiao, S. Z. Nanostructured Metal-Free Electrochemical Catalysts for Highly Efficient Oxygen Reduction. *Small* 2012, 8, 3550–3566.

108. Liu, D.; Zhang, X.; Sun, Z.; You, T. Free-standing Nitrogen-doped Carbon Nanofiber Films as Highly Efficient Electrocatalysts for Oxygen Reduction. *Nanoscale* 2013, 5, 9528–9531.

109. Huang, X.; Zhang, R.; Zhang, X.; Wen, G.; Yu, H.; Zhou, Y. Synthesis of Nitrogen-doped Carbon Microtubes for Application in Lithium Batteries. *Scr. Mater.* 2012, 67, 987–990.

110. Cho, Y. J.; Kim, H. S.; Im, H.; Myung, Y.; Jung, G. B.; Lee, C. W.; Park, J.; Park, M.-H.; Cho, J.; Kang, H. S. Nitrogen-Doped Graphitic Layers Deposited on Silicon Nanowires for Efficient Lithium-Ion Battery Anodes. *J. Phys. Chem. C* 2011, 115, 9451–9457.

111. Hassan, F. M.; Chabot, V.; Li, J.; Kim, B. K.; Ricardez-Sandoval, L.; Yu, A. Pyrrolic-structure

Enriched Nitrogen Doped Graphene for Highly Efficient Next Generation Supercapacitors. *J. Mater. Chem. A* 2013, 1, 2904–2912.

112. Rahman, M. A.; Wang, X.; Wen, C. High Energy Density Metal-Air Batteries: A Review. *J. Electrochem. Soc.* 2013, 160, A1759–A1771.

113. Lu, Y.-F.; Lo, S.-T.; Lin, J.-C.; Zhang, W.; Lu, J.-Y.; Liu, F.-H.; Tseng, C.-M.; Lee, Y.-H.; Liang, C.-T.; Li, L.-J. Nitrogen-Doped Graphene Sheets Grown by Chemical Vapor Deposition: Synthesis and Influence of Nitrogen Impurities on Carrier Transport. *ACS Nano* 2013, 7, 6522–6532.

114. Wang, C.; Zhou, Y.; He, L.; Ng, T.-W.; Hong, G.; Wu, Q.-H.; Gao, F.; Lee, C.-S.; Zhang, W. In Situ Nitrogen-doped Graphene Grown from Polydimethylsiloxane by Plasma Enhanced Chemical Vapor Deposition. *Nanoscale* 2012, 5, 600–605.

115. Sheng, Z.-H.; Shao, L.; Chen, J.-J.; Bao, W.-J.; Wang, F.-B.; Xia, X.-H. Catalyst-Free Synthesis of Nitrogen-Doped Graphene via Thermal Annealing Graphite Oxide with Melamine and Its Excellent Electrocatalysis. *ACS Nano* 2011, 5, 4350–4358.

116. Paek, E.; Pak, A. J.; Kweon, K. E.; Hwang, G. S. On the Origin of the Enhanced Supercapacitor Performance of Nitrogen-Doped Graphene. *J. Phys. Chem. C* 2013, 117, 5610–5616.

LIST OF PUBLICATIONS

1. Ayar Al-zubaidi, Tsuyoshi Inoue, Tomohiro Matsushita, Yosuke Ishii, Takeshi Hashimoto, and Shinji Kawasaki, "Cyclic Voltammogram Profile of Single-walled Carbon Nanotube Electric Double-Layer Capacitor Electrode Reveals Dumbbell Shape", **J. Phys. Chem. C**, Volume 116, Pages 7681−7686, **2012**.
2. Ayar Al-zubaidi, Tsuyoshi Inoue, Tomohiro Matsushita, Yosuke Ishii and Shinji Kawasaki, "Ion adsorption on the inner surface of single-walled carbon nanotubes used as electrodes for electric double-layer capacitors", **Phys. Chem. Chem. Phys.**, Volume 14, Pages 16055-16061, **2012**.
3. Ayar Al-zubaidi, Yosuke Ishii, Saki Yamada, Tomohiro Matsushita, Shinji Kawasaki, "Spectroscopic Evidence for the Origin of the Dumbbell Cyclic Voltammogram of Single-walled Carbon Nanotubes", **Phys. Chem. Chem. Phys**., Volume 15, Pages 20672-20678, **2013**.
4. Zinan Jiang, Ayar Al-zubaidi, and Shinji Kawasaki, "Unusual electric double-layer capacitance increase with charge-discharge cycles of nitrogen doped single-walled carbon nanotubes", **submitted to "Carbon".**
5. Ayar Al-zubaidi, Yosuke Ishii, Tomohiro Matsushita, and Shinji Kawasaki, "Diameter Dependent Doping of Single-Walled Carbon Nanotube Used as Electrical Double Layer Capacitor Electrode", **ECS Trans.**, Volume 50 , No., 43, Pages 13-18, **2013**.
6. Hayong Song, Yosuke Ishii, Ayar Al-zubaidi, Takenobu Sakai and Shinji Kawasaki, "Temperature dependent water solubility of iodine-doped

single-walled carbon nanotubes prepared by an electrochemical method", **Phys. Chem. Chem. Phys**., Volume 15, Pages 5767-5770, **2013**.

7. Yosuke Ishii, Yoshiki Nishiwaki, **Ayar Al-zubaidi**, and Shinji Kawasaki, "Pore Size Determination in Ordered Mesoporous Materials using Powder X-ray Diffraction", **J. Phys. Chem. C,** Volume 117, Number 35, Pages 18120–18130, **2013**.
8. Yosuke Ishii, Saki Yamada, Tomohiro Matsushita, **Ayar Al-Zubaidi**, Shinji Kawasaki, "Halogen Ion Adsorption Properties of Carbon Nanotube Electrodes", **TANSO**, No. 250, Pages 248–52, **2011**.

LIST OF PRESENTATIONS

1. Ayar Al-zubaidi, Tsuyoshi Inoue, Tomohiro Matsushita, Shinji Kawasaki, (Ion Storage Properties of Inner, Outer, Unwrapped, and Chemically Modified Surface of Single Walled Carbon Nanotubes), 3rd International Symposium on Advanced Plasma Science and its Applications for Nitrides and Nanomaterials (ISPlasma2011), Nagoya Institute of Technology, Nagoya City, Aichi, Japan, March 6 – 9, **2011**.
2. Ayar Al-zubaidi, Tomohiro Matsushita, Shinji Kawasaki, (Relation Between the CV Shape and the Tube Structure of Single-walled Carbon Nanotube EDLC Electrode), 62nd Annual Meeting of the International Society of Electrochemistry, Niigata City, Niigata, Japan, September 11 – 15, **2011**.
3. Ayar Al-Zubaidi, Yosuke Ishii, Tomohiro Matsushita, Saki Yamada, Shinji Kawasaki, (Ion Accessibility and the Resulting Electrical Double Layer Capacitance of Different Electrolytes Inside Open-end SWCNT), 4th

International Symposium on Advanced Plasma Science and its Applications for Nitrides and Nanomaterials (ISPlasma2012), Chubu University, Kasugai City, Aichi, Japan March 4 – 8, **2012**.

4. Ayar Al-zubaidi, Yosuke Ishii, Tomohiro Matsushita, Shinji Kawasaki, (Influence of Surface Structure and Ion Type on the Capacitance of Doped SWCNTs Electrode of Electrochemical Capacitors), Pacific Rim Meeting on Electrochemical and Solid State Science (PRIME 2012), Honolulu, Hawaii, USA, October 7-12, **2012**.
5. Ayar Al-zubaidi, Yosuke Ishii, Tomohiro Matsushita, Shinji Kawasaki, (Diameter Dependent Doping of Single-Walled Carbon Nanotube Used as Electrical Double Layer Capacitor Electrode), Pacific Rim Meeting on Electrochemical and Solid State Science (PRIME 2012), Honolulu, Hawaii, USA, October7-12, **2012** .
6. Ayar Al-zubaidi・石井陽祐・松下知弘・川崎晋司[チューブ径に依存した単層カーボンナノチューブ電極の特異なイオン吸着特性] 43rd Annual Meeting of Union of Chemistry-Related Societies in Chubu Area, Japan. Nagoya Institute of Technology, Nagoya, Aichi, Japan, November 10-11, **2012**.
7. Ayar Al-zubaidi, Yosuke Ishii, Tomohiro Matsushita, Saki Yamada (Electric Double Layer Capacitor Properties of Doped Single-walled Carbon Nanotubes) 5th International Symposium on Advanced Plasma Science and its Applications for Nitrides and Nanomaterials (ISPlasma2013), Nagoya University, Japan, January 28-February 1st **2013**.
8. Ayar Al-zubaidi, Masato Tsutsui, Yosuke Ishii, and Shinji Kawasaki (Spectroscopic Changes associated with the Dumbbell Cyclic Voltammogram of

Single-walled Carbon Nanotubes used as Electric Double Layer Capacitor Electrodes), The 2013 International Conference on Advanced Capacitors (ICAC 2013), organized by The Electrochemical Society of Japan, Osaka, Japan, May 27 - 30, **2013**.

AWARDS AND RECOGNITIONS

1. (Best Presentation Award), from 4th International Symposium on Advanced Plasma Science and its Applications for Nitrides and Nanomaterials (ISPlasma2012), **2012**.
2. (President of Nagoya Institute of Technology) Award, for student outstanding academic achievement, **2013**.
3. (Student Grant Award), from the 2013 International Conference on Advanced Capacitors (ICAC 2013), **2013**.

APPENDIX

APPENDIX

Additional results of *in situ* Raman measurement

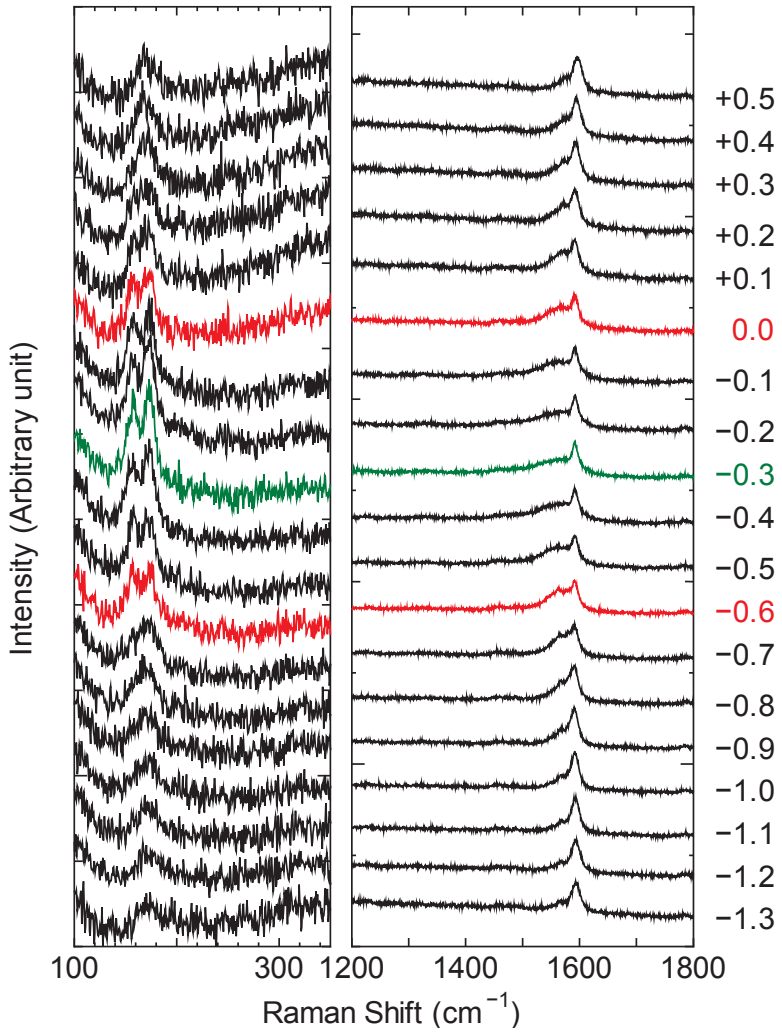

Figure A1: Raman spectra for open-end SWCNTs in $TEMABF_4$ using red laser (λ=632.8 nm). Values of applied potential in (V) are indicated on the right.

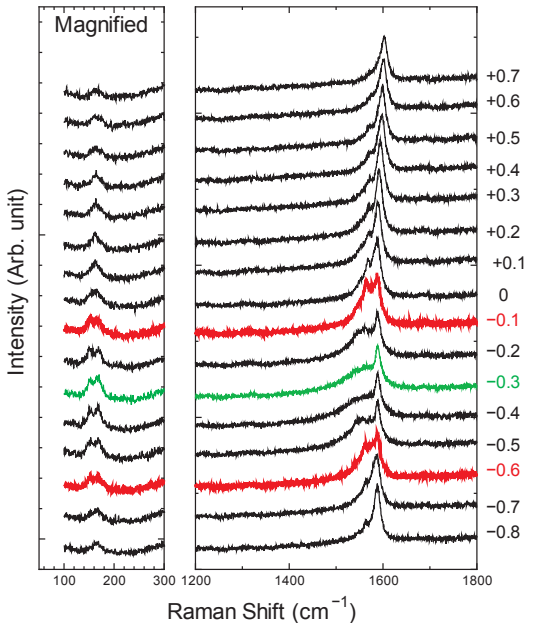

Figure A2: Raman spectra for open-end SWCNTs in NaBr using red laser (λ=632.8 nm). Values of applied potential in (V) are indicated on the right.

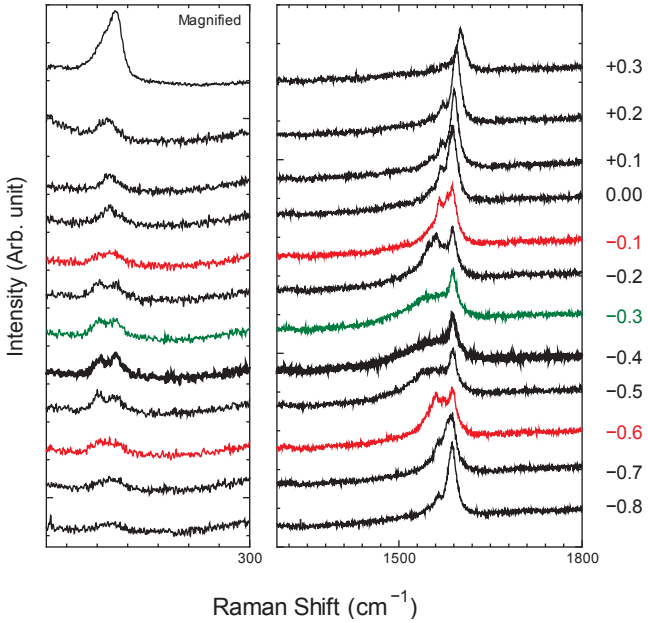

Figure A3: Raman spectra for open-end SWCNTs in NaI using red laser (λ=632.8 nm). Values of applied potential in (V) are indicated on the right.

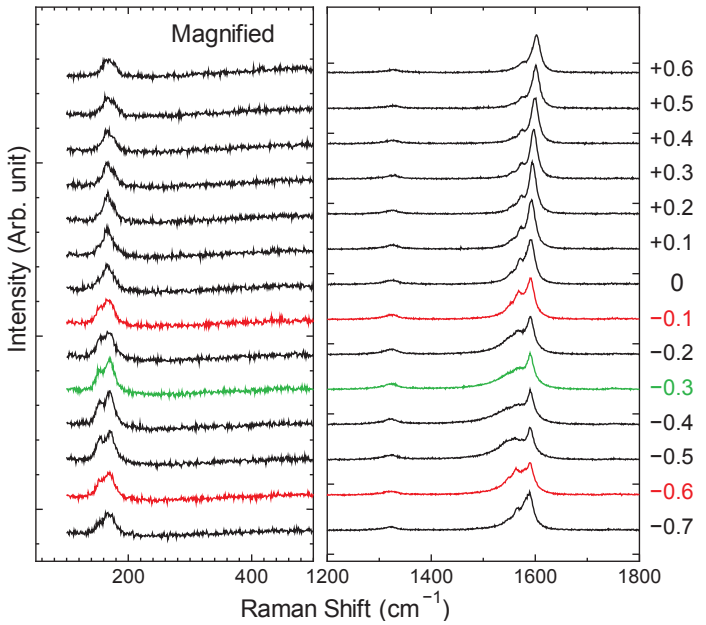

Figure A4: Raman spectra for open-end SWCNTs in KCl using red laser (λ=632.8 nm). Values of applied potential in (V) are indicated on the right.

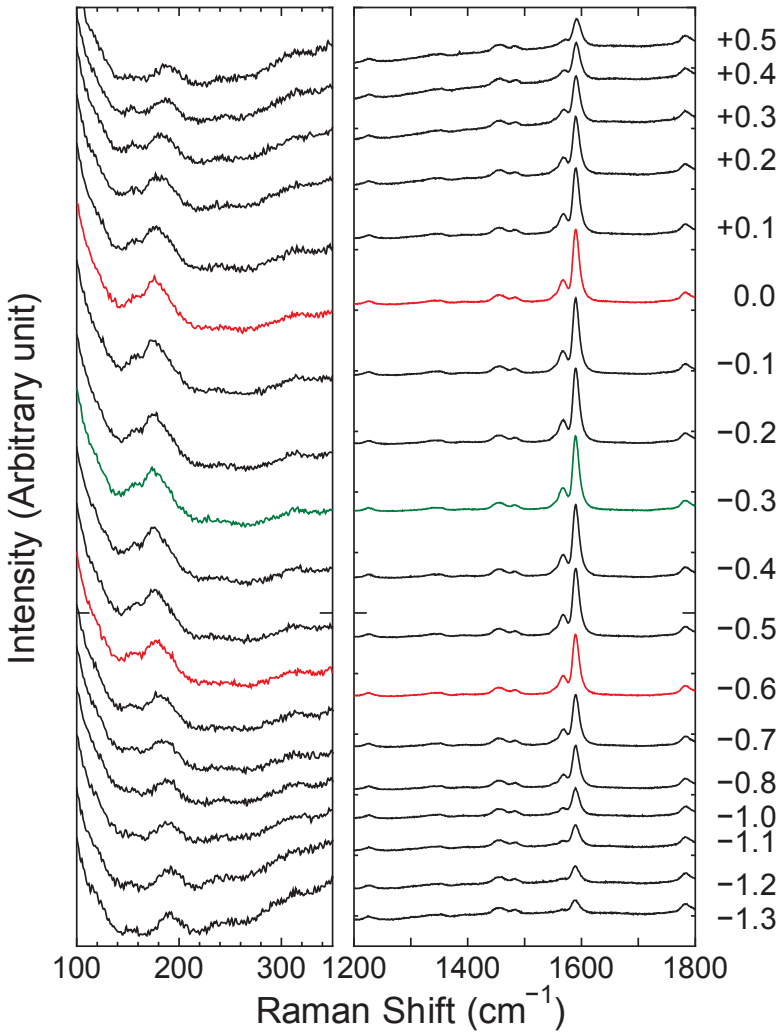

Figure A5: Raman spectra for open-end SWCNTs in $TEMABF_4$ using green laser (λ=532 nm). Values of applied potential in (V) are indicated on the right.

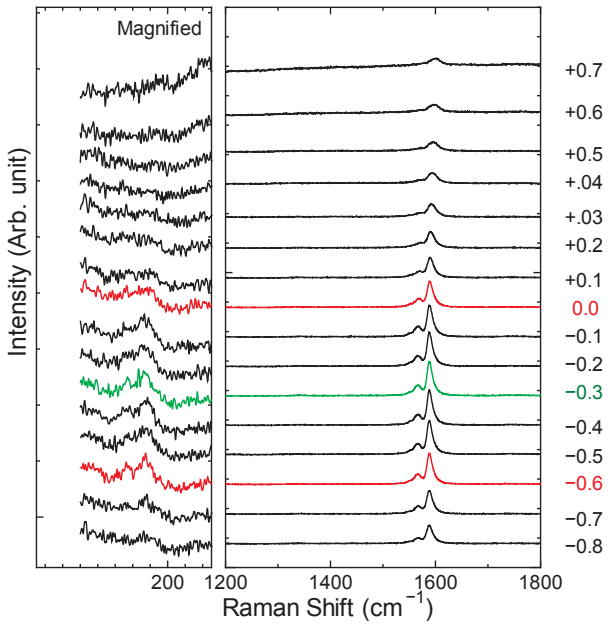

Figure A6: Raman spectra for open-end SWCNTs in NaBr using green laser (λ=532 nm). Values of applied potential in (V) are indicated on the right.

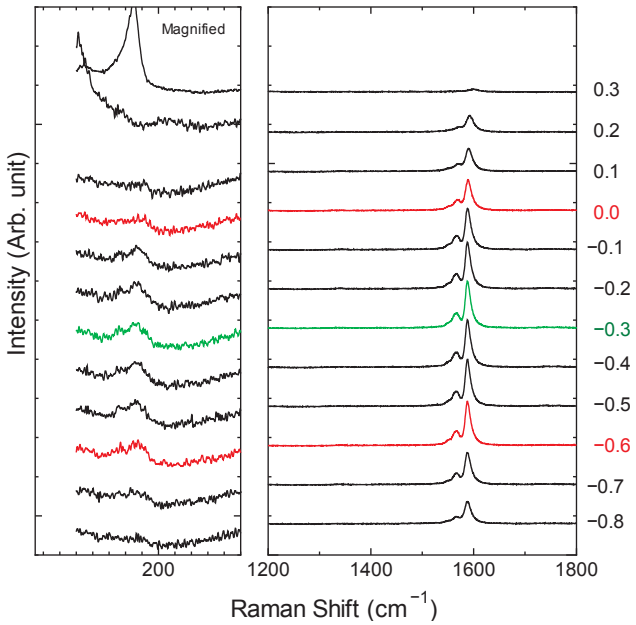

Figure A7: Raman spectra for open-end SWCNTs in NaI using green laser (λ=532 nm). Values of applied potential in (V) are indicated on the right.

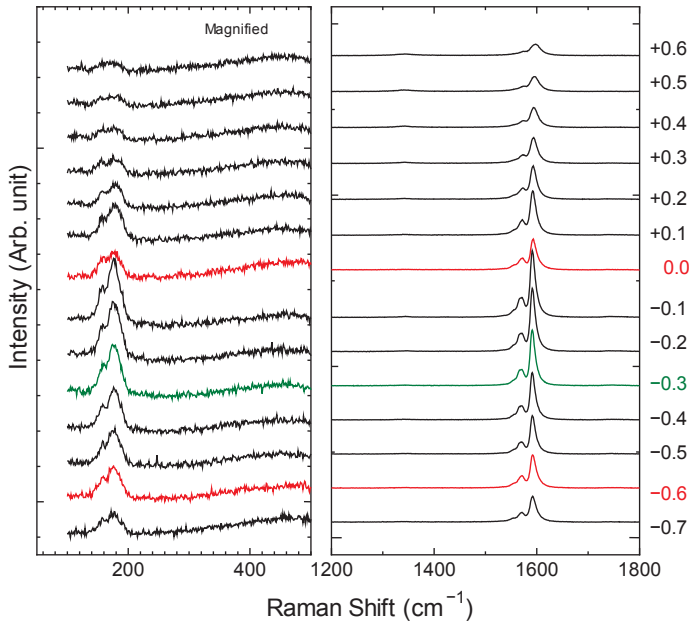

Figure A8: Raman spectra for open-end SWCNTs in KCl using green laser (λ=532 nm). Values of applied potential in (V) are indicated on the right.

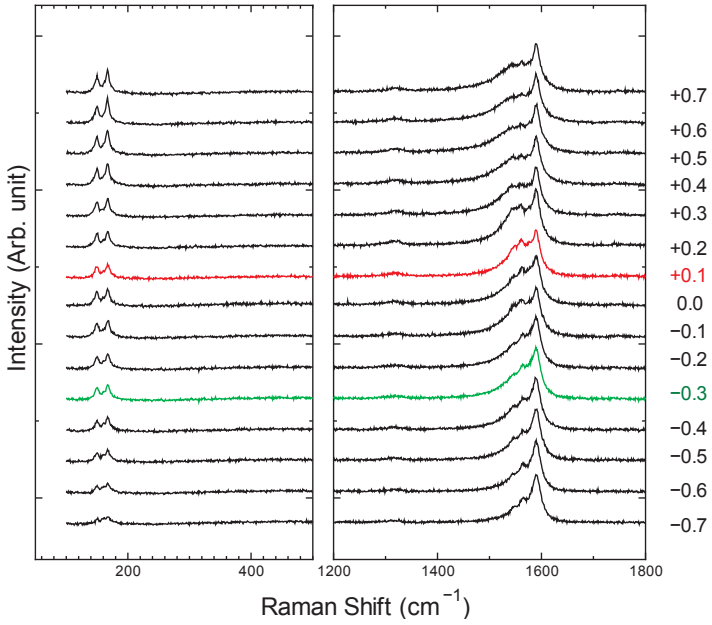

Figure A9: Raman spectra for closed-end SWCNTs in NaCl using red laser (λ=632.8 nm). Values of applied potential in (V) are indicated on the right.

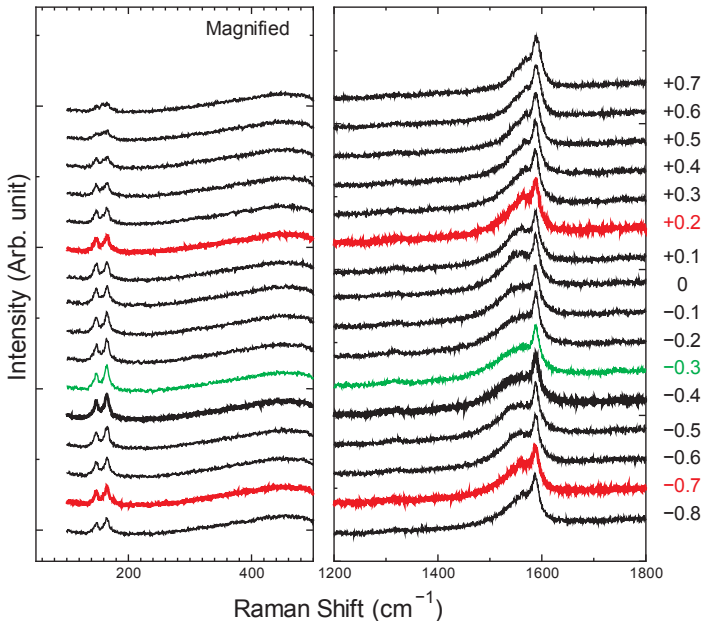

Figure A10: Raman spectra for closed-end SWCNTs in NaBr using red laser (λ=632.8 nm). Values of applied potential in (V) are indicated on the right.

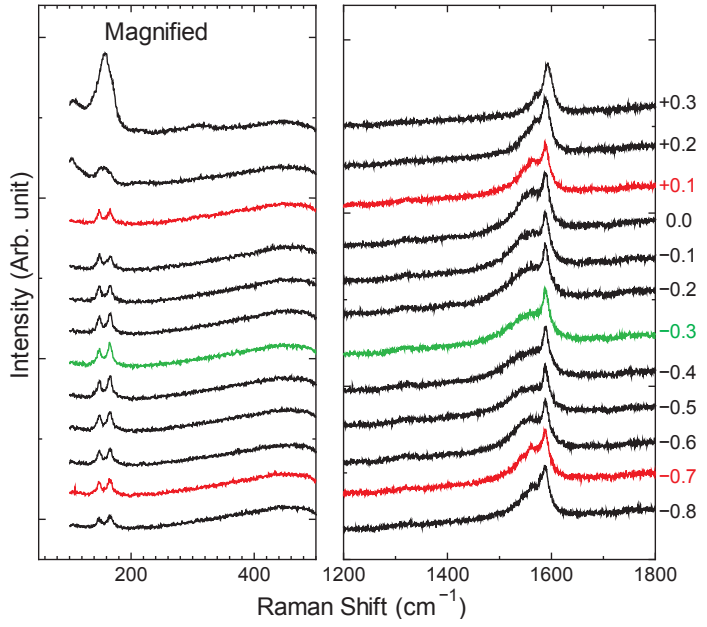

Figure A11: Raman spectra for closed-end SWCNTs in NaI using red laser (λ=632.8 nm). Values of applied potential in (V) are indicated on the right.

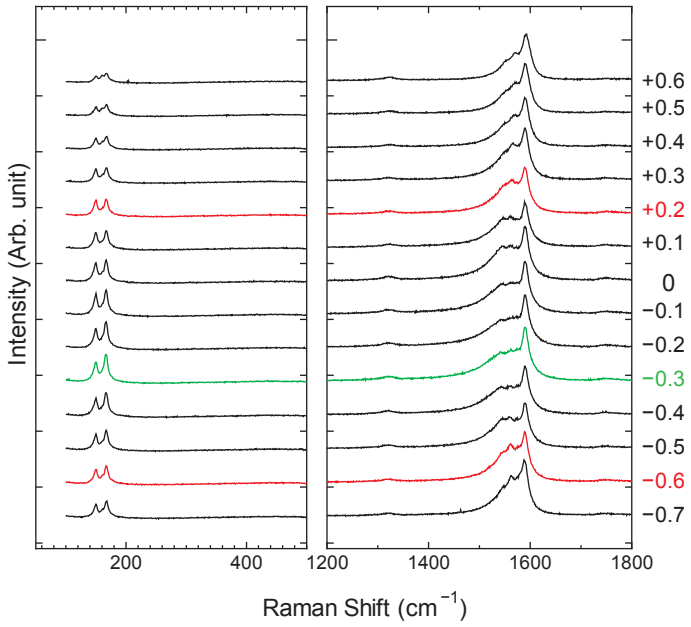

Figure A12: Raman spectra for closed-end SWCNTs in KCl using red laser (λ=632.8 nm). Values of applied potential in (V) are indicated on the right.

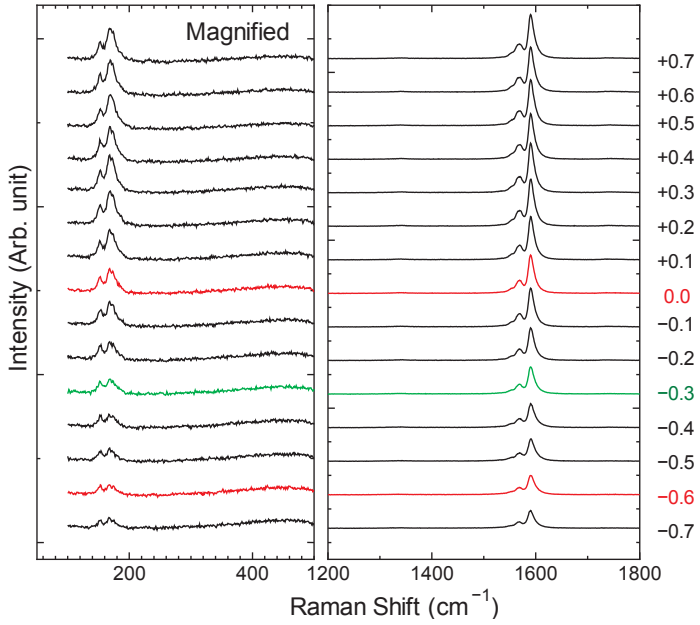

Figure A13: Raman spectra for closed-end SWCNTs in NaCl using green laser (λ=532 nm). Values of applied potential in (V) are indicated on the right.

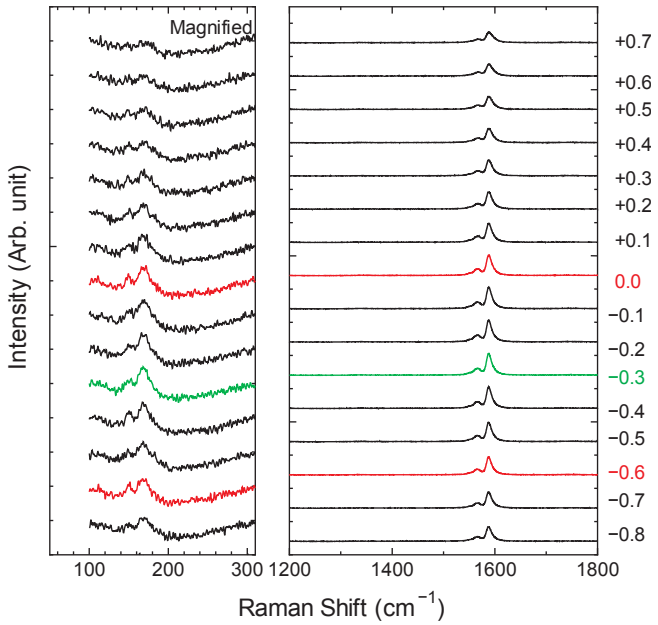

Figure A14: Raman spectra for closed-end SWCNTs in NaBr using green laser (λ=532 nm). Values of applied potential in (V) are indicated on the right.

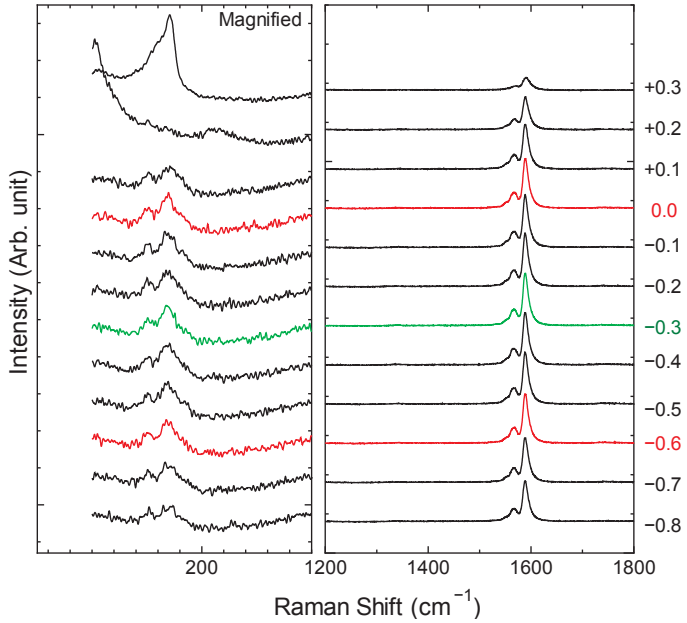

Figure A15: Raman spectra for closed-end SWCNTs in NaI using green laser (λ=532 nm). Values of applied potential in (V) are indicated on the right.

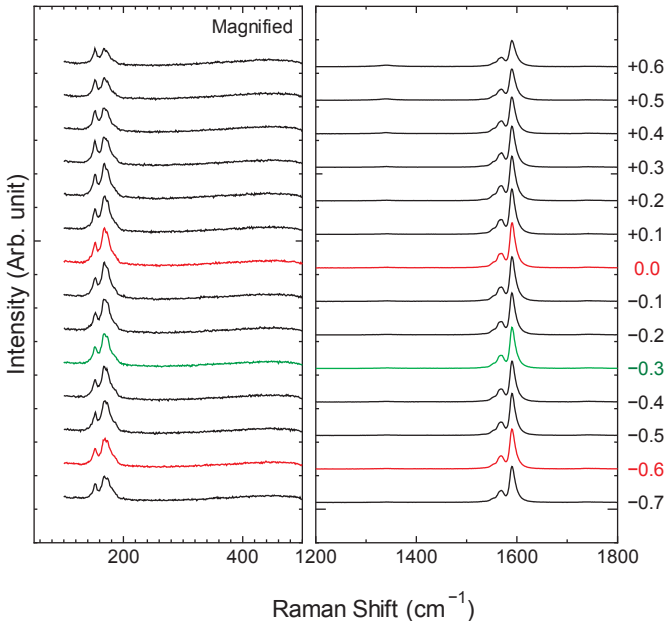

Figure A16: Raman spectra for closed-end SWCNTs in KCl using green laser (λ=532 nm). Values of applied potential in (V) are indicated on the right.